# A Methodology for Centrifugal Compressor Stability Prediction



by

Björn Benneke

Submitted to the Department of Aeronautics and Astronautics
in partial fulfillment of the requirements for the degree of

Master of Science in Aerospace Engineering



at the

MASSACHUSETTS INSTITUTE OF TECHNOLOGY

September 2009



Author .....
Department of Aeronautics and Astronautics
August 15th, 2009

Certified by .....
Zoltán S. Spakovszky
H. N. Slater Associate Professor
Thesis Supervisor

Accepted by .....
David L. Darmofal
Associate Department Head
Chair, Committee on Graduate Students

# A Methodology for Centrifugal Compressor Stability Prediction

by

Björn Benneke

Submitted to the Department of Aeronautics and Astronautics
on August 15th, 2009, in partial fulfillment of the
requirements for the degree of
Master of Science in Aerospace Engineering

## Abstract

The stable operation of centrifugal compressors is limited by well-known phenomena, rotating stall and surge. Although the manifestation of the full scale instabilities is similar to the ones observed in axial machines, the stall inception in centrifugal compressors is less well understood. This thesis focuses on developing an integrated methodology to predict the stability limit and the stall inception pattern in highly-loaded centrifugal compressors with vaned diffusers. The approach, based on a body force representation of the blade rows, is different from previous research in that the prediction is independent of compressor stability correlations and a-priori knowledge of the compressor characteristics.

The methodology consists of a control volume analysis to define the body force fields based on steady, single-passage 3-D RANS simulations and a look-up table approach to capture the dependence of the body forces on the local flow parameters. The body force model was implemented in a finite volume scheme of an existing unsteady Euler solver for a full-wheel domain consisting of only 68,000 cells. The body force based compressor model was validated against high-fidelity 3-D RANS calculations and was applied to investigate the stall inception in a pre-production, 5.0 pressure ratio, high-speed centrifugal compressor stage of advanced design.

The body force based simulation at 75% corrected design speed agreed with experimental measurements available at design speed in that the diffuser becomes unstable at operating points with a positively sloped diffuser static pressure rise characteristic. Modal stall precursors were observed and the backward-traveling character of the long-wavelength disturbance was found to be in agreement with predictions by a previously developed analytical centrifugal compressor stability model and experimental measurements in the same compressor. Additional investigations in a compressor with altered dynamic behavior demonstrated the capability of the body force-based compressor model to capture the formation of short-wavelength spike-like stall precursors. It is the first time that both backward-traveling modal waves and short-wavelength spike-like stall precursors are simulated in a centrifugal compressor with vaned diffuser, in agreement with experimental measurements. Further work is required to investigate the flow mechanisms responsible for the formation of the short-wavelength disturbances and to establish a criterion for their occurrence.

Thesis Supervisor: Zoltán S. Spakovszky
Title: H. N. Slater Associate Professor

# Acknowledgments

This project was enabled and supported by ABB Turbo System Ltd. under supervision of Dr. Christian H. Roduner. At ABB, I would like to thank Dr. Roduner, Dr. Daniel Rusch, Dr. Janpeter Kühnel, Dr. Hans-Peter Dickmann, and Dr. Niklas Sievers for their support and advice.

Particularly, I would like to thank Prof. Zoltán S. Spakovszky for his guidance, insight, and support throughout my graduate studies at MIT. His passion and advice have helped me to become a better researcher. He is always available for his students and keeps the spirit of the MIT Gas Turbine Laboratory alive. I am very grateful that I had the chance to become part of this laboratory.

I also would like to thank Jon Everitt, Andrew Hill, and Isabelle Delefortrie for their camaraderie and the cooperative work on the ABB project. I am grateful to Dr. Ottmar Schäfer for providing technical support and advice for the Euler solver.

At the GTL, I have very much enjoyed the productive atmosphere and the company of my lab-mates. Special thanks go to my office-mates Andreas, Francois, David, and Ryan, who accompanied me in happy times as well as in stressful times. They have supported me with technical advice, humor, and friendship during long hours in 31-259. I also would like to thank Georg, George, Jeff, Jon, Leo, Sho, and Shinji for their friendship and making the GTL a great place to work.

I am very grateful to my parents and my brother for their unyielding love and their support. Throughout my life and education, I could always rely on them if I needed support or help. Lastly, but most importantly, I would like to thank Blair who has my gratitude and love for her encouragement, support, and understanding over the last two years.

# Contents

# List of Figures

# Nomenclature

## Abbreviations

| | |
|---|---|
| CFD | Computational Fluid Dynamics |
| RANS | Reynold-Averaged Navier Stokes |

## Roman Symbols

| | |
|---|---|
| $A$ | Flow area |
| $A^*$ | Flow area at sonic conditions |
| $D$ | Corrected flow per unit area |
| $e$ | Internal energy |
| $e_t$ | Total energy |
| $\vec{f}$ | Body force vector |
| $H$ | Flux quantity |
| $j$ | Circumferential cell index |
| $l_{ref}$ | reference length |
| $p$ | Static pressure |
| $p_t$ | Stagnation pressure |
| $M$ | Mach number in absolute frame |
| $M_m$ | Mach number in meridional plane |
| $M_{rel}$ | Mach number in relative frame |
| $r$ | Radial Coordinate |
| $r_2$ | Impeller tip radius |

| | |
|---|---|
| $R$ | Specific gas constant |
| $s$ | Blade pitch |
| $S$ | Surface area of control volume |
| $T$ | Static temperature |
| $T_t$ | Stagnation temperature |
| $\vec{V}$ | Velocity vector in absolute frame |
| $v_\perp$ | Velocity perpendicular to control surface |
| $x$ | Axial Coordinate |

## Greek Symbols

| | |
|---|---|
| $\alpha$ | Swirl angle |
| $\beta$ | Pitch angle in meridional plane |
| $\Delta$ | Change in quantity |
| $\gamma$ | Specific heat ratio |
| $\phi$ | Flow coefficient |
| $\lambda$ | Blade metal blockage |
| $\omega$ | Impeller rotor frequency |
| $\theta$ | Circumferential coordinate |
| $\rho$ | Density |

## Subscripts

| | |
|---|---|
| $_{PS}$ | Pressure side |
| $_{r,\theta,x}$ | radial, circumferential, and axial coordinates |
| $_{SS}$ | Suction side |
| $_{t}$ | Stagnation quantity |
| $_{VLS}$ | Conditions at inlet of vaneless space |

## Superscripts

| | |
|---|---|
| $()^*$ | Sonic condition |

# Chapter 1

# Introduction

## 1.1 Background

Recent trends in emission reduction of internal combustion engines have led to a demand for turbocharger compressors with increased pressure ratios of up 5.5-6.0. Over the last few decades, highly-loaded centrifugal compressors in turboshaft engines for helicopters and turboprops have demonstrated that design pressure ratios of 6 or higher can be obtained in a single-stage centrifugal compressor. However, the high pressure rise capability is usually accompanied by narrower compressor maps due to compressibility effects and the challenging diffusion of the high Mach number flow from high-speed impellers.

Figure 1-1 illustrates the compressor maps for a turbocharger and a typical helicopter engine compressor. The differences in design philosophy and the resulting performance are strongly governed by the application. The turbocharger compressor map (left) is characterized by a wide, stable operating range for a given speed, while the compressor map of the helicopter engine shows narrow characteristics but much higher pressure ratios.

The key design challenge for turbocharger centrifugal compressors is the demand for high-pressure ratio, high efficiency, and sufficient surge margin throughout the operating envelope.

One way to improve stability is to introduce impeller designs with increased back-

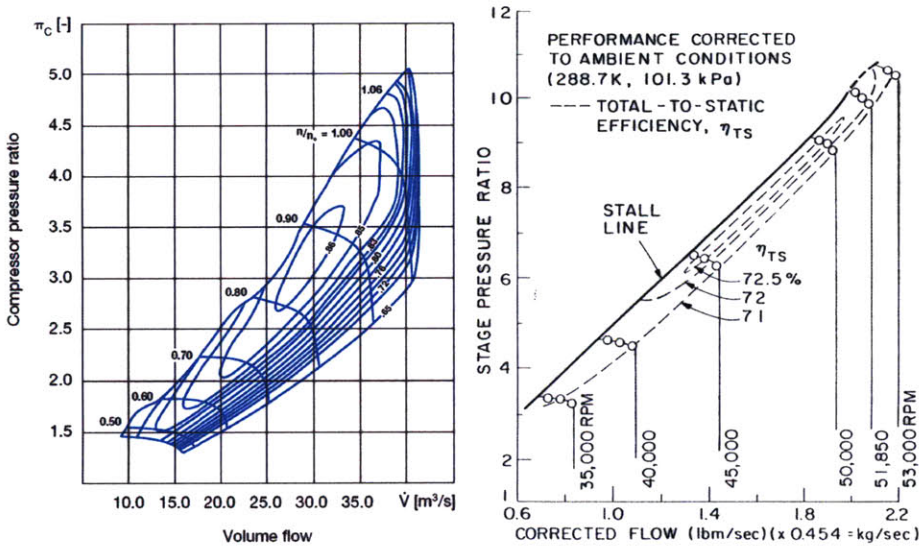


Figure 1-1: Compressor maps of centrifugal compressors. Left: turbocharger compressor [30]. Right: helicopter engine compressor [31]. Note the difference in the operating range for a given speed.

sweep. Due to the increased backsweep, the slope of the ideal compressor characteristic becomes more negative improving stability [13]. However, to maintain the same pressure ratio requires higher rotor speeds and, therefore improved materials. As described by Spakovszky and Roduner [29], the desire is to replace the high-strength titanium alloys by aluminum alloys which may be machined at a much lower cost.

This thesis is focused on establishing a methodology to predict the stability of highly-loaded centrifugal compressors. If successful, the method has the potential to enable the stability assessment in the early development phase of advanced compressor configurations.

### 1.1.1 Compressor Instability

The phenomena limiting the stable operating range of centrifugal compressors are rotating stall and surge. The manifestation of these full-scale instabilities in centrifugal compressors is similar to that in axial machines and was first described by Emmons [8].

During rotating stall, one or more stall cells propagate around the circumference of

the compressor typically at a rotational speed of 20-70% of the rotor speed [13]. As the passage flow in the cells is severely stalled, the net mass flow in the cells is negligible compared to the flow though unstalled passages. In fully-developed rotating stall, the local flow in the passages is highly unsteady, while the annulus-averaged mass flow and the pressure rise are quasi-steady. The rotating stall cells lead to a continuous redistribution of flow between the blade passages. The inherently unsteady nature of the flow field poses major challenges in the modeling of rotating stall inception.

The second type of instability, surge, is a global compression system instability. During surge, the global mass flow and pressure rise exhibit large-amplitude oscillations which lead to fully-reversed flow. The frequency of the oscillation depends on the entire compression system and is usually between 3-10Hz, at least an order of magnitude lower than for rotating stall.

### 1.1.2 Stall Inception

The key step in predicting the stability limit is describing the inception of rotating stall and surge. Extensive research has been conducted to investigate the path into full-scale instability, often referred to as the pre-stall behavior.

#### Axial Compressors

The stall inception in axial compressors has received much more attention than the one in centrifugal machines. Based on extensive research, it is recognized that there are two main routes to full-scale instability: modal oscillations and spike-like disturbances. Depending on the stage matching, both phenomena can occur in the same compressor.

Modal oscillations are long length-scale circumferential perturbations that are natural resonances of oscillation in the compression system. These small-amplitude disturbances usually extend over a wide sector of the annulus, and the full length of the compressor. The occurrence of modal waves was theoretically predicted by a low-order, analytical model developed by Moore and Greitzer [25] and then observed

experimentally by McDougall et al [24]. The model by Moore and Greitzer showed that the time-evolution of modal oscillations is linked to the mean background flow field governing the the damping of the oscillations. If the background flow conditions are such that their damping becomes negative, the oscillations grow in amplitude and the compression system becomes unstable.

Based on the framework by Moore and Greitzer, many formulations were developed. A summary is given in a review paper by Longley [22]. Spakovszky extended the model by Moore and Greitzer with the capability to resolve the dynamics of individual blade-rows, inter-blade-row gaps and intermediate ducts [28]. This model can thus capture overall dynamic system effects and the coupling between the components. Besides the detailed studies of the stall inception, research was performed to investigate the use of active control schemes to extend the operating range of axial compressors. The idea was first introduced by Epstein et al [9] and, since then, successful experiments were carried out by Paduano et al. [27], Day [4], and Haynes et al. [15].

As opposed to modal oscillations, spike-like disturbances are short-wavelength and local phenomena that emerge from a few blades only [4]. The spike stall inception is characterized by the localized stalling of one blade-row which evolves into a two-dimensional stall cell and triggers full-scale instability within a few rotor revolutions. Due to their non-linear nature, spike-like disturbances cannot be described by the low-order, analytical models.

Camp and Day [2] established a criterion, based on the stage matching, that determined which of the stall inception patterns is going to arise. A spike-like disturbance is likely to trigger compressor stall if the critical rotor incidence is reached before the peak of the total-to-static pressure rise characteristic. However, if the stage matching is such that the peak of the pressure rise is reached before the rotor incidence exceeds its critical value, the compressor is likely to form modal waves.

### Centrifugal Compressors

To date, a generalized theory or criterion for the stall inception in centrifugal compressor does not exist. The inherently more complicated flow and the wide range of system characteristics present a major challenge in the development of a generalized description.

For vaned diffusers, Lawless and Fleeter [21] investigated the rotating stall acoustic signature in a low speed centrifugal compressor. Starting from the assumption introduced by Moore and Greitzer [25] that rotating stall cells are the mature, fully-developed form of weak linear disturbances, they found a wide repertoire of excited spatial modes. The analysis of high-speed compressors by Oakes et. al [26] showed experimentally the existence of rotating stall pattern prior and during surge. The same work revealed the presence of a mode several hundred rotor revolution prior the occurrence of surge.

Research efforts by Dean [5] and later by Hunzinker and Gyarmathy [17] investigated the effects of the subcomponent performance in vaned diffusers on the stability of a centrifugal compressor. They identified the semi-vaneless space as the most critical element in the compressor stage.

A compression system stability model was developed by Spakovszky [28] that is capable of dealing with unsteady, radially swirling flows and of dissecting the dynamic behavior of the impeller and diffuser subcomponents. It was the first model that captured both the effects of the overall dynamic system and the coupling between the components in the system. This low-order, analytical model first predicted the existence of backward-traveling modal pre-stall waves prior to rotating stall. It was found that the backward-rotating rotating stall wave is caused by the interaction between pressure waves and unsteady vortex shedding driven by a resonance of the impeller and diffuser wave systems. The strongest activity was shown to be in the vaneless space.

A research project on a pre-production highly-loaded centrifugal compressor carried out by Spakovszky and Roduner [29] confirmed the existence of backward-

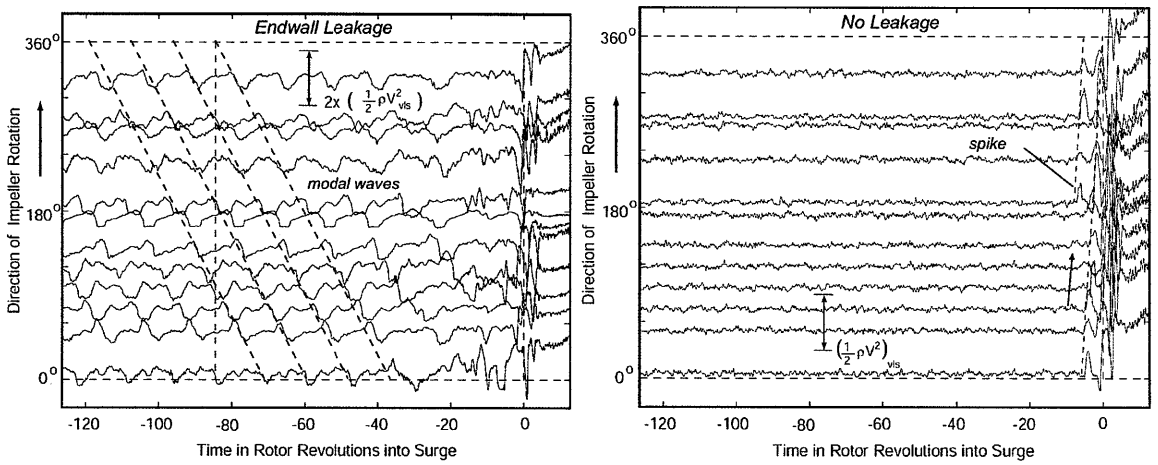


Figure 1-2: Static pressure traces measured at circumferentially distributed locations in the vaneless space. Modal stall inception (left). Spike stall inception (right). Figure adopted from [29]

rotating perturbations prior to the full-scale instability. They showed that the stable operating range and stall inception pattern are highly sensitive to the amount of bleed air extracted at the impeller exit. The bleed flow, used for secondary flow systems, reduces the endwall blockage in the vaneless space, thus altering the characteristics of vaneless space and semi-vaneless space. In agreement with the analytical model, the damping of the compression system for long-wavelength modal waves was reduced and a four-lobed backward rotating stall wave was formed (see Figure 1-2). This destabilization of the highly-loaded diffuser was accompanied by a 50% loss in the stable operating range.

Without the presence of bleed air, the centrifugal compressor was found to exhibit short-wavelength unsteady flow patterns ("spikes") in the vaneless space (see Figure 1-2). Although the short-wavelength disturbances are different than those in axial machines, the work revealed that they can also exist in centrifugal compressors. A general criterion for their occurrence is yet to be established. This work attempts to simulate this behavior with the goal to describe the necessary flow conditions leading to the formation of spikes.

## 1.2 Motivation

As stated previously, the major design challenge for highly-loaded centrifugal compressors is to achieve both a broad operating range and high efficiencies throughout the envelope. Due to compressibility effects, it becomes more and more difficult to obtain the desired surge margin at high pressure ratios. Novel designs are needed with extended surge margins and delayed onset of instability. Their development requires an improved understanding of the key mechanisms responsible for the formation of the stall precursors.

As mentioned earlier, the work by Spakovszky and Roduner [29] on a pre-production, highly-loaded centrifugal compressor of advanced design demonstrated that there can be two paths leading to full-scale instability. They showed that, depending on the amount of leakage flow, either modal waves or short-wavelength disturbances "spikes" can occur prior to the onset of instability. A four-lobed backward traveling rotating stall wave was measured with flow leakage present, in agreement with results from a previously developed low-order, dynamic stability model [28]. Based on this work, the hypothesis is that the spanwise flow non-uniformity at the impeller exit plays a key role in the stall inception process. However, to date there is no generalized theory or criterion for the formation of short-wavelength disturbances in centrifugal compressors.

## 1.3 Research Objectives and Questions

The research described in this thesis is devoted to establishing a novel and integrated method for predicting the stability for centrifugal compressors with vaned diffusers. The approach is different from previous research in that the prediction is independent of compressor stability correlations and a priori knowledge of the compressor characteristics. The goal is to determine the stability limit directly from the 3-D compressor geometry. The key research questions are:

1. What are the relevant flow features that need to be captured in the body force

representation in order to reproduce the flow field of a highly-loaded centrifugal compressor with vaned diffuser as observed in experiments and high-fidelity RANS simulations?

2. Based on this body force formulation, is the unsteady compressor model capable of simulating the formation of long-wavelength modal stall precursors in agreement with experimental measurements?

3. For an altered compressor dynamic behavior, can a short-wavelength spike-like disturbance be captured?

4. Is the presence of tip-leakage flow, as it exists in axial machines, necessary in the formation of spikes?

5. Based on the outcomes of this methodology, can a more generalized criterion for stall inception in centrifugal compressors with vaned diffuser be established?

## 1.4 Summary and Contributions

An integrated, body force-based methodology for the investigation of the stall inception point and the stall inception pattern in highly-loaded centrifugal compressors was established. The methodology is based on first principles and is independent of compressor stability correlations and a-priori knowledge of the compressor characteristics. The body force based compressor model was validated against high-fidelity RANS calculations.

Unsteady stall inception simulations in a highly-loaded centrifugal compressor with vaned diffuser were conducted at 75% corrected design speed. The diffuser is the least stable component and the formation of modal stall precursors was observed for operating points with a positively sloped diffuser static pressure rise characteristic. As measurements at 75% speed were not available, a comparison of trends was made with data at 100% corrected design speed. The results are in good agreement with the experimental measurements. In addition, unsteady simulations of an altered

compressor model demonstrated the capability of the methodology to capture the formation of short-wavelength spike-like stall precursor in the vaned diffuser

The established methodology is the first to capture the formation of both backward-traveling rotating stall precursors and short-wavelength spike-like stall precursors in centrifugal compressors with vaned diffusers.

# Chapter 2

# Overview of Stability Prediction

To investigate the stability of centrifugal compressors with vaned diffusers, a novel and integrated methodology was established. The method does not rely on compressor stability correlations or a-priori knowledge of the compressor characteristics. This chapter gives an overview of the methodology and describes the structure of this thesis and the context for each of the following chapters.

First, previous approaches for the investigation of centrifugal compressor instability are discussed. This discussion motivates the development of the body force based prediction methodology. Next, the fundamental ideas behind the body force model and the key pieces of the methodology are explained. The final section describes the technical roadmap. Starting from only the 3-D geometry, a route towards the investigation of compressor instability with the final goal of establishing a stall criterion for centrifugal compressors is outlined.

## 2.1 Motivation for a Body Forced Based Approach

Low-order, linear analytical models were developed to investigate the stability of the compression system towards long-wavelength modal stall precursors. The basic idea behind the models, first introduced by Moore and Greitzer [25], is that rotating stall and surge are the mature forms of small amplitude flow perturbations that are the natural resonances of oscillation in the compression system.

In contrast to modal wave stall precursors, short-wavelength "spike" stall inception is characterized by three-dimensional fluid phenomena that are inherently non-linear. Capturing the effects of spike formation requires one to describe flow length-scales of order blade scale. The complex, non-linear nature of the problems eludes a low-order, analytical description and requires a flow simulation that is capable of describing the three-dimensional features and non-linear aspects of the flow.

A way to account for the three-dimensional features and the non-linear aspects is to make use of computational fluid dynamics (CFD). However, the wide range of length-scales and time-scales of the fluid dynamics involved in the stall inception presents a challenge for the RANS simulations. To simulate the inherently unsteady and non-axisymmetric flow features at stall inception, time-accurate simulations of the full compressor annulus are required. However, in this large flow domain, the challenge in RANS simulations is to capture flow separation and regions of reversed flow.

This poses the question what relevant flow features need to be retained in a simplified approach. One way to deal with the challenge is a body force based approach. For a low-speed axial compressor, Gong [12] demonstrated that the path into instability can be simulated with an unsteady compressor flow model that represents the pressure and viscous effects of the blades on the flow by a body force distribution.

The methodology presented in this thesis builds on ideas from Gong's approach. Essential differences are that the empiricism in the body force correlations is removed by defining the body forces based on 3-D flow fields obtained from steady, single-passage RANS simulations. Additionally, the new methodology is applicable to highly-loaded centrifugal compressors with vaned diffusers, which have previously received much less attention than axial machines.

## 2.2 Body Force Based Compressor Model

The physical effects of the compressor blades on the flow field are due to the pressure and viscous forces at the solid surfaces. The fundamental idea behind the modeling

procedure is to redistribute these blade forces so that they act uniformly on the fluid mass. Instead of capturing individual blades exerting surface forces on the fluid, the model describes the effects of the blades by an appropriate body force distribution in the bladed regions of the gas path.

The appropriate force distributions are determined before the unsteady computation is initialized. However, the blade forces depend on the local flow conditions, i.e. the incidence angle, the local Mach number etc. To capture this dependence in the unsteady flow simulations, the body force distribution is described as a function of local flow parameters. The description of this body force dependency is obtained from 3D steady, single-passage calculations.

When the discrete blades are replaced by body force distributions, there is no longer a need for complicated grid topologies with fine mesh resolutions near the blade surfaces. Instead, the computational domain is an axisymmetric, three-dimensional channel bound by the shroud and the hub endwall. Figure 2-1 illustrates the meridional view of this channel. The domain extends from upstream of the impeller leading edge to downstream of the diffuser. The shaded regions of the domain indicate the regions where the body force distributions represent the effects of the impeller and the diffuser blade rows. In this first implementation, the effect of the scroll on the upstream diffuser flow is neglected.

To represent effects of the finite blade thickness, the fractional blade metal blockage is extracted from the 3D geometry and is accounted for in the body force model. This is of particular importance for the simulation of transonic compressors, as transonic flows exhibit substantial changes in Mach number for small changes in flow area [14].

An additional aspect of the unsteady flow in the bladed regions is that flow disturbances (potential, vertical, entropic) cannot redistribute past individual blade passages. To account for this, the flow in the bladed regions of the gas path is modeled to be quasi-axisymmetric. The quasi-axisymmetric flow modeling implies that the blade rows are assumed to consist of an infinite number of thin rubber blades that restrict the redistribution of circumferential flow variations. Flow disturbances are locked to

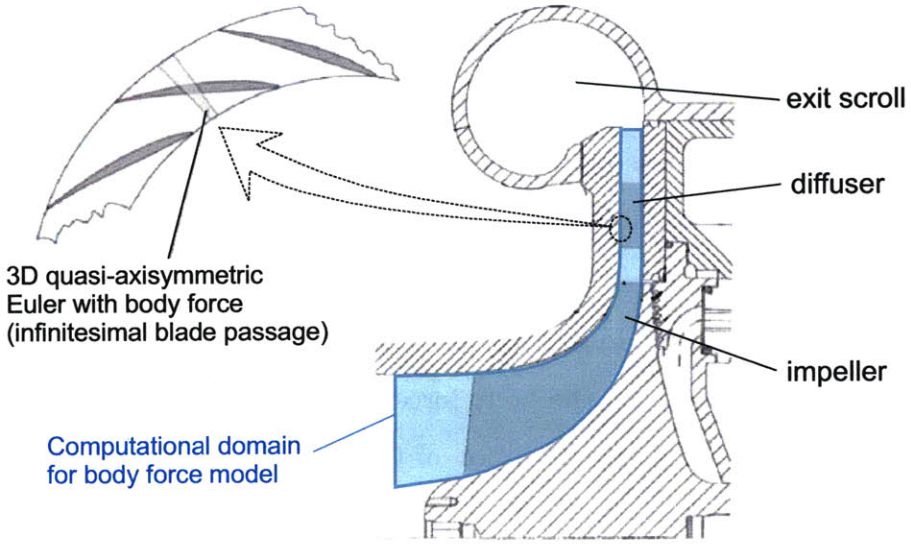


Figure 2-1: Meridional view of computational domain (blue) for the test centrifugal compressor. In shaded regions, the body force distribution representing impeller and diffuser is active.

these infinitesimally thin, deformable channels. As a result, circumferential gradients in the flow quantities do not affect the flow dynamics in the bladed regions. The flows in the neighboring streamtubes are affected by local disturbances only due to the upstream influence and the body force effects. The governing equations for flow in the blade row are obtained by removing the circumferential flow gradients from the Euler equations in the blade row fixed reference frame (see Chapter 4).

The limitations of the flow modeling based on quasi-axisymmetric flow is that single-passage events cannot be captured, as discrete blades do not exist. Modal wave stall precursors, however, have a wavelength much longer than the blade pitch. Therefore, the blade passing frequency is much higher than the frequency associated with the passage of the modal wave structures, such that the quasi-axisymmetric flow modeling is well based for modal wave stall precursors. The simulation of spike-like disturbances with wavelength of a few blade pitches was demonstrated by Gong [12] and is also shown in this thesis.

In summary, the following are the attributes of the new methodology for centrifugal compressor stability prediction:

- The approach can model highly-loaded centrifugal compressors with vaned diffusers and is capable of dealing with both modal and spike stall inception.

- The integrated methodology is of predictive nature in that no empirical correlations or a-priori measurements of the characteristics are required. The body force distributions are extracted from 3D steady, single-passage RANS simulations.

- The definition of the body forces is limited to the flow fields captured by the RANS calculations. As such, the body forces are extrapolated for local flow coefficients lower than the last converged RANS operating point. It will be shown that the RANS based body force description is sufficient to capture the stall inception process. However, full-scale instability cannot be simulated due to the body force limitations.

## 2.3 Technical Roadmap

The technical roadmap is illustrated in Figure 2-2. It represents the thread leading through Chapters 3 and 4. Starting directly with the compressor geometry, 3-D steady single-passage RANS simulations are carried out first. The computational domain contains one impeller main blade, one splitter blade, and one diffuser vane. Steady-state flow fields are computed for several operating points. Section 3.1 provides detail on these simulations. The steady simulation results are validated by comparison to experimental measurements before moving on to the body force extraction.

The passage flow fields from the RANS calculations contain the inviscid and viscous effects of the blades for different flow conditions. Each of the flow fields is appropriately averaged in the circumferential direction. The method is based on a control volume approach and extracts the body force components at different axial and radial locations as described in Section 3.3. For each operating point, this extraction results in a body force field in the meridional plane. The force fields for a centrifugal compressor with vaned diffuser are analyzed in Section 3.3.5. The data

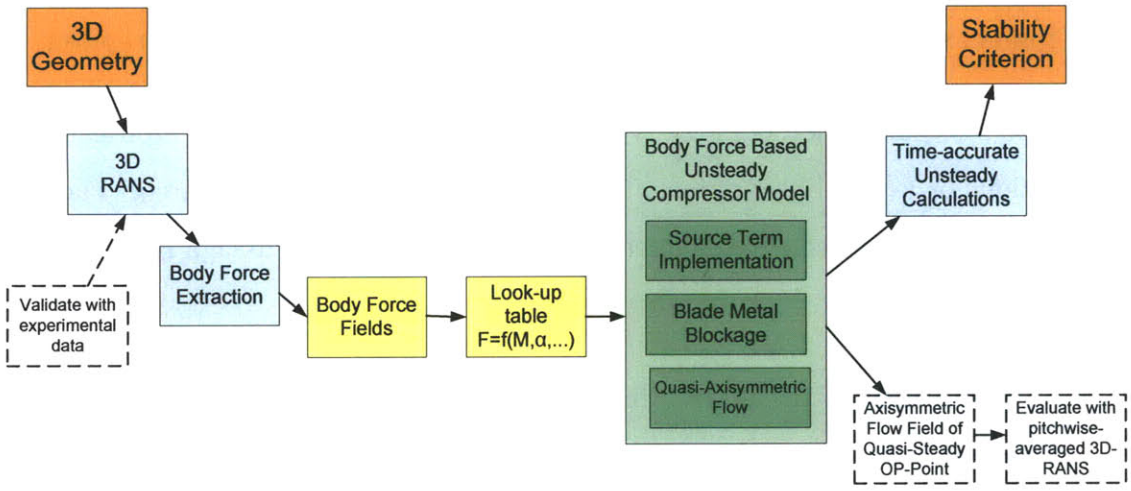


Figure 2-2: Technical Roadmap of the centrifugal compressor stability prediction methodology. From 3D geometry (left) to a stability criterion (right)

from all force fields are then combined into a body force look-up table. The look-up table provides the body force components at a given location in the compressor as a function of the local flow parameters. Details are discussed in Section 3.4.

The information from the look-up table is fed into the body force based, unsteady compressor flow model. It represents the central element of the methodology and will be referred to as the body force model in this thesis. The three main features of the body force model are: (1) the effects of the blades on the flow field are modeled by body force source terms acting on the fluid mass. The magnitudes of the force components are functions of the local flow parameters. The functional relationship is defined by the look-up table; (2) in the bladed regions of the gas path, the quasi-axisymmetric flow modeling prevents disturbances from redistribution in the circumferential direction; and (3) to represent the effects of the finite blade thickness, the blade metal blockage is accounted for.

Chapter 4 provides detail on the flow modeling. The governing equations for the bladed regions and regions without blades are derived and the implementation of the model in an existing Euler solver is discussed.

Steady operating points are calculated with the body force model and compared

to the circumferentially averaged flow fields from the 3-D RANS simulations to validate the methodology. Finally, time-accurate simulations of the entire centrifugal compressor are performed using the body force model. The stall inception point and the stall inception pattern are investigated with the future goal of establishing a stall inception criterion for centrifugal compressors with vaned diffusers.

# Chapter 3

# Derivation of Body Force Distribution from 3-D RANS Calculations

This chapter discusses the methods used to define the required force description from the compressor geometry. While the methods are formally introduced, they are applied to a test compressor for validation purposes. The test compressor, a highly-loaded centrifugal compressor of advanced design, is the same as that used in the experiments by Spakovszky and Roduner [29]. This approach allows the validation with experimental measurements at various steps in the development of the methodology.

The first step to assess the effects of the blades on the flow field at different flow conditions is to perform a sequence of single-passage, steady RANS simulations at different operating conditions. Section 3.1 explains the setup and presents the results for the test compressor geometry. Using appropriate exit boundary conditions, converged flow fields were achieved at mass flows lower than the peak of the pressure rise characteristic. It is critical to capture operating points with positive slope of the characteristic, as the corresponding flow features are important in the instability inception process. It will be shown that overall good agreement between simulations and experiments is found capturing the trends in the global performance and in

the diffuser subcomponent characteristics that are important for the stall inception. Discrepancies at the impeller-diffuser interface due to the presence of the mixing plane in steady RANS calculations are discussed.

Given the viscous flow field solutions from the steady RANS calculations, the body force representations of the blades under different operating conditions are extracted. The extraction method is explained in Section 3.3. The body force field for an operating point near design is analyzed. On the basis of this analysis, the features of the body force field that represent the blades in a centrifugal compressor with vaned diffuser are described.

Finally, the body force fields for different operating points are processed to define a body force look-up table, which describes body force components as functions of local flow parameters. Limitations of the available range in flow parameters are discussed and a simple approximation is introduced to describe the forces outside the available range. The results shown in Sections 3.3 and 3.4 serve as inputs to the body force model described in Chapter 4.

## 3.1 Steady, Single-passage RANS Simulations

This section describes the setup of the viscous flow simulations used to obtain the passage flow fields. Later in this chapter the resulting flow fields are analyzed to extract the required body force distributions for the body force model.

The test compressor, used to validate the methods throughout the thesis, is first described. Next, the computational tool, the numerical method and the setup are outlined. Finally, the results for the test compressor are analyzed and compared to experimental measurements by Spakovszky and Roduner [29].

### 3.1.1 Test Compressor Definition

For the validation of the methods outlined in this thesis, the pre-production centrifugal compressor stage used in the experiments by Spakovszky and Roduner [29] was chosen. The stage is representative of a modern turbocharger compressor of advanced

design. The centrifugal compressor with vaned diffuser has a pressure ratio of 5. At design, the impeller tip Mach number exceeds unity. The impeller consists of 9 main blades and 9 splitter blades, while the diffuser has 16 diffuser vanes. More information on the test compressor and the experimental measurement can be found in [29].

### 3.1.2 CFD Tool Description

All 3-D viscous flow simulations to obtain the steady compressor flow fields were carried out using the commercially available software package Fine/Turbo by Numeca. Fine/Turbo is an integrated CFD package tailored for turbomachinery applications. The package includes tools for grid generation, flow solving, and post-processing.

For computational speed and numerical accuracy Fine/Turbo solely uses structured hexahedra grids. Therefore, the simulation of the flow field in complex centrifugal compressor geometries requires multi-block grid topologies. The automated grid generator, Autogrid, enables the grid generation for turbomachinery applications with little user input. The graphical user interface, FINE, allows setting the simulation parameters and controls the flow solver Euranus. Euranus supports parallel computation on multiple processors and the "multigrid" technique. In a multigrid solver, multiple sweeps between the fine mesh and coarsened grid levels are performed within each iteration. This technique reduces low frequency errors on coarse grid levels and accelerates the convergence by multiple orders of magnitude [1]. The post-processing tool, CFView, processes the resulting flow solutions using a graphical user interface or automated Python scripts. A more detailed description of the software package can be found in [18].

### 3.1.3 Computational Procedure

The software tool is used to perform steady, single-passage RANS simulations solving the viscous Reynolds Averaged Navier-Stokes equations. The governing equations contain an apparent stress term due to the fluctuating velocity field, generally referred to as Reynolds stress. The Spalart-Almaras turbulence model is applied to

approximate the Reynolds stress terms.

The computational domain is depicted in Figure 3-1. To lower the computational requirements, it contains only one impeller main blade, one splitter blade, and one diffuser vane. Periodic boundary conditions are applied to simulate the flow through a blade row of identical blades. The multi-block grid consists of 23 individual, structured grid blocks with a total cell count of approximately one-million cells.

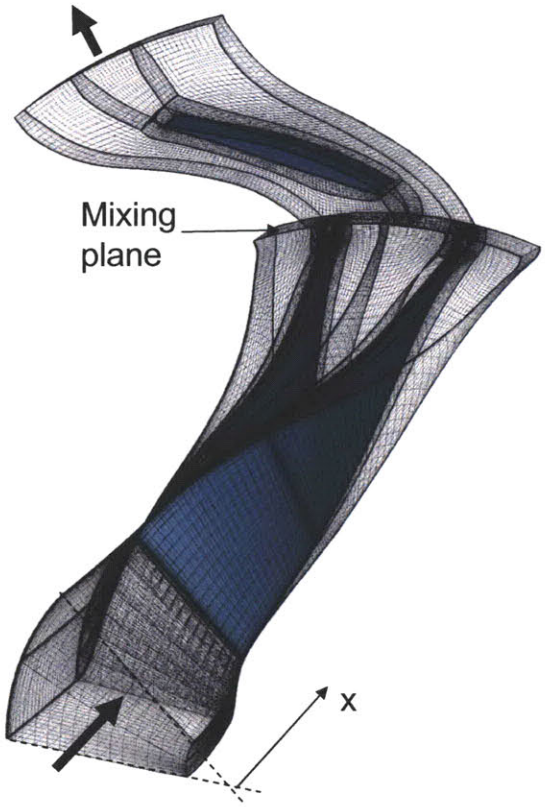


Figure 3-1: FineTurbo grid for steady single-passage RANS simulations of test centrifugal compressor.

At the interface between the exit of the impeller domain and the inlet of the downstream diffuser domain, a mixing plane formulation transmits information between the rotating impeller frame and the stationary diffuser frame. The mathematical details of this formulation are omitted here (see [18] for details) and a short description is given instead.

The mixing plane approach introduced by Denton and Singh [7] has been widely used due to its efficiency in simulating blade-row interaction with a steady calculation.

Steady simulations of centrifugal compressors using this approach can be seen as coupled simulations of impeller and diffuser, which exchange boundary conditions at the interface [6]. The downstream diffuser side is treated as an inlet face with the boundary conditions being defined by the averaged flow properties at the impeller exit. The upstream impeller side can be seen as an outlet face with the exit flow condition being provided by the diffuser inlet flow. For the time marching scheme, the boundary conditions evolve as the scheme proceeds towards the steady-state solution. The approach neglects the unsteady effects of the impeller-diffuser interaction and induces an error generated by the artificial mixing process at the interface [6]. The effects on the flow in a highly-loaded centrifugal compressor are discussed together with the results in Section 3.2. To capture the global performance of the compressor correctly, a flux-based mixing plane formulation is used. It ensures that the mass, momentum, and energy flows across the impeller-diffuser interface are preserved (see [6] for details).

### 3.1.4 Boundary Conditions

At the inlet of the domain the total temperature and the total pressure are specified. The inlet flow direction is defined to be purely axial. At all solid surfaces of the compressor, no-slip conditions are applied. The impeller blades and the hub endwall of the impeller are defined as rotating surfaces. All other surfaces including diffuser vane, shroud, and the hub endwall in the diffuser are formulated as stationary surfaces.

The type of exit boundary condition was chosen depending on the operating point. For operating points between choke and design point, the averaged static pressure at the domain outlet was defined. Static pressure exit boundary conditions are commonly used in internal flow CFD applications. However, this type of boundary condition can lead to convergence problems in turbomachinery applications. For example, previous work by Hill [16] showed that, as the slope of the compressor pressure rise characteristic approaches zero, the compression system becomes statically unstable and the computation diverges. To improve the convergence at operating points with flow coefficients lower than at design conditions, a mass flow exit boundary condi-

tion was applied. As will be shown in Section 3.2, the application of the mass flow boundary condition allows the simulation of operating points beyond the peak of the pressure rise characteristic. The resulting flow fields are critical for the description of the body forces, as the flow features at low flow coefficients are important in the instability inception process.

To validate the use of the mass flow boundary condition, identical operating points were successively simulated using static pressure exit boundary conditions and mass flow exit boundary conditions. The analysis of global performance and flow details demonstrated that the resulting compressor flow field is not affected by altering the type of exit boundary condition. Figure 3-2 shows that Mach number and total pressure profiles in the diffuser are in good agreement between the two cases.

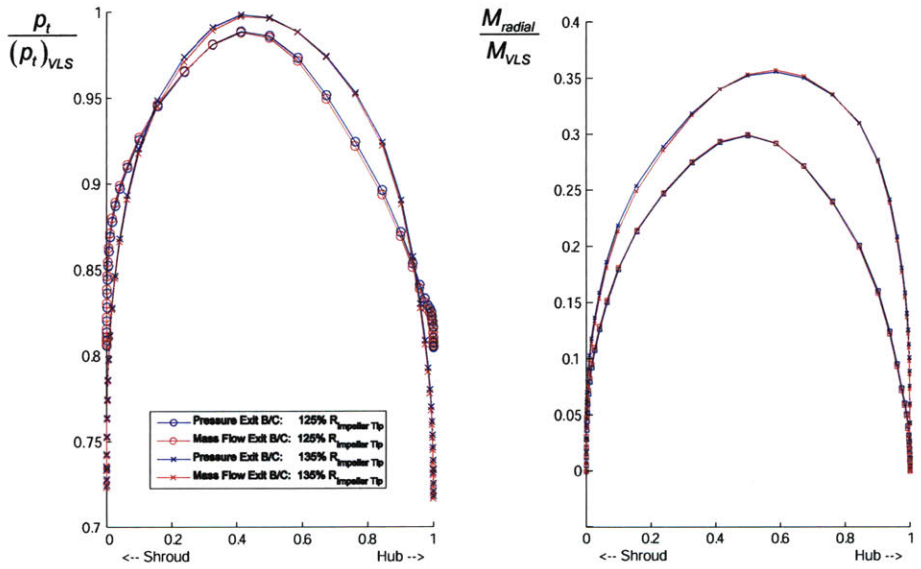


Figure 3-2: Comparison of diffuser flow profiles at 125% and 135% impeller tip radius between simulations using static pressure exit boundary condition and mass flow exit boundary condition.

## 3.2 Discussion of RANS Results

This section analyzes the results from the single-passage, steady RANS simulations. First, the overall compressor performance is assessed by comparing the stage pressure

ratio characteristic to experimental measurements. Next, the diffuser subcomponent behavior is analyzed and the impact of the mixing plane is described.

To obtain a wide range of flow conditions for the body force look-up table, a total number of 64 operating points between the choke and stall point on four different speedlines were simulated. These operating points provide a sufficient range of flow conditions to establish the body force look-up table describing the body forces as a function of local flow conditions.

As will be discussed in the following subsections, the results suggest that the obtained flow fields can be used to determine the blade forces for different flow conditions.

### 3.2.1 Stage Pressure Ratio Characteristics

The simulated compressor characteristics at 78%, 95%, 100%, and 105% design speed are illustrated in Figure 3-3. The blue crosses indicate operating points for which converged, steady flow solutions were found. It is important to note that the last operating point at low mass flow is where numerical divergence begins rather than the physical onset of instability. The goal of the approach in this thesis is to establish and to demonstrate a methodology that captures the stall point as measured in the experiments.

To assess the accuracy of the simulation, the experimentally determined characteristic at design speed is added as the green circles. In the experimental data, the last green point represents the experimentally measured stall point. The comparison illustrates that converged solutions cannot be obtained for low mass flows. In addition, the simulation overestimates the stage pressure ratio by approximately 5-8%. The calculations agree with the experimental data, in that the characteristic flattens out towards the stall point. The trend in the slope of the characteristic is captured reasonably well.

One reason for the difference between simulation results and the measurements is the use of the mixing plane approach at the impeller-diffuser interface. As described in the following section, the mixing plane approach mismatches the impeller and

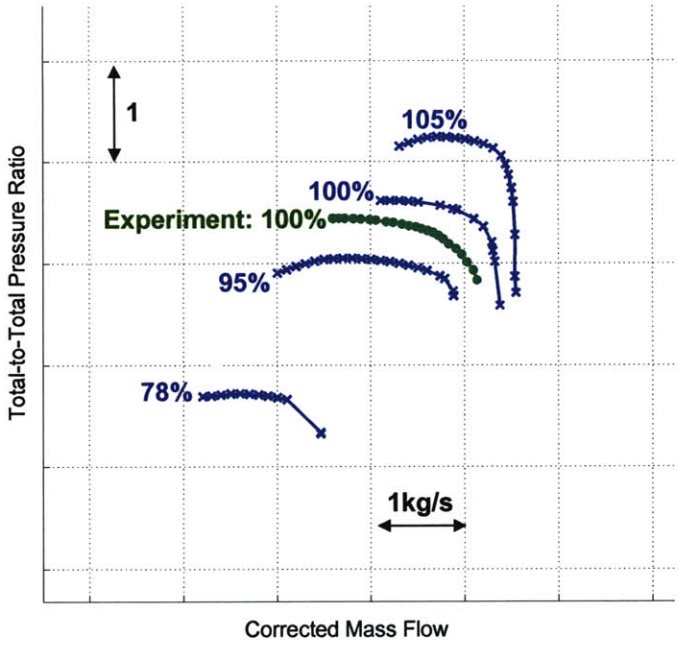


Figure 3-3: Total pressure ratio characteristics of the test compressor. Comparison between RANS simulation and experimental results.

diffuser, which can have an impact on the global performance.

A second difference between simulation and experiment is the compressor configuration. The experimental device includes a volute downstream of the diffuser and the exit total pressure is measured at the exit of the volute. In the simulation, however, the computational domain ends downstream of the diffuser and the total pressure is determined at the domain outlet. This might reduce the stagnation pressure loss in the simulation leading to a higher stage pressure ratio.

It is important to note that the objective of the methodology is to capture the stall inception rather than to predict the design performance. As shown by Hunzinker and Gyarmathy [17] and by Spakovszky and Roduner [29], the critical metrics for the stability analysis of centrifugal compressors with vaned diffuser are the subcomponent pressure rise characteristics.

### 3.2.2 Diffuser Subcomponent Performance / Mixing Plane

This section compares the diffuser subcomponents pressure rise characteristics between experiment and simulations. Experimental data for the test compressor are available from Spakovszky and Roduner [29]. To dissect the performance of the subcomponent in the experiment, one diffuser channel was instrumented with static pressure taps in the vaneless space, the semi-vaneless space, the diffuser passage and downstream of the diffuser vanes. The locations of the pressure taps in the hub endwall are shown in Figure 3-4.

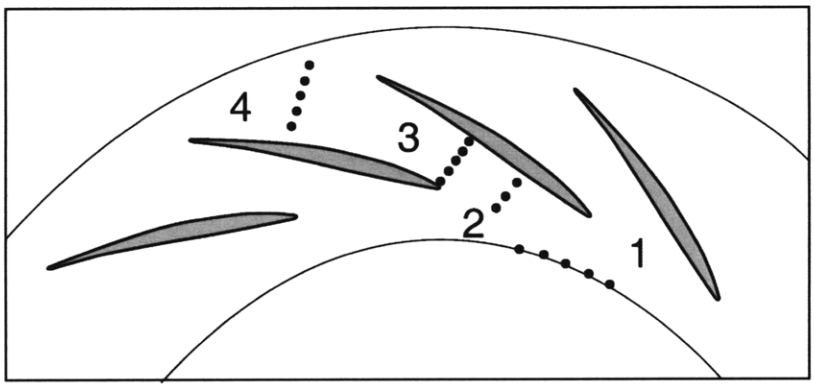


Figure 3-4: Locations of static pressure taps in the diffuser. Figure adopted from [29].

The vaneless space is the space between the impeller exit (Station 1) and the diffuser leading edge (Station 2). Downstream of the vaneless space, the semi-vaneless space is defined between station 2 and the throat of the diffuser passage (station 3). The diffuser passage extends from station 3 to 4.

To investigate whether the diffuser flow is captured correctly by the RANS simulations, the subcomponent characteristics from the simulation are plotted in comparison with the experimental data in Figure 3-5. A consistent comparison is obtained by determining the pressure rise in the simulation using the static pressure at the locations of the physical pressure taps in the experiment.

Near the design point, i.e. approximately in the center of the flow range plotted, the pressure rise of the subcomponents is in good agreement with the experiment. However, the slope of the characteristics does not follow the experimental results near

stall. In the data from the simulation, the pressure rise characteristic in the semi-vaneless space reaches a maximum and changes to a positive slope at low mass flow. As a consequence, the semi-vaneless space is destabilized and becomes the weakest element in the compression system. This suggests that a mismatching between impeller and diffuser in the simulation has a destabilizing effect on the compression system, which can yield the growth of long-wavelength stall precursors.

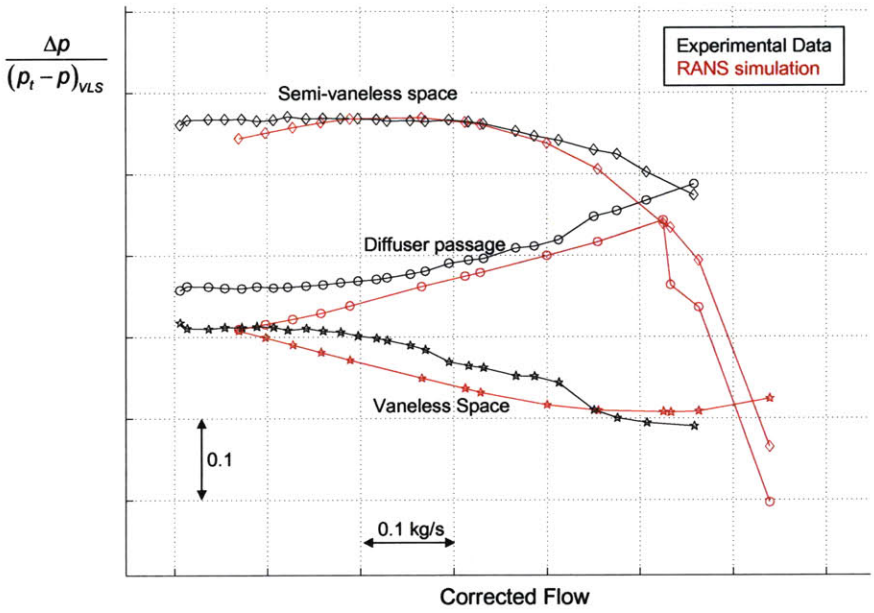


Figure 3-5: Static pressure rise in diffuser subcomponents. Comparison between simulation using flux-based mixing plane approach and experimental results at 100% corrected impeller speed.

The work by Everitt [10] demonstrates that the mismatching of impeller and diffuser in the simulation is introduced by the mixing plane approach in the steady Fine/Turbo simulations. Figure 3-6 and 3-7 compare the flow field near stall from the simulation with Numeca's flux-based mixing plane and an isolated diffuser calculation that invokes the appropiate momentum-averaged flow angle at the diffuser inlet. The comparison shows that the Mach number contour is strongly altered by Numeca's flux-based mixing plane. As a result, the diffuser operating point is altered and the matching between impeller and diffuser is changed. A region of excessively high Mach number on the pressure side and a large flow separation on the suction surface are

observed in the mixing plane result in Figure 3-6. The flow separation decreases the pressure recovery in the diffuser passage at low flow as indicated in Figure 3-5.

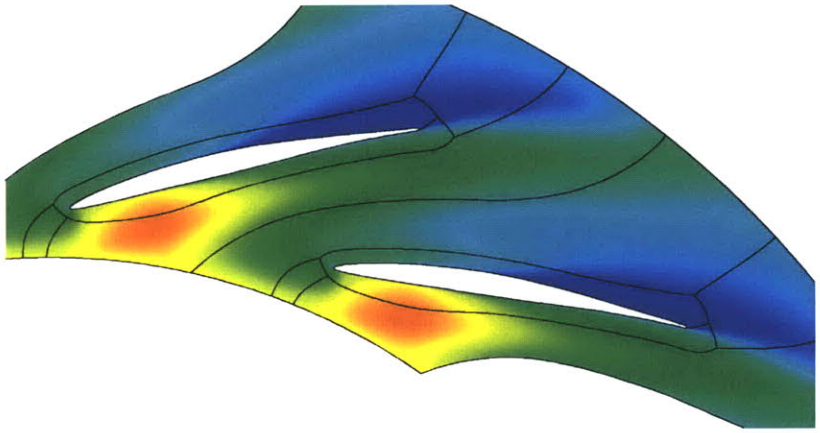

Figure 3-6: Mach number contour plot in vaned diffuser extracted from single-passage stage calculation with flux-based mixing plane implementation.

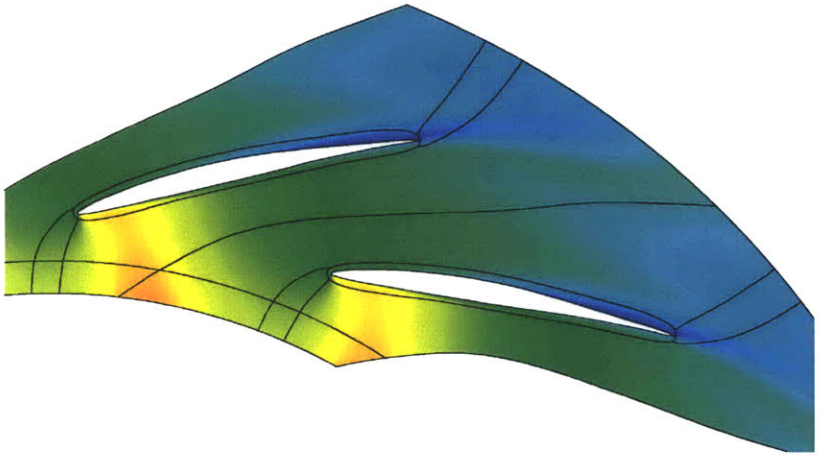

Figure 3-7: Mach number contour plot in vaned diffuser extracted from isolated diffuser simulation by Everitt [10]. Simulated stage operating point is identical to Figure 3-6

## 3.3 Body Force Extraction Method

This section outlines the extraction of the body forces from the 3-D single-passage RANS calculations for a specific operating point. First, a control volume analysis approach is developed to extract the blade forces from detailed compressor flow fields. Then, the resulting body force distribution is discussed for an operating point near

the design point. The force distributions serve as the inputs to the body force look-up table discussed in Section 3.4.

### 3.3.1 Control Volume Approach

As discussed in Section 2.3, the body force approach requires a description of the force components for each axial and radial location in the computational domain. At each location in the meridional plane, a control volume analysis of an angular segment is performed to obtain the body force components. The flow field quantities are taken from the 3-D RANS simulations. As an example, Figure 3-8 illustrates a control volume at midspan near the impeller exit.

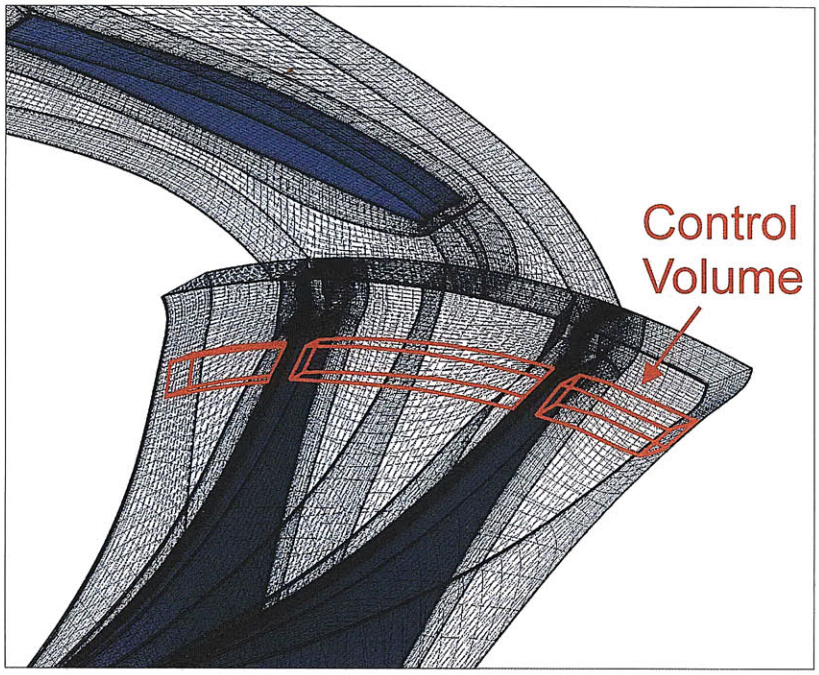


Figure 3-8: Sketch of control Volume for extraction of body force near impeller exit.

For each angular control volume the steady momentum equation is applied in cylindrical coordinates:

$$\iint_S \left(\rho \vec{U} \cdot d\vec{S}\right) \vec{U} = -\iint_S p \cdot d\vec{S} + \underbrace{\vec{F}_{Blade\ Passage}}_{\iiint_V \rho \vec{f}\, dV} \cdot \tag{3.1}$$

The momentum flux terms and the pressure terms are numerically evaluated on

the free surfaces using the flow field data. From Equation (3.1), the body force vector $\vec{f}$ can be determined according to

$$\vec{f} = \frac{\iint_S \left(\rho \vec{U} \cdot d\vec{S}\right) \vec{U} + \iint_S p \cdot d\vec{S}}{\iiint_V \rho dV} \tag{3.2}$$

The body force vector $\vec{f}$ represents the inviscid and viscous forces on the blade surfaces evenly distributed over the mass in the control volume. The extraction method is consistent with the body force implementation in the unsteady compressor flow model described in Chapter 4.

Since the method extracts an axisymmetric body force field for a given operating point, the control volume analysis is simplified to a two-dimensional analysis and the body force components are extracted from a circumferentially-averaged flow field.

To account for the circumferential variation of the flow quantities in the two-dimensional analysis, the flow field is averaged using the blade force averaging method introduced by Kiwada [20]. This averaging method preserves the momentum fluxes across the faces of the control volume. In addition, the fluid volumes and the free surface areas of the control volumes in the bladed regions are reduced due to the finite blade thickness. This reduction is accounted for by the blade metal blockage. The following two subsections discuss the blade force average and the blade metal blockage in more detail.

### 3.3.2 Blade Force Average

Figure 3-9 shows two equivalent control volumes. On the left side, the total flux through the upper surface is calculated from the circumferentially non-uniform flux distribution. On the right side, the flux through this surface is expressed from the circumferentially averaged flux distribution in the meridional plane. To ensure the consistency between the fluxes in the two representations, the average is defined by

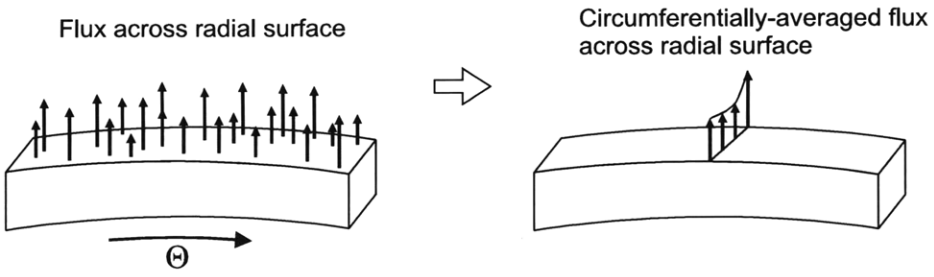


Figure 3-9: Flux evaluation on cell faces using blade force average.

$$\bar{H} = \frac{\int\limits_A H dA}{\int\limits_A dA} \tag{3.3}$$

, where $H$ is a generic flux quantity.

The calculation of the momentum flux on the control surface requires the averages $\overline{\rho V_r^2}, \overline{\rho V_\theta^2}, \overline{\rho V_x^2}, \overline{\rho V_r V_x}, \overline{\rho V_r V_x}, \overline{\rho V_\theta V_x}$. Note that $\overline{\rho V_r^2} \neq \bar{\rho} \cdot \overline{V_r} \cdot \overline{V_r}$, such that higher order terms are not captured in a simple area-averaged flow field. The formulation here is based on the average fluxes and is thus referred to as blade force average. The circumferentially averaged pressure $\bar{p}$ is calculated to determine the pressure terms on the surfaces. To compute the mass in the control volume, the circumferentially averaged density $\bar{\rho}$ is also determined. As a result, the knowledge of eight circumferentially averaged flow quantities in meridional plane is sufficient to compute the blade forces consistently.

### 3.3.3 Blade Metal Blockage

The second aspect that has to be accounted for is the reduction in free surface areas and fluid volumes of the control volumes due to the presence of the compressor blades. As shown in Figure 3-10 and captured by Equation 3.4, the blade metal blockage, $\lambda$, for a given axial and radial location is defined as the ratio of the flow channel width in circumferential direction and the blade pitch.

$$\lambda = \frac{r\left(\theta_{SS} - \theta_{PS}\right)}{S} \tag{3.4}$$

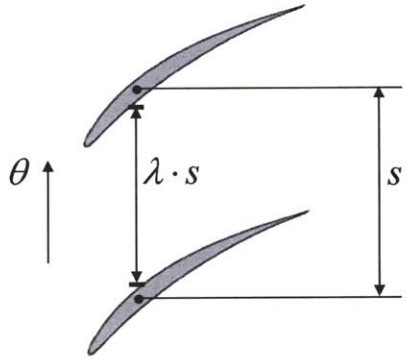


Figure 3-10: Definition of blade metal blockage $\lambda$.

The blade metal blockage was determined for the test compressor based on the geometric blade definitions and is illustrated in Figure 3-11. The leading and trailing edges of main impeller blade, splitter blade, and diffuser are indicated by jumps in blockage value. High values of blockage are near the root of the impeller blades, where the blade thickness is the largest.

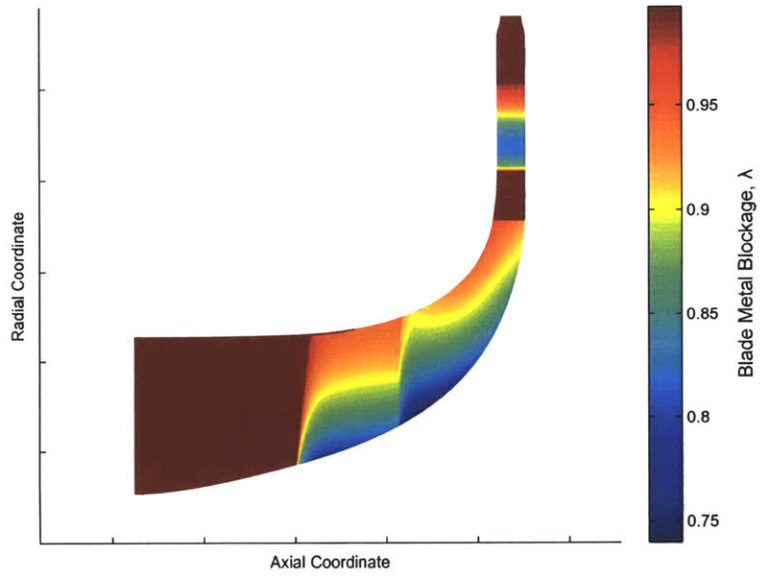


Figure 3-11: Blade metal blockage for test compressor.

The accounting for blade metal blockage in the control volume analysis here is

different from the method by Kiwada [20] in that it accounts for the blade metal blockage by appropriately changing the geometry of the control volume consistent with the body force model described in Chapter 4. In the previous method the differential form of the governing equations (Equations 4.3) was integrated over the entire angular volume including the blade metal volume. This led to numerical inaccuracies at the blade leading and trailing edges.

The method described here is based on the control volume form of the steady momentum equations (see Equation 3.1). The blockage is accounted for by appropriately modifying the volume and surface area terms of the control volume.

### 3.3.4 Numerical Integration

The objective of the body force extraction methodology is to obtain the body force components for each cell in the body force based unsteady diffuser model from the single-passage, steady RANS flow fields. Figure 3-12 illustrates the different grids used in the extraction method. From the single-passage RANS simulation, the flow fields are available on a high resolution, 3-D mesh.

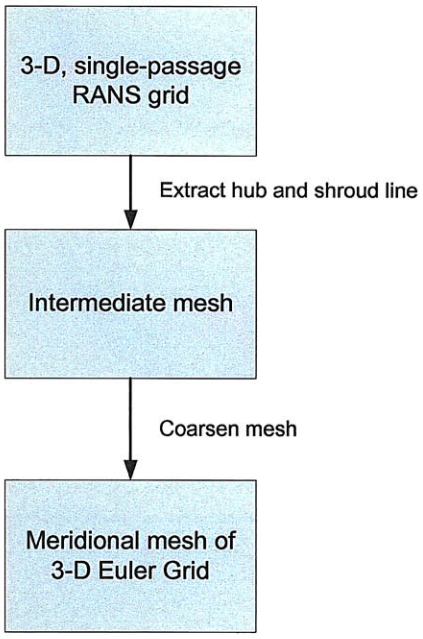


Figure 3-12: Grids used in body force extraction method.

This flow field is circumferentially averaged on the intermediate mesh. The inter-

mediate mesh is identical to the meridional mesh of the 3-D Euler grid used by the body force model, but it is six times finer. The resolution factor between intermediate mesh and meridional mesh of the 3-D Euler grid is chosen so that the resolution of the intermediate mesh is comparable to the RANS grid, preserving the flow field fidelity during the body force extraction.

As shown in Figure 3-13, 36 data points are available on the intermediate mesh to calculate the mass in each cell. Six data points are available on each control volume face of the cell to calculate the flux and pressure terms.

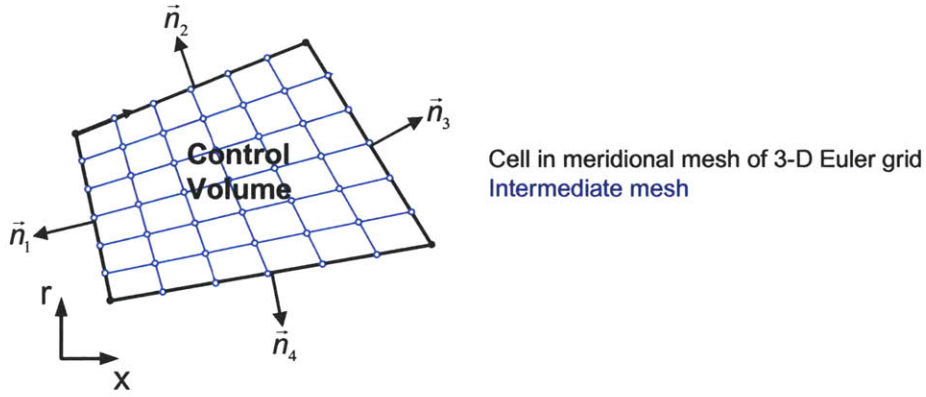


Figure 3-13: Two-dimensional representation of control volume for body force extraction method for a generic cell in meridional mesh of 3-D Euler grid.

### 3.3.5 Body Force Distribution Near Design Point

The methodology derived in Section 3.3 is applied to the flow fields from the steady RANS simulations. For each operating point an axisymmetric body force field is extracted. The features of this body force field for an operating point near design conditions are presented and discussed here. Emphasis is placed on interrogating the body force components based on first principles.

Figure 3-14 depicts a vector plot of the axisymmetric body force distribution. An annular segment of the compressor gas path between hub and shroud is depicted and the force vectors at midspan are illustrated. The quantitative variation of the radial, tangential, and axial force components in the streamwise direction are shown

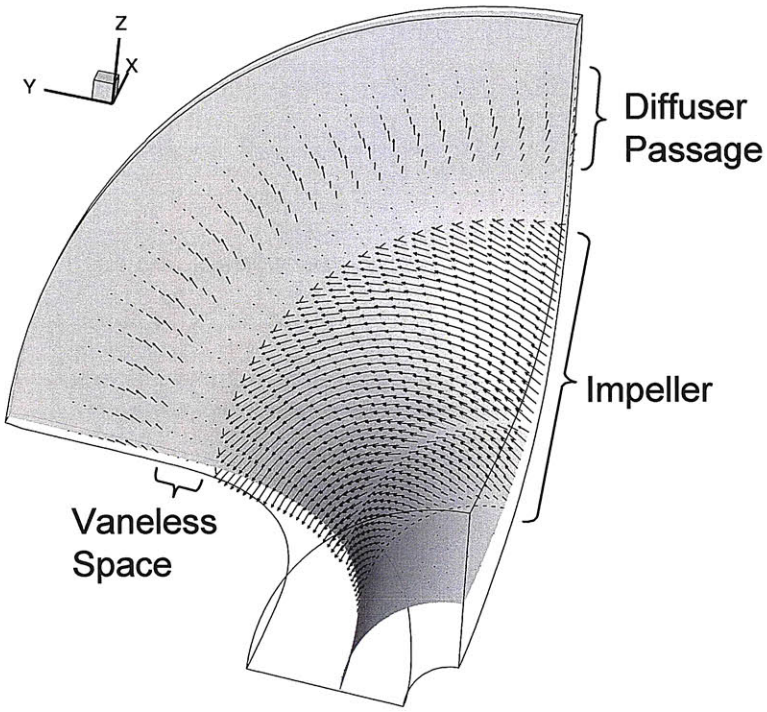


Figure 3-14: Axisymmetric representation of body force vectors at midspan for an operating point near design conditions.

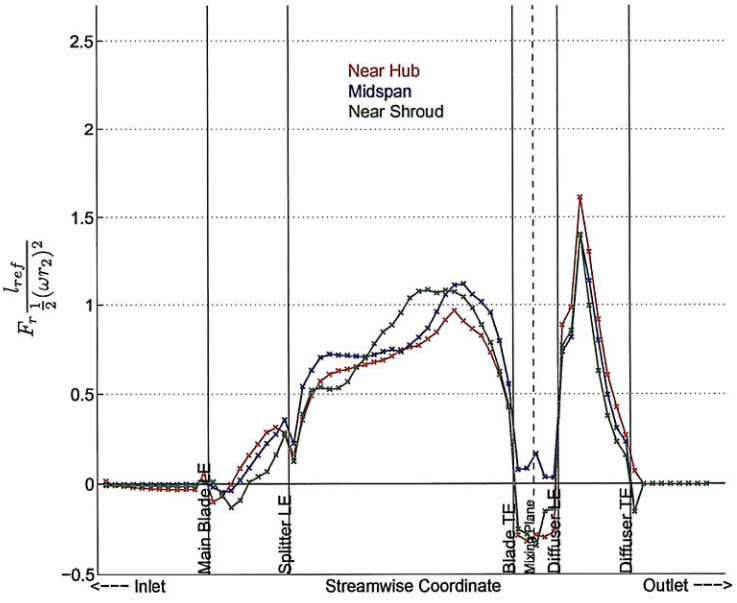


Figure 3-15: Radial body force component along the channel from inlet to outlet of the computational domain.

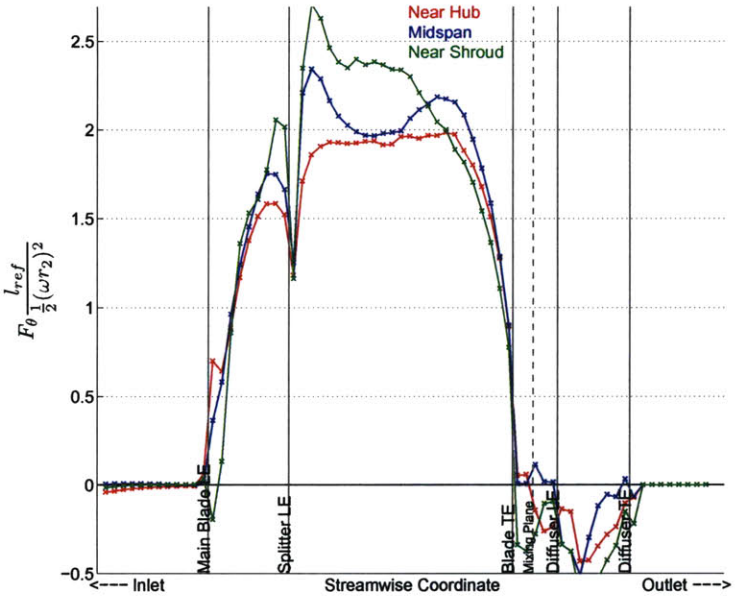


Figure 3-16: Tangential body force component along the channel from inlet to outlet of the computational domain.

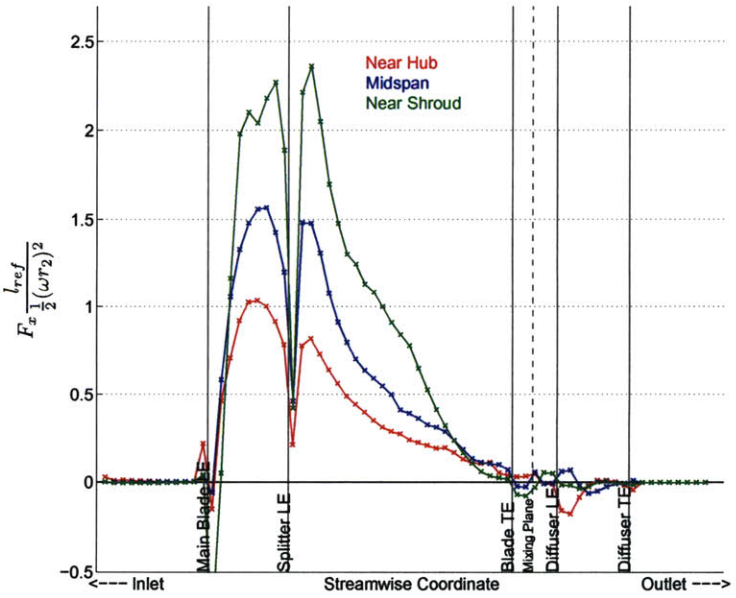


Figure 3-17: Axial body force component along the channel from inlet to outlet of the computational domain.

in Figures 3-15 to 3-17. The left end of the plots shows the values at the domain inlet while the right end represents the outlet of the computational domain. The leading and trailing edges of each blade row are also marked.

From conservation of momentum, the body forces per unit mass scale with $\frac{U_{ref}^2}{l_{ref}}$. Thus, the body forces are non-dimensionalized according to $\frac{F \cdot l_{ref}}{\frac{1}{2} U_{ref}^2}$ where $l_{ref}$ is taken to be the gas path length of the compressor and $U_{ref}^2$ is the impeller tip speed $\omega r_2$. The factor $\frac{1}{2}$ is introduced to relate to the impeller tip kinetic energy.

High tangential body forces in the impeller passage are seen in Figures 3-14 and 3-16. These forces represent the flow turning in the absolute frame from purely axial flow upstream of the impeller to a transonic, highly-swirling flow at the impeller exit, which yields the addition of angular momentum. From the Euler turbine equation, this increase in angular momentum leads to the addition of work by the impeller. The tangential body force is increased where the flow is additionally guided by the splitter blade.

The inlet of the impeller, the inducer, is characterized by a combination of high axial and tangential force components. The axial force component increases from hub to shroud. Both aspects are in agreement with results by Kiwada [20] for an axial compressor rotor. In the radial part of the impeller passage, the main force direction is tangential. Additionally, a force component in the radial direction exists in the impeller passage due to the backswept blades.

At the outer end of the rotating impeller passage, there is no pressure difference between suction and pressure side due to the Kutta condition. An adjustment takes place near the end of the passage to decrease the pressure difference across the channel [14]. Due to the decreased pressure difference, the Coriolis force in the rotating frame of reference drives the flow towards the pressure side. The resulting relative velocity in the direction opposite to the direction of rotation leads to the slip effect. The decreased pressure difference is captured in the body force distribution. Radial and tangential force components decrease towards zero near the impeller trailing edge.

The diffuser blades take out the swirl of the flow leaving the impeller. This is represented by a tangential force component with a direction opposite to the impeller

rotation and a component in the radial direction (see Figure 3-14). The force vectors in the diffuser are perpendicular to the local flow direction, indicating that no work is added to the fluid. Because the diffuser blades are prismatic, the body forces throughout the diffuser passage are approximately uniform across the span.

Outside the blade passage, the body forces essentially vanish. As a result, the inlet region upstream of the impeller leading edge, the vaneless space, and the outlet region downstream of the diffuser cascade are approximately body force free. Small force components occur in the vaneless space due to the highly non-uniform, swirling flow leaving the impeller. Mixing of non-uniform flow and viscous effects between parallel streamtubes lead to relatively small force magnitudes.

## 3.4 Definition of a Body Force Look-Up Table

The previously discussed body force extraction method yields an axisymmetric body force field corresponding to a single steady-state flow field. To capture the dynamic behavior in the unsteady, non-axisymmetric flow simulations, the body forces need to react to the local flow conditions. The objective is thus to express the forces at each location in the compressor domain as a function of local flow conditions. This section introduces a look-up table approach that uses the information of the available axisymmetric body forces fields to build up a functional dependence between body force and local flow conditions.

### 3.4.1 Local Flow Parameter Dependence

The non-dimensional flow parameters that can influence the blade forces are the Reynolds number, the flow angles, and the Mach number. For the high Reynolds number turbomachinery flow, Reynolds number effects can be neglected. The flow direction in the three-dimensional domain can be described by the swirl angle $\alpha$ and the pitch angle $\beta$. The swirl angle $\alpha$ is defined as the angle between the velocity vector and the meridional plane, while the pitch angle is defined in the meridional plane as the angle between the channel centerline and the velocity vector, as illustrated in

Figure 3-18.

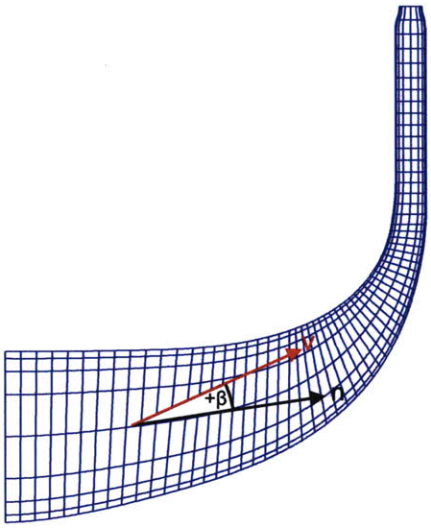


Figure 3-18: Definition of the pitch angle $\beta$. $\beta > 0$ indicates flow towards the shroud, while $\beta < 0$ indicates flow towards the hub.

It was determined from the 3-D RANS calculations that the velocity component towards hub or shroud is small compared to the velocity component parallel to the channel centerline, yielding pitch angles $\beta$ close to zero. Given the small variation in $\beta$ and the low sensitivity of the forces to variations in the pitch angle $\beta$, the pitch angle influence on the forces is small. As a result, the body forces at a given location in the flow field are mainly governed by the local Mach number M and the local swirl angle $\alpha$.

Two look-up table approaches were developed and tested in the body force model. The first one describes the force components directly as functions of the two independent input parameters, the local swirl angle, $\alpha$, and the local Mach number, M. An advanced inter- and extrapolation scheme, the so-called Spatial Kriging Estimation method (see [3] for details), was implemented to estimate the body force components for a generic range of Mach numbers and flow angles. The advantage of this look-up table approach is that it independently captures the effects of variations in relative local flow angle and relative local Mach number. If a sufficient range of flow conditions is available from the RANS simulations, this is the preferred method.

In the testing phase, it was discovered that the range of flow conditions obtainable from the previously performed steady 3-D RANS simulations is limited and insufficient for the 2-D look-up table approach. While solving the flow field, the body force model required the body forces for local flow parameters outside the range of flow angles and Mach numbers covered by the look-up table. The details of the 2-D look-up table and the related challenges are discussed in Appendix A.

### 3.4.2 Force Description Based on Meridional Mach Number

To use the available data more effectively, a simplified, one-dimensional look-up table approach was developed. It is based on the local Mach number in the meridional plane $M_m$. This approach combines the effects of the local Mach number and the local swirl angle in a single parameter. It is similar to the local flow coefficient approach that has been used in previous body force based models for incompressible flow [11].

For each operating point from the 3-D RANS simulations and each location in the meridional plane, the force components and the local meridional Mach number were extracted. The functional dependence between each of the force components and the meridional Mach number is found by interpolation between the data points available for the selected impeller speed.

Figures 3-19 to 3-21 show the body force as a function of the meridional Mach number at midspan near the impeller inlet, near the impeller exit, and in the diffuser passage. Each figure illustrates separately the dependence of the radial, tangential, and axial force components on the local meridional Mach number. The crosses mark the data points for which the force components are known from the body force extraction of 3-D RANS flow field. In the characteristics, the operating point closest to stall is at the left end of the characteristic, while operating points close to choke are on the right.

The trend of the force characteristics is similar for the three simulated speedlines. The force components are non-dimensionalized by the reference length and the impeller tip speed. The magnitude of the force components scales with the square of the impeller speed.

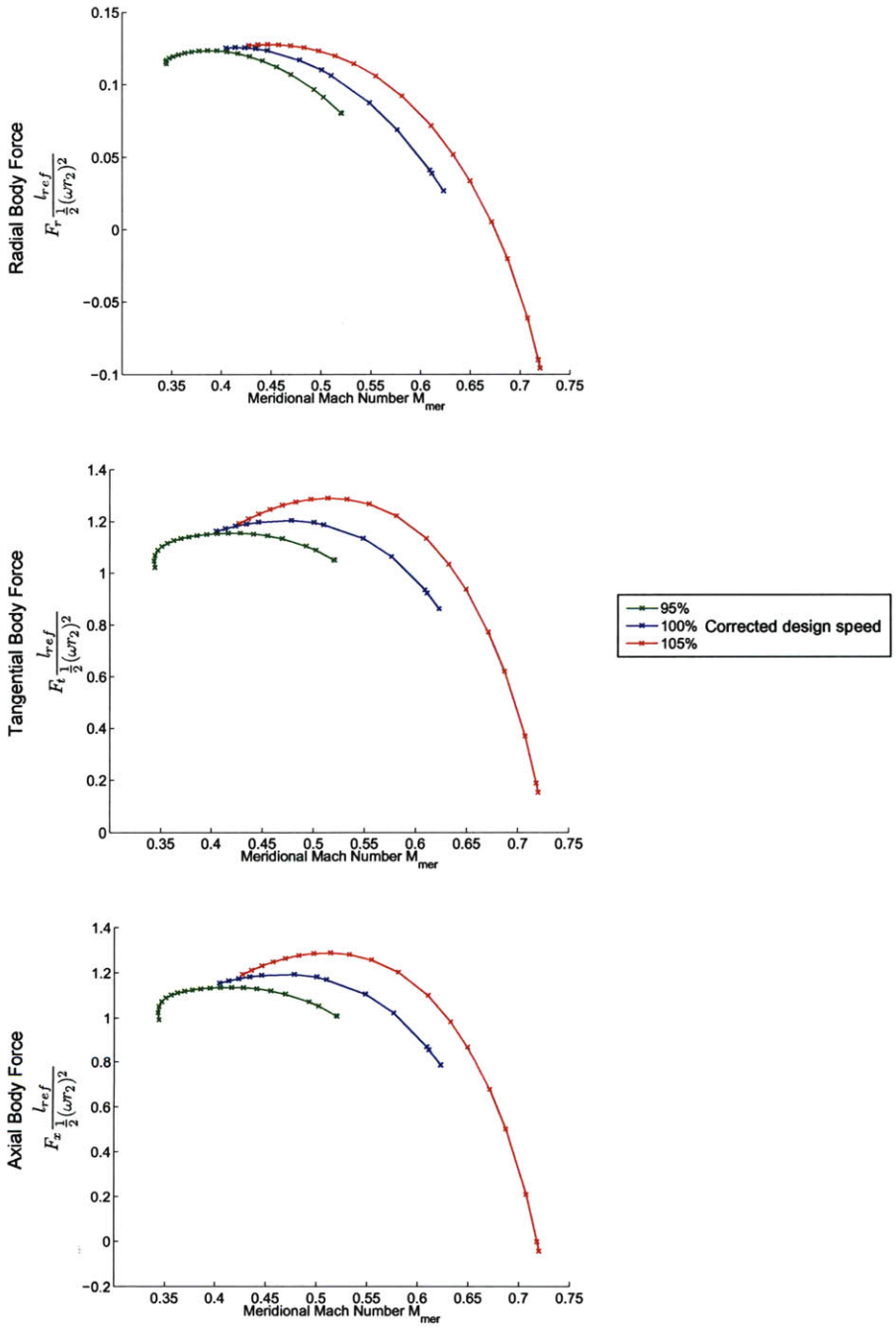


Figure 3-19: Body force components near impeller inlet as a function of local meridional Mach number

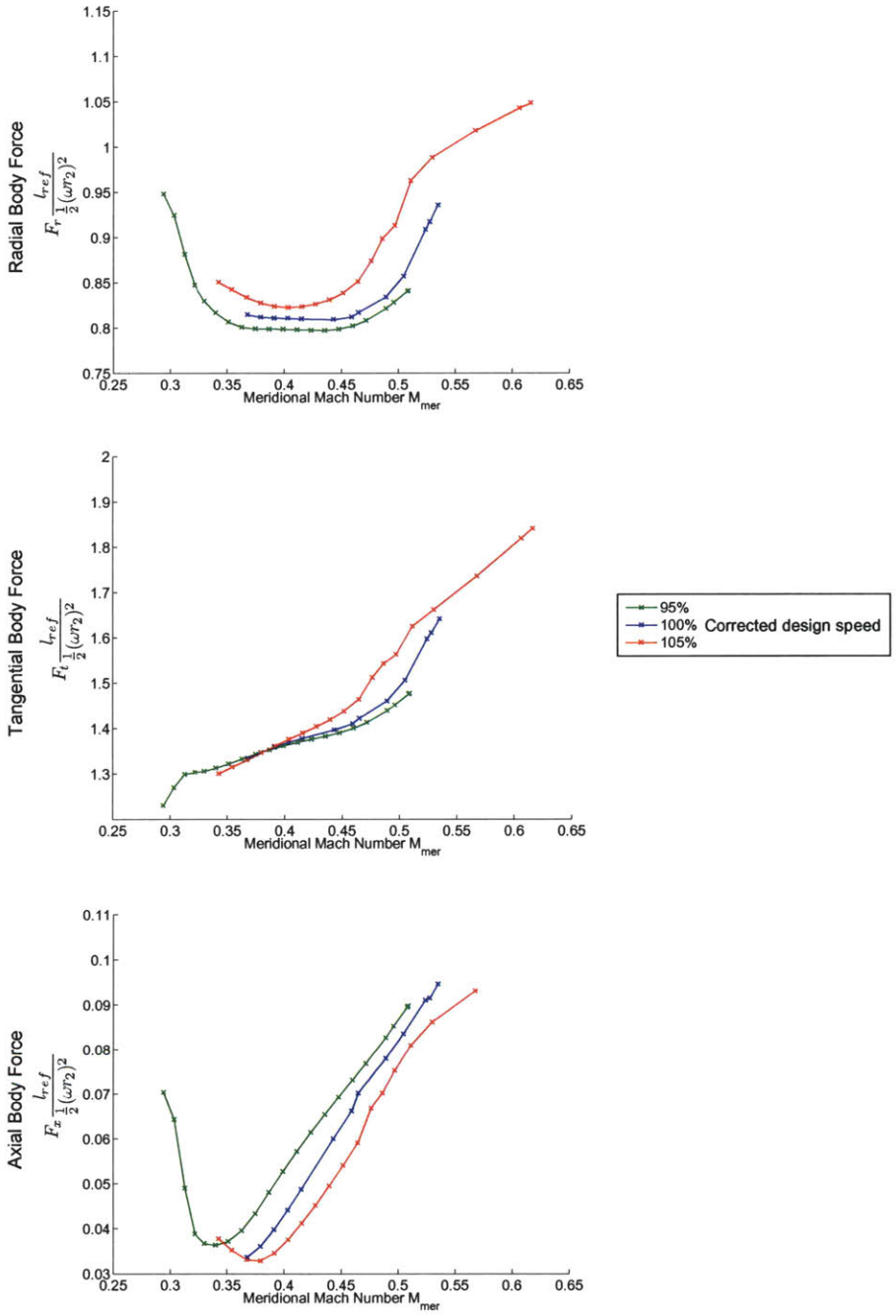


Figure 3-20: Body force components near impeller exit as a function of local meridional Mach number

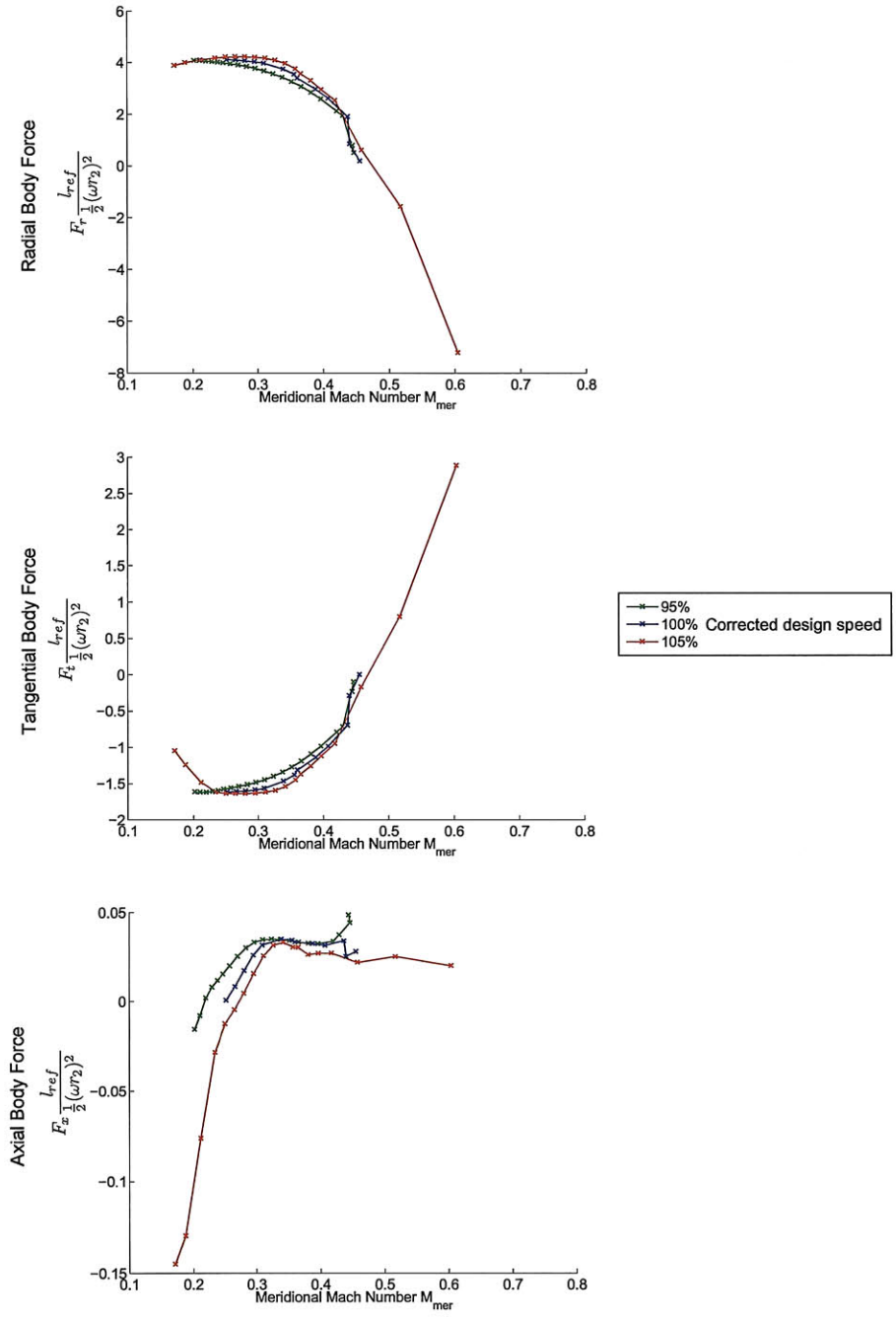


Figure 3-21: Body force components in diffuser passage as a function of local meridional Mach number

The Mach number range of the body force characteristics varies for the three speeds in the single-passage RANS simulations (see Figure 3-3). For example, the 95% design speed characteristic extends further towards the stall point, whereas more data is available near choke for the 100% design speed characteristic.

The advantage of this look-up table approach is that it covers more than 25% of the meridional Mach number range centered around the mean value. For comparison, the 2-D look-up table covered only a 1-2 degree range in swirl angle. Furthermore, a simple one-dimensional inter- and extrapolation scheme can be applied to estimate the force for a generic $M_m$.

However, in non-axisymmetric flow during stall inception, the local flow conditions can differ considerably from the flow conditions in the steady flow fields. Depending on the amplitude of the stall precursor, body force information is required for meridional Mach numbers below the values available from the look-up table.

In this first approach, the body force extrapolation is performed by keeping the last available data point in the look-up table constant for meridional Mach numbers below the tabulated values. This conservative approach prevents numerical difficulties due to excessive body forces but yet enables to capture the dynamic behavior of the disturbances during stall inception, as will be discussed in Section 6.6

### 3.4.3 Multi-valued Body Force Characteristics

The body force model requires a unique definition of the body force components, $F_r$, $F_t$, and $F_x$ at any flow condition. However, the force description, expressed in terms of $M_m$, can be multi-valued if multiple flow fields exist that have locally the same meridional Mach number.

Figure 3-22 shows an example of the body force characteristic in the diffuser passage at about 15% span from the shroud endwall. There are multiple values of force in the characteristic for the same meridional Mach number.

The reason for the occurrence of the multi-valued body forces at this location is the streamline shift near the shroud endwall due to a separation bubble near the diffuser inlet. Following the characteristic from the design point towards stall, the local

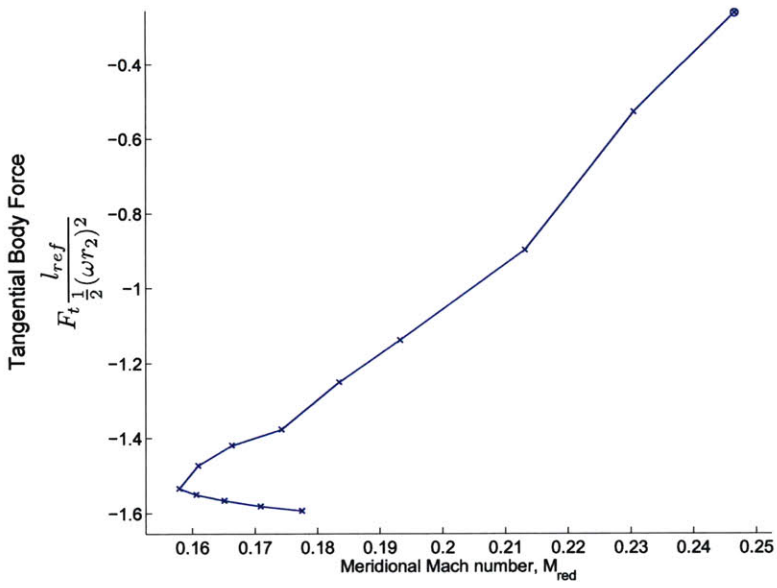


Figure 3-22: Tangential body force components near shroud downstream of diffuser leading edge as a function of local meridional Mach number.

meridional Mach number experiences an initial decrease due to a drop in overall mass flow through the compressor. At high back-pressures, a separation bubble evolves that causes a streamline shift towards the hub. Figure 3-23 illustrates the streamline shift in the 3-D RANS simulation, which can locally increase the meridional Mach number. As a consequence, the same local meridional Mach number can occur for different global operating points.

The body force characteristics were examined for each cell in the computational domain and Figure 3-24 indicates where multi-valued body forces in the look-up tables can occur. Red cells indicate that a part of the available range in meridional Mach number has multi-valued body forces. As discussed, this occurs in the diffuser near the shroud endwall. A similar phenomenon is caused by the tip leakage flow at the impeller tip near the shroud.

To obtain a unique definition of the blade force, the Mach number at the compressor inlet is introduced as an auxiliary parameter. The inlet Mach number corresponds directly to the mass flow through the compressor and decreases monotonically from the choke point to the stall point. If a multi-valued body force value is accessed, the

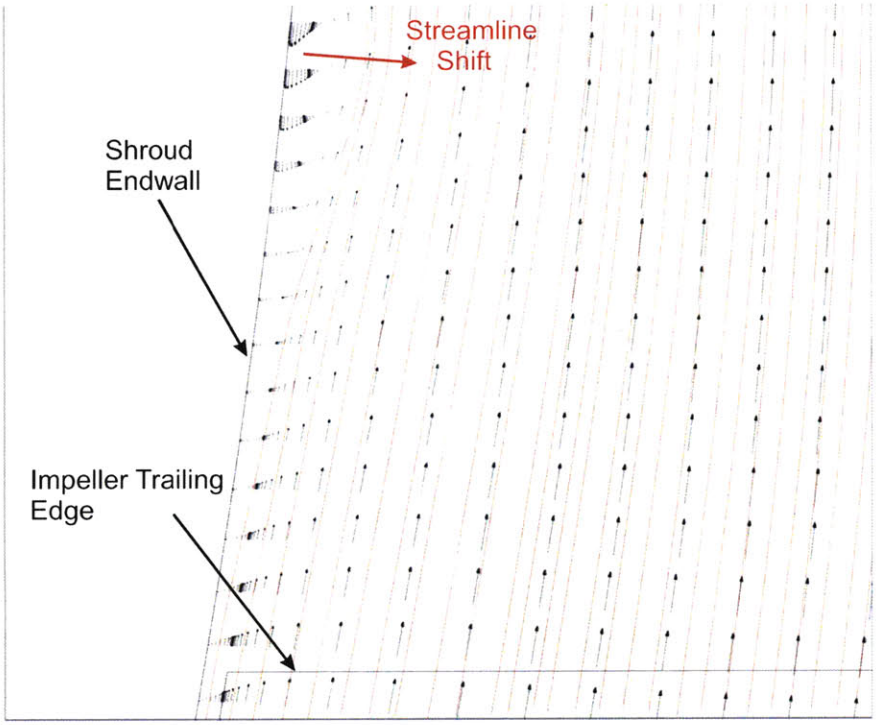


Figure 3-23: Separation bubble at shroud downstream of impeller trailing edge. The streamline shift leads to the occurrence of a multi-valued body force description.

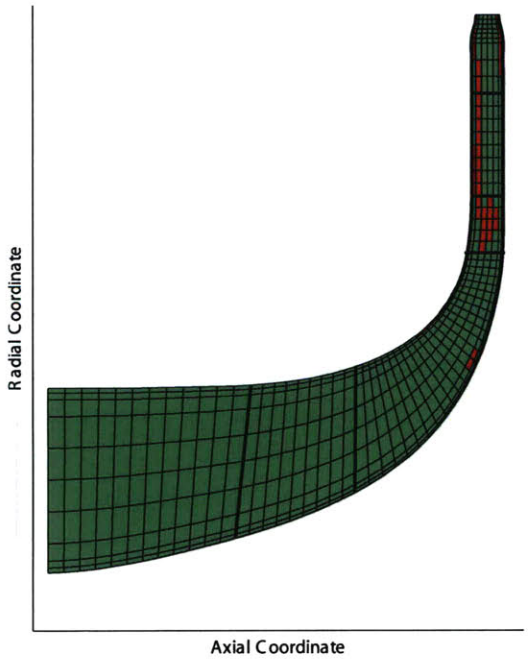


Figure 3-24: Cells containing multi-valued in body forces in the look-up table are marked in red.

body force value is selected for which the inlet Mach number is closest to the instantaneous inlet Mach number in the unsteady simulation. Hence, a unique definition of the blade force is ensured.

## 3.5 Summary

A framework was outlined for the blade force description needed for unsteady simulations with the body force model. First, the steady state compressor flow fields at different operating points were simulated for a highly-loaded centrifugal compressor with a vaned diffuser using single-passage RANS calculations.

The subcomponent pressure rise characteristics of the vaned diffuser were interrogated by comparing them with previously performed experimental measurements. Quantitatively, good agreement was found near design conditions. However, it was shown that a mismatching between impeller and diffuser is introduced due to the mixing plane approach used in the 3-D RANS simulations. The mismatching destabilizes the semi-vaneless space, indicated by a positively sloped semi-vaneless space characteristic for operating points close to stall. As the semi-vaneless space is the weakest element of the compression system, it is thus suggested that the mixing plane interface has a destabilizing effect on the compression system.

A method was introduced that extracts the blade forces for a given compressor flow field and represents them as an axisymmetric body force description. Finally, the axisymmetric body force fields for all available operating points were processed to define the local body forces as functions of the local flow parameters. The resulting force description serves as the input for the unsteady body force model described in Chapter 4.

# Chapter 4

# Development of the Body Force Based Compressor Model

As discussed in Chapter 2, the central element of the stability prediction methodology is the body force based computational model for the unsteady simulation of stall inception. The goal of this chapter is to develop a compressor model capable of simulating both types of stall inception. To capture short-wavelength disturbances, the model must be able to capture the relevant three-dimensional flow features and non-linear flow effects.

The approach is to use a body force distribution to represent the effects of the blades on the flow field, built on ideas by Marble [23] and Gong [12]. The model developed here is the first to exploit the potential of the body force model for the simulation of three-dimensional stall precursors in a centrifugal compressor with vaned diffuser. It also represents the first attempt to simulate stall inception under transonic flow conditions in a highly-loaded centrifugal compressor.

In the first section of this chapter, the modeling procedure for the compressor components is outlined. Next, the necessary modifications of the finite volume scheme in an existing Euler solver that yields the 3-D unsteady compressor model are presented. This includes the implementation of the body force source terms, the blade metal blockage, and the quasi-axisymmetric flow in the stationary and rotating blade rows.

## 4.1 Compressor Flow Field Modeling

The flow domain modeled for the body force based stall simulations is the axisymmetric three-dimensional channel between the shroud and the hub endwalls. As shown in Figure 2-1, the domain extends from upstream of the impeller leading edge to downstream of the diffuser trailing edge. The meridional plane swept around the circumference is identical to the one used in the steady, single-passage RANS simulation for the body force extraction. The flow modeling in the different compressor subcomponents is discussed in the subsections that follow. The flow modeling inside the blade passages (shaded regions in Figure 2-1) and the flow in the regions without blades are discussed separately.

### 4.1.1 Flow Modeling Outside of Bladed Regions

Neglecting viscous endwall effects and flow mixing, the flow outside the blade passages can be described by the unsteady, three-dimensional, compressible Euler equations. The conservative form of the Euler equations in cylindrical coordinates can be written as:

$$\frac{\partial}{\partial t}\begin{bmatrix} r\rho \\ r\rho V_x \\ r\rho V_\theta \\ r\rho V_r \\ r\rho e_t \end{bmatrix} + \frac{\partial}{\partial x}\begin{bmatrix} r\rho V_x \\ r\rho V_x^2 + rp \\ r\rho V_x V_\theta \\ r\rho V_x V_r \\ rV_x\left(\rho e_t + p\right) \end{bmatrix} + \frac{\partial}{\partial \theta}\begin{bmatrix} \rho V_\theta \\ \rho V_\theta V_x \\ \rho V_\theta^2 + p \\ \rho V_\theta V_r \\ V_\theta\left(\rho e_t + p\right) \end{bmatrix} + \frac{\partial}{\partial r}\begin{bmatrix} r\rho V_r \\ r\rho V_x V_r \\ r\rho V_\theta V_r \\ r\rho V_r^2 + rp \\ rV_r\left(\rho e_t + p\right) \end{bmatrix} = \begin{bmatrix} 0 \\ 0 \\ -\rho V_\theta V_r \\ \rho V_\theta^2 + p \\ 0 \end{bmatrix} \tag{4.1}$$

In previous body force formulations for axial compressors, the flow outside the bladed regions was modeled as inviscid [12]. As shown in Chapter 3, however, viscous effects outside the blade passages can lead to body forces: the highly-swirling flow at the impeller exit yields appreciable body forces that are up to 10% of force magnitude in the bladed regions. This effect may be captured by the force extraction from the high-fidelity RANS simulations. Hence, the low magnitude body force source terms outside the bladed regions are retained in the modeling procedure.

Body force source terms are therefore added to the governing equations for the flow upstream of the impeller, in the vaneless space, and downstream of the diffuser:

$$\frac{\partial}{\partial t}\begin{bmatrix} r\rho \\ r\rho V_x \\ r\rho V_\theta \\ r\rho V_r \\ r\rho e_t \end{bmatrix} + \frac{\partial}{\partial x}\begin{bmatrix} r\rho V_x \\ r\rho V_x^2 + rp \\ r\rho V_x V_\theta \\ r\rho V_x V_r \\ rV_x\left(\rho e_t + p\right) \end{bmatrix} + \frac{\partial}{\partial \theta}\begin{bmatrix} \rho V_\theta \\ \rho V_\theta V_x \\ \rho V_\theta^2 + p \\ \rho V_\theta V_r \\ V_\theta\left(\rho e_t + p\right) \end{bmatrix} + \frac{\partial}{\partial r}\begin{bmatrix} r\rho V_r \\ r\rho V_x V_r \\ r\rho V_\theta V_r \\ r\rho V_r^2 + rp \\ rV_r\left(\rho e_t + p\right) \end{bmatrix} = \begin{bmatrix} 0 \\ r\rho F_x \\ -\rho V_\theta V_r + \rho r F_\theta \\ \rho V_\theta^2 + p + r\rho F_r \\ 0 \end{bmatrix} \tag{4.2}$$

### 4.1.2 Flow Inside the Impeller and Diffuser Passages

The governing equations for the flows inside the impeller and diffuser passages are defined in Equation 4.3. A detailed derivation of these equations is omitted here (see for example Kiwada [20]); instead, the modeling concepts for the flow inside the blade

regions are discussed.

There are three conceptual modifications to the unsteady Euler equations. Each modification is highlighted by a different color.

$$\left(\frac{\partial}{\partial t}+\Omega\frac{\partial}{\partial \theta}\right)\begin{bmatrix}\lambda r\rho\\ \lambda r\rho V_x\\ \lambda r\rho V_\theta\\ \lambda r\rho V_r\\ \lambda r\rho e_t\end{bmatrix}+\frac{\partial}{\partial x}\begin{bmatrix}\lambda r\rho V_x\\ \lambda\left(r\rho V_x^2+rp\right)\\ \lambda r\rho V_x rV_\theta\\ \lambda r\rho V_x V_r\\ \lambda rV_x\left(\rho e_t+p\right)\end{bmatrix}+\frac{\partial}{\partial r}\begin{bmatrix}\lambda r\rho V_r\\ \lambda r\rho V_x V_r\\ \lambda r\rho V_\theta rV_r\\ \lambda\left(r\rho V_r^2+rp\right)\\ \lambda rV_r\left(\rho e_t+p\right)\end{bmatrix}=\begin{bmatrix}0\\ \lambda r\rho F_x+rp\dfrac{\partial\lambda}{\partial x}\\ \lambda r\rho rF_\theta\\ \lambda\rho V_\theta^2+\lambda p+\lambda r\rho F_r+rp\dfrac{\partial\lambda}{\partial r}\\ \lambda r\rho\cdot F_\theta\omega r\end{bmatrix} \tag{4.3}$$

First, the pressure rise and the flow turning caused by the impeller and diffuser blade rows are modeled by body forces distributed in the circumferential direction. The body force source terms on the right hand side are highlighted in blue. The body forces $F_r, F_\theta$ and $F_x$ are functions of the local meridional Mach number. The local work addition by the impeller is accounted for by the product of the local tangential force $F_\theta$ and the local impeller blade speed $\omega r$ on the right hand side of the energy equation.

Second, the impeller and diffuser are assumed to consist of an infinite number of thin rubber blades that restrict the redistribution of circumferential flow variations in the bladed regions [12]. Flow disturbances are locked to these infinitesimally thin, deformable channels. As a result, circumferential gradients in the flow quantities do not directly affect the flow dynamics in the bladed regions. The flows in the neighboring streamtubes are affected by a local disturbance only due to the upstream

influence and the body force effects.

This aspect of the flow is modeled by removing the $\frac{\partial}{\partial\theta}$-term from the governing equations in the blade-row relative frame. For the rotating impeller, the term $\Omega\frac{\partial}{\partial\theta}$ (see term highlighted in red in equation 4.3) arises due to the transformation from the rotating frame to the stationary frame.

Finally, blade metal blockage effects are accounted for in the modeling. The blade metal blockage $\lambda$, which was defined based on the 3-D compressor geometry in Chapter 3, is inserted into the governing equations and is highlighted in green.

## 4.2 Implementation of Body Force Based Compressor Model

This section describes how the finite volume scheme of an industry Euler solver was modified for the body force based centrifugal compressor stall model. Unlike the conservative form of the Euler equations (Equation 4.1), the governing equations of the blade passage flow (Equation 4.3) cannot directly be transformed into a finite volume description. Due to the omission of the $\frac{\partial}{\partial\theta}$-term in the governing equations (quasi-axisymmetric flow), the divergence theorem cannot be applied to obtain the required integral form based on fluxes across the control surfaces. Instead, the body force source terms, the blade metal blockage, and the modification for the quasi-axisymmetric flow in the bladed regions were implemented by modifying the evaluation of pressure and flux terms on the cell faces and altering the calculation of the fluid mass in the cell volume.

In the following subsections, the numerical scheme of the Euler solver is first introduced. Then, the implementation of each of the three modifications to the governing equations in the finite volume description is explained.

### 4.2.1 Description of the Euler Solver

The body force model is implemented by modifying an existing flow solver based on the Jameson-Schmidt-Turkel scheme [19] for solving the Euler equations in Cartesian coordinates. The code was originally developed for the simulation of the internal flow in turbines and is equipped with grid generation tools and a post-processor compatible with TecPlot. A user-interface facilitates the execution of the different tools. The body force model was implemented by modifying the source code of the Euler solver. During the course of this project, additional output routines and MATLAB tools were developed to help interpret the results from the body force simulations.

The numerical approach of the Euler solver is based on a standard finite volume scheme for spatial discretization and uses three-dimensional, structured meshes. In finite volume schemes, a system of ordinary differential equations in time is obtained by applying the integral forms of the equations of motion to each cell separately. The governing equations become:

$$\begin{aligned}
&\frac{\partial}{\partial t}\iiint_V \rho dV &&+ \iint_S \rho\vec{U}\cdot d\vec{S} &&&= 0 \\
&\frac{\partial}{\partial t}\iiint_V \rho\vec{U}\cdot dV &&+ \iint_S \left(\rho\vec{U}\cdot d\vec{S}\right)\vec{U} &&+ \iint_S p\cdot d\vec{S} &= 0 \\
&\frac{\partial}{\partial t}\iiint_V \rho\left(e+\frac{U^2}{2}\right)\cdot dV &&+ \iint_S \rho\left(e+\frac{U^2}{2}\right)\vec{U}\cdot d\vec{S} &&+ \iint_S p\cdot d\vec{S} &= 0
\end{aligned} \tag{4.4}$$

A multi-stage Runge-Kutta time-stepping scheme solves the system of ordinary differential equations for all cells in the computational domain. As the time-stepping scheme was not altered by the body force implementation, a discussion on time-stepping is omitted here.

### 4.2.2 3-D Euler Grid for Body Force Based Stall Simulations

All simulations that will be discussed in Chapters 5 and 6 were performed on the 3-D Euler Grid shown in Figure 4-2. With the body force approach, there is no longer a

need for complicated grid topologies capturing the geometry of the discretized blades. Instead, a structured, axisymmetric grid for the entire computational domain is set up.

This axisymmetric grid was generated by sweeping the meridional Euler mesh (see figure 4-1) around the axis of rotation. The descriptions of the hub and shroud lines in the meridional plane for the 3-D Euler Grid are based on the RANS flow domain. This ensured compatibility between the flow domains, which was important for the body force extraction near the endwalls.

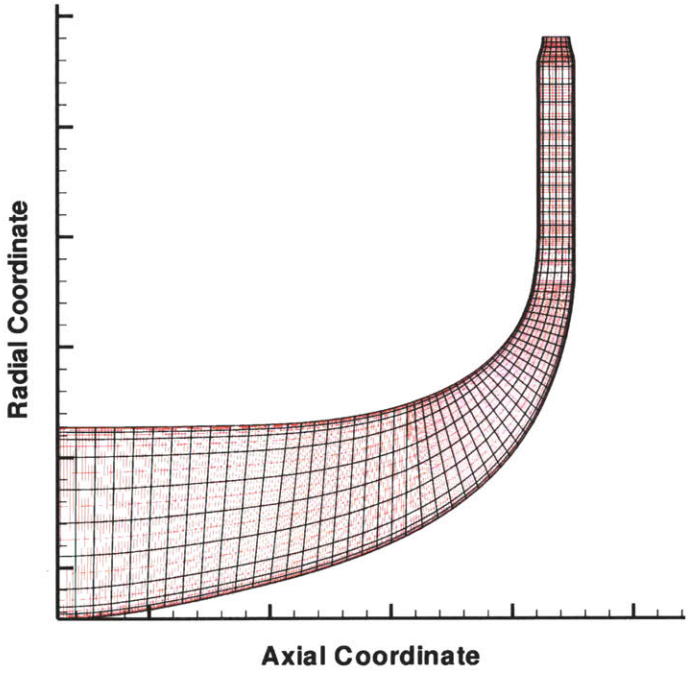


Figure 4-1: Meridional plane of the 3-D Euler Grid for the body force model (bold lines in black) overlaid with the intermediate mesh (red lines).

The 3-D Euler Grid used has 68 cells in the streamwise direction, 10 cells in the spanwise direction and 100 cells around the circumference. A total cell count of 68,000 for the full wheel domain is used. This grid is much smaller compared to 12 million cells that would be needed for an unsteady, full-wheel RANS simulation. As a result, unsteady flow simulations of the entire compressor over several rotor revolutions can be performed orders of magnitudes faster than in 3-D unsteady RANS simulations.

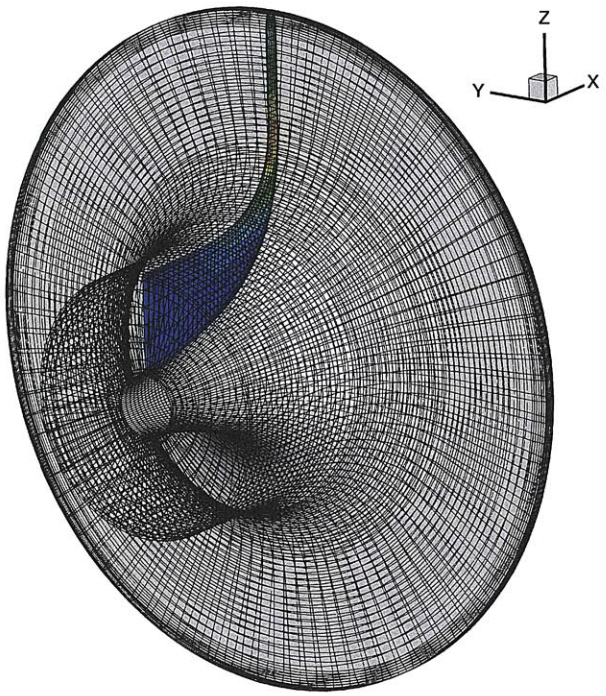


Figure 4-2: 3-D Euler Grid used in body force model. The grid consists of a single structured, axisymmetric block of 68,000 cells.

### 4.2.3 Body Force Source Term Implementation

To capture the flow turning and pressure rise of the compressor, the integral forms of the Euler equations are modified by a source term on the right hand side:

$$\begin{aligned}
&\frac{\partial}{\partial t}\iiint_{V_\lambda} \rho dV && + \iint_{S_\lambda} \rho\vec{U}\cdot d\vec{S} && && = 0 \\
&\frac{\partial}{\partial t}\iiint_{V_\lambda} \rho\vec{U}\cdot dV && + \iint_{S_\lambda} \left(\rho\vec{U}\cdot d\vec{S}\right)\vec{U} && + \iint_{S_\lambda} p\cdot d\vec{S} && = \iiint_{V_\lambda} \rho\cdot\vec{F}\, dV \\
&\frac{\partial}{\partial t}\iiint_{V_\lambda} \rho\left(e+\frac{U^2}{2}\right)\cdot dV && + \iint_{S_\lambda} \rho\left(e+\frac{U^2}{2}\right)\vec{U}\cdot d\vec{S} && + \iint_{S_\lambda} p\cdot d\vec{S} && = \iiint_{V_\lambda} \rho\left(F_\theta\cdot\Omega r\right) dV
\end{aligned} \tag{4.5}$$

.

In Chapter 3, the body force was defined as a force per unit mass. Consistently, the force components are multiplied here by the fluid mass in the cell volume $\iiint_V \rho\, dV$.

In the unsteady simulations, the force components are functions of the local meridional Mach number. Therefore, the instantaneous meridional Mach number in each

cell is calculated before applying the integral form of the governing equations to the computational cells. Then, the look-up table for the radial and axial location of the cell is accessed and the three force components are interpolated according to the description in Section 3.4.2. If a multi-valued body force in the look-up table is determined (see Section 3.4.3), the algorithm uses the inlet Mach number as an auxiliary parameter. A unique description is ensured since the inlet Mach number is a global parameter and drops monotonically from choke to stall.

### 4.2.4 Blade Metal Blockage

In the Jameson scheme, the flow quantities on each of the six faces of a computational cell are evaluated as the average of the values at the cell centers on the two sides of the face. The mass, momentum, and energy flows across each face are then calculated assuming that the flux quantities ($\rho v_\perp$, $\rho v_\perp v_x$, $\rho v_\perp v_y$, $\rho v_\perp v_z$, $\rho v_\perp h$) are uniform on the face. In other words, the flows across the faces are simply calculated as the product of the face area and flux quantities. Similarly, the mass in the cell is calculated assuming that the density in the cell is uniform and equal to the cell-centered value. In such a model, the reduction in through-flow area due to blade metal blockage can be represented by reducing the effective cell surface areas and the effective cell volume.

Section 3.3.3 defined the blade metal blockage term, $\lambda$, at any axial and radial location in the gas path. The averaged blade metal blockage in each cell volume and on each cell face was determined from the 3-D blade geometry of the test compressor. Based on this information, the volume and surface terms in the integral form of the governing equations are modified. In Equation 4.5, this is expressed by replacing the initial cell volume $V$ by the effective cell volume $V_\lambda = \lambda_{cell} V$. Equivalently, the effective area of each cell face is reduced to $S_{\lambda,i} = \lambda_{face,i}\, S$. The overall cell surface, $S_\lambda$, is then the sum over all the cell faces.

### 4.2.5 Implementation of Quasi-Axisymmetric Flow in Stationary Blade Row

This section outlines the implementation of the governing equations for the quasi-axisymmetric flow description inside the vaned diffuser, i.e. for blade rows in the stationary frame. The model implementation will be extended in Section 4.2.6 to capture the effects of the flow field in the rotating impeller.

As discussed in Section 4.1.2, the $\frac{\partial}{\partial\theta}$-term in the differential form of the governing equations for the flow inside the blade rows needs to be removed. In the Euler solver implementation, the gradient in the circumferential direction cannot be removed directly from the integral form of the Euler equations. However, the structured, axisymmetric grid topology in the 3-D Euler Grid (see figure 4-2) allows an effective implementation of the quasi-axisymmetric flow model. To obtain a finite volume description that omits the influence of the tangential gradients inside the bladed regions, the flux term evaluation on the radial cell faces is modified.

Figure 4-3 shows three cells in a plane perpendicular to the axis of rotation. Index $j$ labels the circumferential location of a generic cell inside the flow domain, while the cells $j-1$ and $j+1$ are the neighboring cells in the circumferential direction.

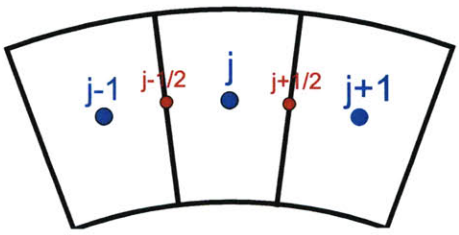


Figure 4-3: Conceptual illustration of a generic cell with the labels for its radial faces and its neighboring cells.

The original Jameson scheme represents the flow quantities at all cell faces by averaging the adjacent cell center values. For example:

$$\begin{aligned} \rho\left(j-\frac{1}{2}\right) &= \frac{\rho(j)+\rho(j-1)}{2} \\ \rho\left(j+\frac{1}{2}\right) &= \frac{\rho(j)+\rho(j+1)}{2} \end{aligned} \tag{4.6}$$

Since the flow quantities at locations $j - \frac{1}{2}$ and $j + \frac{1}{2}$ can be different due to circumferential flow variations, the Jameson scheme does account for circumferential gradients $\frac{\partial}{\partial\theta}$.

In the implementation for the quasi-axisymmetric flow in the bladed regions, this influence was removed. For the analysis of cell $j$, a quasi-axisymmetric flow field was assumed by setting the value of the flow quantities at the faces $j - \frac{1}{2}$ and $j + \frac{1}{2}$ equal to the cell-centered value:

$$\begin{aligned} \rho\left(j - \frac{1}{2}\right) &= \frac{\rho(j) + \rho(j)}{2} = \rho(j) \\ \rho\left(j + \frac{1}{2}\right) &= \frac{\rho(j) + \rho(j)}{2} = \rho(j) \end{aligned} \tag{4.7}$$

.

Thus, the flow quantities in neighboring cells ($j - 1$ and $j + 1$) are assumed to be identical to those in cell $j$, i.e. the local flow field is assumed to be axisymmetric. As the solver is based on Cartesian coordinates, the velocity vector from the cell center needs to be rotated to obtain the velocity vector at the radial cell faces. The fluxes on the two axial and circumferential faces are calculated using the Jameson scheme.

### 4.2.6 Implementation of Quasi-Axisymmetric Flow in the Rotating Impeller Frame

The quasi-axisymmetric flow model discussed in Section 4.1.2 restricts the redistribution of disturbances in the bladed regions. Flow disturbance are locked to infinitesimally thin deformable channels [1]. For a stationary blade row, this aspect of the flow was implemented as described in Section 4.2.5.

However, the disturbances in the rotating impeller are locked to the blade passages in the rotating impeller frame. Viewed by a stationary observer, the impeller relative flow field, including the circumferential variations and disturbances in the passages, rotates around the circumference at impeller speed. Figure 4-4 schematically illus-

[1]The flow in the neighboring streamtubes is affected by a local disturbance only due to the upstream influence and body force effects.

trates a disturbance (red) that is locked to the impeller blade passages.

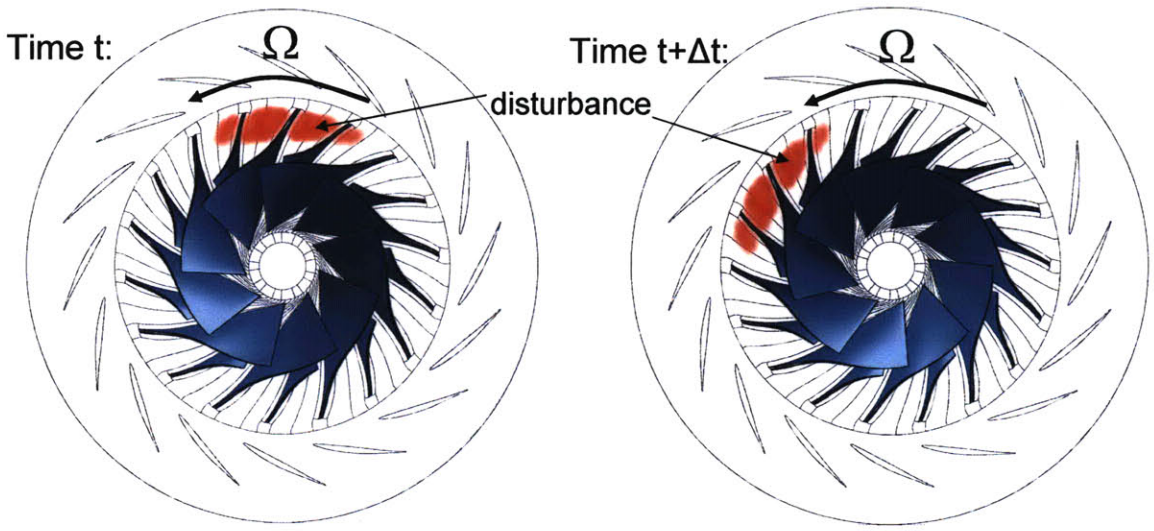


Figure 4-4: Flow disturbance (red) inside the impeller passages at two consecutive time instances. The disturbance is locked to the blade passage in the rotating impeller frame. Viewed from stationary frame, the disturbance rotates around the circumference at impeller speed.

The body force model computes the flow field in the absolute frame. To capture the behavior of disturbances locked to the impeller frame, the influence of the circumferential gradients $\frac{\partial}{\partial\theta}$ is removed as seen in Section 4.2.5, but the relative flow field is rotated additionally at each time step.

The rotation effect of disturbances in the impeller relative flow field was implemented in the Euler solver by rotating the unsteady flow field in the absolute frame at rotor frequency, as illustrated in Figure 4-5. At each time step, the rotating angle $\Delta\Theta$ is determined based on the time step and the impeller angular velocity. The black dot represents a generic cell center at angle $\theta$. To achieve the effect of rotation, the value at the angle $\theta + \Delta\Theta$ (red dot) is interpolated and is assigned to the cell center (black dot).

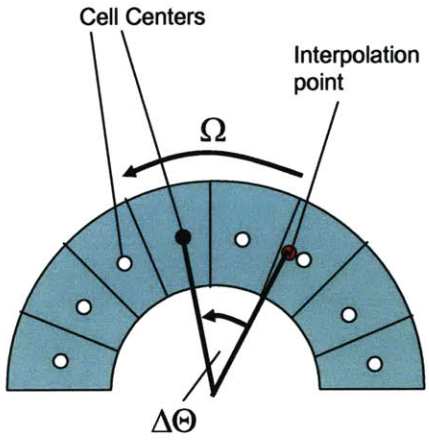


Figure 4-5: Illustration of numerical implementation of rotation effect for disturbances in impeller frame.

# Chapter 5

# Quasi-Steady Compressor Performance Computation

The key objective of the new methodology is to capture the dynamic behavior and the stall inception of highly-loaded centrifugal compressors. To assess the fidelity of the body force simulations, simulations of the steady, axisymmetric compressor flow field are first performed. At reduced speed (approximately 75% design speed), the body force based flow field simulations demonstrate good quantitative agreement with the high-fidelity, steady RANS simulations. This chapter provides a detailed comparison of the global compressor performance and the flow field details. At high impeller speeds, the sensitivity of the transonic flow to numerical inaccuracies caused by the grid resolution was found to be responsible for convergence problems. Based on these findings, the decision was made to first demonstrate the stall inception simulation at reduced speed.

## 5.1 Quasi-Steady Compressor Simulations

A sequence of quasi-steady body force simulations was performed for a number of operating points along a speedline at 75% corrected design speed. In these quasi-steady simulations, the local body force components were functions of the local meridional Mach number as described in Section 3.4.2.

The look-up table data was obtained by consistently scaling down the body forces extracted from the FineTurbo simulations at 78% design speed (see section 3.3). The body force based simulations were performed at 75% rather than directly at 78%, because it considerably improved the numerical convergence of the calculations. To validate all key elements of the methodology, including the body force extraction, the look-up table approach, and the body force model, and to assess the fidelity of the body force simulations, the axisymmetric compressor flow fields are compared to the pitchwise-averaged flow field from the single-passage RANS simulations.

First, the stage pressure ratio characteristic and the diffuser subcomponent pressure rise characteristics are assessed. Next, a detailed comparison between the flow field from the body force model and the pitchwise-averaged RANS solution is given. Finally, some numerical difficulties encountered when solving for the flow field at higher compressor speeds are analyzed and discussed.

## 5.2 Assessment of Global Compressor Performance

Figure 5-1 depicts the collection of stage pressure rise characteristics available from experiments and simulations. Experimental measurements available at 100% design speed are indicated by the green circles. The blue crosses correspond to the four speedlines obtained from the steady, single-passage RANS simulation. These simulations were discussed in detail in Section 3.1. The quasi-steady body force simulations were performed at 75% design speed. The speedline was computed by gradually increasing the static pressure at the diffuser exit. Operating points in the stable operating range are marked by red crosses. Two additional red circles (#2 and #3) indicate operating points at high back-pressures where the steady simulations resulted in converged solutions, but the unsteady simulations (discussed in Chapter 6) revealed them to be unstable.

For the stable operating range, the body force simulations are in good agreement with the high-fidelity RANS simulations. The quantitative difference in the stage pressure ratio is less than 5% throughout the operating range. At the left end of

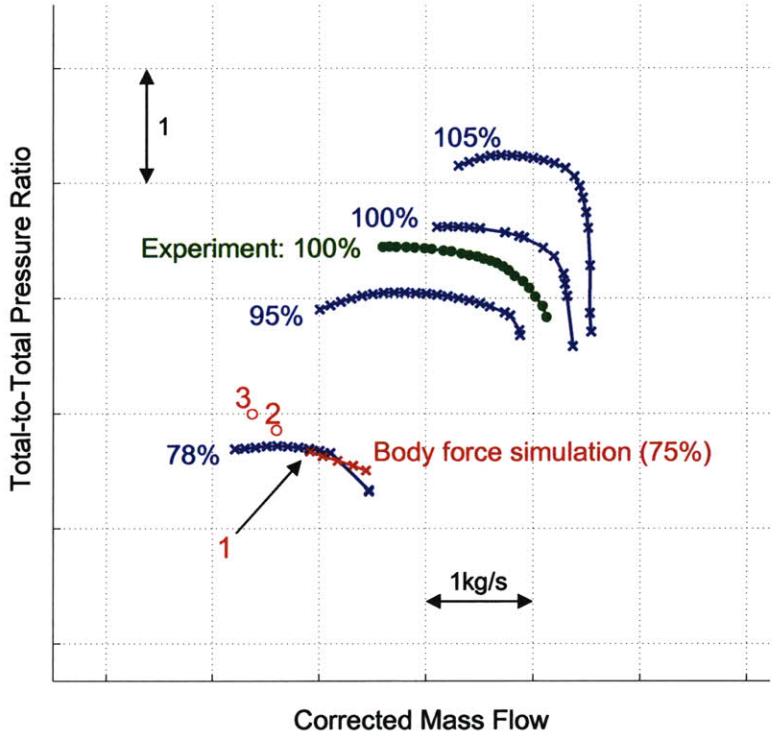


Figure 5-1: Total pressure ratio characteristics of the test compressor. Comparison between the body force simulations, RANS simulations, and experimental results.

the stable operating range (near point #1), the body force look-up table contains more information, as more FineTurbo flow solutions were available in the flat part of the characteristic. As a result, the fidelity of the body force model is improved near point #1 and the discrepancy in the stage pressure ratio is reduced to a fraction of a percent.

To evaluate the fidelity of the body force model, it is useful to compare the quantitative error introduced by the 3-D RANS simulation to the quantitative error introduced by the body force approach. In Section 3.2, errors of up to 8% were seen in the stage pressure ratio that were introduced due to the mixing plane approach and the absence of a volute downstream of the diffuser in the simulation. For the stable operating range, the results suggest that the assumptions in the body force description introduce errors that are of the same order of magnitude as those resulting from the single-passage RANS simulations described in Section 3.2.

In the stable operating range, the slope of the characteristic is captured and is in agreement with the FineTurbo results. However, Figure 5-1 also indicates that the steady body force simulations do not follow the slope of the RANS characteristic when the back-pressure is further increased. While the mass flow decreases adequately, the stage pressure rise is overestimated in the steady body force simulations. The results suggest that, as the mass flow is further reduced, the body force model starts to access entries in the body force look-up table where the forces are extrapolated. The influence of the extrapolated forces on the steady performance are discussed together in Section 5.5.

## 5.3 Assessment of Diffuser Static Pressure Rise Characteristic

The work by Spakovszky and Roduner [29] identified the static pressure rise characteristics of the vaned diffuser and its subcomponents as useful metrics for the stability analysis in centrifugal compressors with vaned diffusers.

To determine the diffuser subcomponent characteristics in the RANS simulations in Section 3.2.2, the wall static pressure was determined at several streamwise and pitchwise locations in the diffuser passage. In the body force model, the diffuser blade row is modeled as quasi-axisymmetric flow, thus discrete passages no longer exist. This prevents a consistent comparison of the subcomponent characteristics of the body force model to those of FineTurbo. Thus, the discussion is focused on the characteristic of the overall diffuser. For the comparison of the characteristics, the diffuser encloses the vaneless space, the semi-vaneless space, the diffuser passage and the vaneless region downstream of the diffuser blading.

Figure 5-2 compares the different characteristics calculated by FineTurbo and the body force model. The results from the RANS simulation with FineTurbo are marked by the blue crosses, while the red crosses correspond to the body force results. Near choke-side of the characteristic, the body force simulation results do not match the FineTurbo results, since the body force look-up table is not populated with data at high flow conditions. However, considerably more data points are available in the look-up table for operating points between near design point and stall point. For the investigation of stall inception, this part of the characteristic is important and in good agreement with the RANS results. The maximum relative difference in the pressure coefficients is approximately 3%. More importantly, the body force simulation agrees with FineTurbo in that the characteristic flattens out towards the left side of the characteristic.

In terms of corrected flow at the diffuser inlet, the body force model is capable of obtaining flow solutions at lower flows than FineTurbo. At low flow, the results indicate that the diffuser static pressure rise characteristic peaks and changes the slope to slightly positive at operating point #3. The positive slope of the characteristic indicates that the diffuser flow is destabilized and modal stall precursors might form at this operating point.

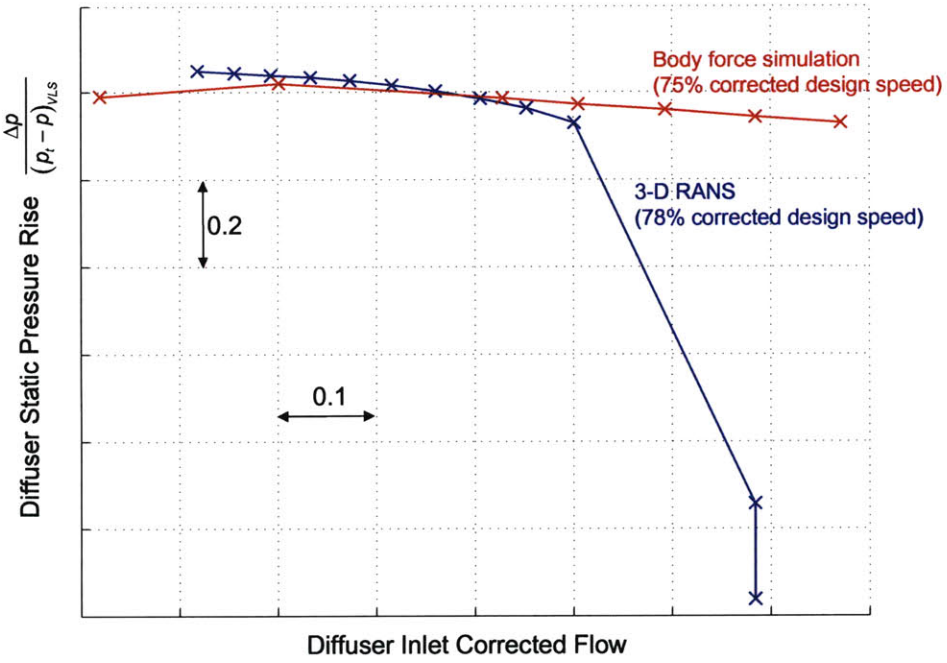


Figure 5-2: Diffuser static pressure rise characteristic at 75% corrected design speed.

## 5.4 Compressor Flow Field Assessment

Since the objective of the body force model is to investigate the stall inception, the fidelity of the simulation for flow conditions close to stall is of particular interest. The steady flow field is assessed for the last operating point at the left side of the stable characteristic. The assessment is conducted by comparing the axisymmetric flow field from the body force simulation in the meridional plane to the pitchwise-averaged FineTurbo solution.

Figure 5-3 shows the meridional plane of the 3-D RANS simulation (left) and the body force model (right). For comparison, the flow domains of the two simulations are identical. In Figure 5-3, the static pressure field is illustrated as a contour plot. Although absolute values are not shown, all contour plots have consistent color scales when comparing results from the body force model to the FineTurbo flow solutions.

The following two subsections analyze the streamwise flow behavior at channel mid-span (along the dashed line in Figure 5-3) and in the spanwise direction. The

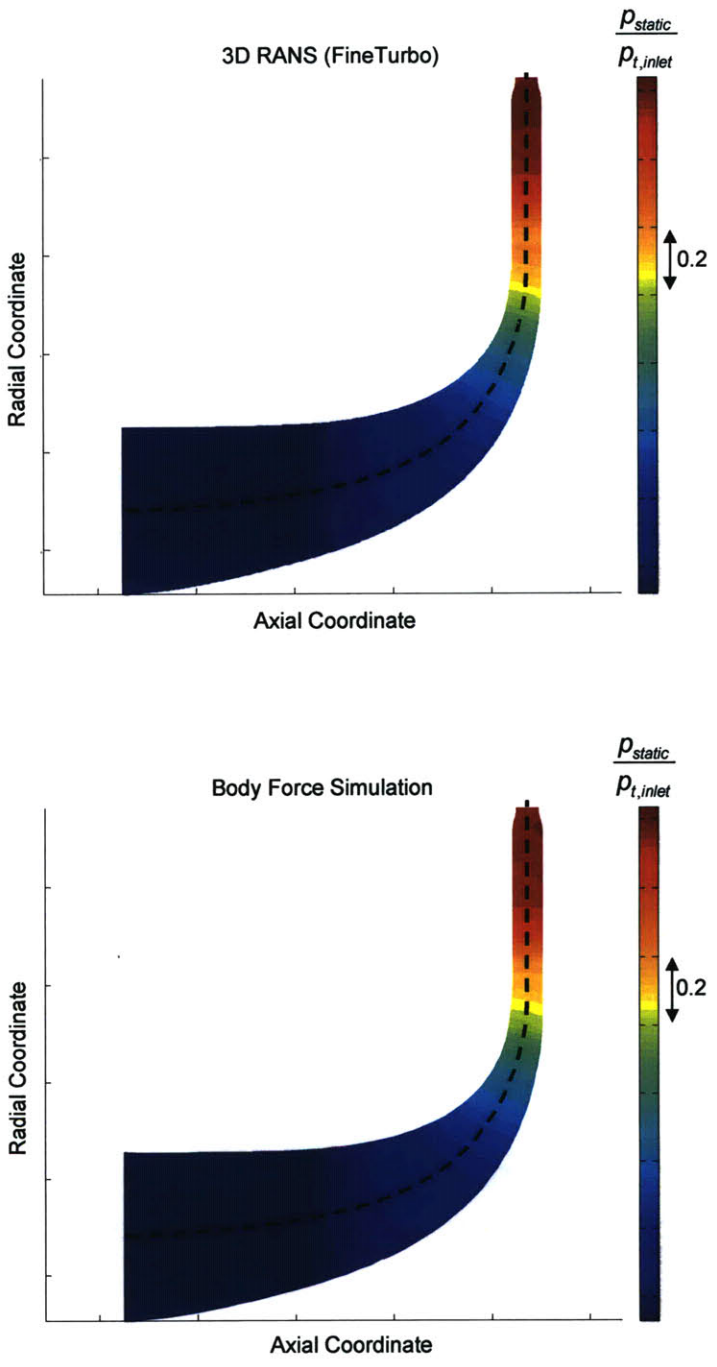


Figure 5-3: Static pressure contour in the meridional plane. Top: pitchwise-averaged static pressure from 3D-RANS simulation. Bottom: static pressure in the axisymmetric flow field simulated by the body force model.

assessment includes the stagnation and static values of pressure and temperature, the Mach number components, and the swirl angle. It shows that the body force model achieves good qualitative and quantitative agreement with 3-D RANS simulations on the channel centerline, while the spanwise variation is not fully captured at the impeller exit and in the diffuser.

### 5.4.1 Streamwise Flow Behavior at Channel Mid-Span

Figures 5-4 to 5-12 illustrate the flow variation of several flow quantities at midspan along the centerline between the hub and shroud. The left ends of the graphs correspond to the inlet of the compressor domain, while the right ends correspond to the radial outlet of the domain. For clarity, the positions of the leading and trailing edges of the impeller main blade, the splitter blade, and the diffuser blade are indicated by the grey vertical lines.

In each figure, the blue curve corresponds to the data from the body force simulation, while the red curve illustrates the 3-D RANS flow solution. Each blue cross represents a grid cell in the body force simulation. The resolution of the FineTurbo mesh is many times higher; therefore, the data are represented by a continuous, solid line.

Figures 5-4 and 5-5 depict the stagnation pressure and stagnation temperature along the channel. The variation in stagnation quantities along the channel illustrates the pressure rise and the work addition through the impeller and the losses in the diffuser. On a component level, both the pressure rise and the work addition across the impeller as determined by the body force model agree with the RANS results within 1%. At the impeller leading edge, the work addition by the inducer becomes significant and results in a sharp increase in $p_t$ and $T_t$. The body force simulation agrees well with the results from the RANS calculation in the inducer. Through the impeller passage, the numerical errors increased slightly. The maximum error is 1.8% in stagnation temperature and approximately 3% in stagnation pressure.

No work is added downstream of the impeller trailing edge. As a result, the stagnation temperature is constant through the diffuser as illustrated in both calculations.

The body force model also captures the loss mechanisms in the diffuser. Mixing losses and boundary layer losses yield a decrease in the stagnation pressure across the vaneless space and the diffuser passage. In the vaneless space and in the upstream half of the passage, the body force based simulation agrees well with the RANS simulation. Towards the trailing edge of the diffuser blades, however, the body force model slightly overestimates the magnitude of the loss. The difference can be attributed to the discrepancies in the spanwise variation of the stagnation pressure, which leads to a shroud endwall separation in the body force simulation. The spanwise variation in the flow properties is discussed in the following subsection.

Figures 5-6 and 5-7 depict the variation in the static pressure and static temperature. Similar to the stagnation quantities, good quantitative agreement is achieved between the body force based simulations and RANS simulation. Small numerical errors of up to 1-2% arise in the impeller passage. The pressure recovery in the vaneless space and the diffuser passage are captured correctly. A difference of about 2% in the pressure recovery is estimated downstream of the diffuser blading. This difference can be attributed to overestimated losses due to the shroud endwall separation.

Figures 5-8 to 5-11 show the absolute, radial, tangential, and axial Mach number through the compressor. The variation in swirl angle along the channel is plotted in Figure 5-12. At the leading edge, the axial Mach number component experiences a sharp increase due to the reduction in flow-through area caused by the blade metal blockage. The body force based simulation captures this effect and agrees with the RANS simulation within less than 1% of error. At the same location, the flow is turned by the inducer, and the tangential Mach number and the swirl angle are increased. The 3-D RANS simulation and the body force based simulation show a nearly identical rise in the flow Mach number and flow angle. Towards the trailing edge of the impeller, the body force model overestimates the flow Mach number. The maximum error is approximately 7%, which is relatively high in comparison to the good agreement in the previously discussed quantities. The reason for the relatively high numerical error is the high sensitivity of the transonic flow to small numerical inaccuracies in the stagnation quantities. Section 5.6 discusses this aspect of transonic

flow in more detail. At the trailing edge of the impeller, the blade metal blockage drops sharply to zero in the vaneless space. As the though-flow area is increased, the radial Mach number is reduced per conservation of mass. The decrease in the radial Mach number is in agreement between the two simulations.

In summary, the comparison shows that the body force model captures all aspects of the flow variation at midspan along the compressor channel. With only 68,000 cells (compared to 12 million for a full-wheel RANS simulation), the body force based simulations agree with the high-fidelity RANS simulations, with errors less than 3% in stagnation and static states. The largest error in Mach number is 7% due to the high sensitivity of the transonic flow to small inaccuracies in the stagnation quantities.

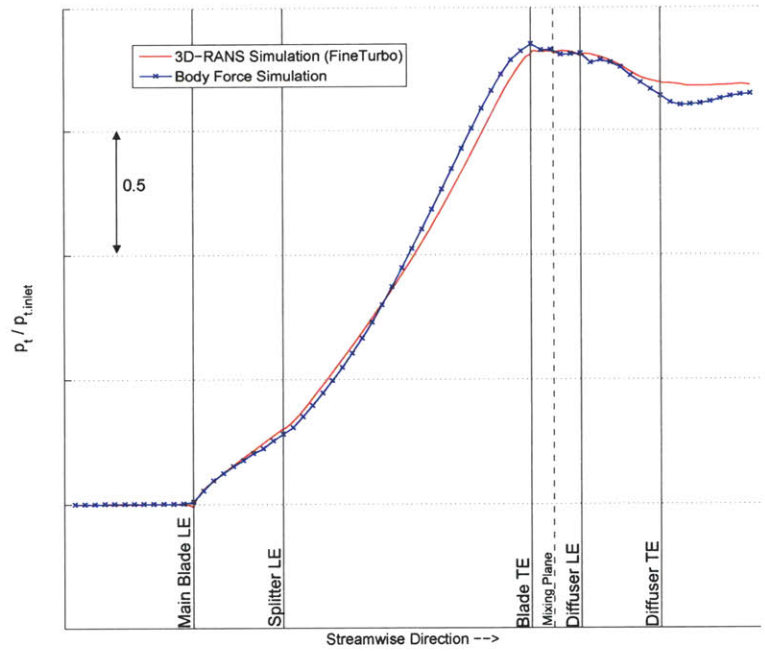


Figure 5-4: Stagnation Pressure. Comparison of the results from the body force simulation to those from the RANS simulation.

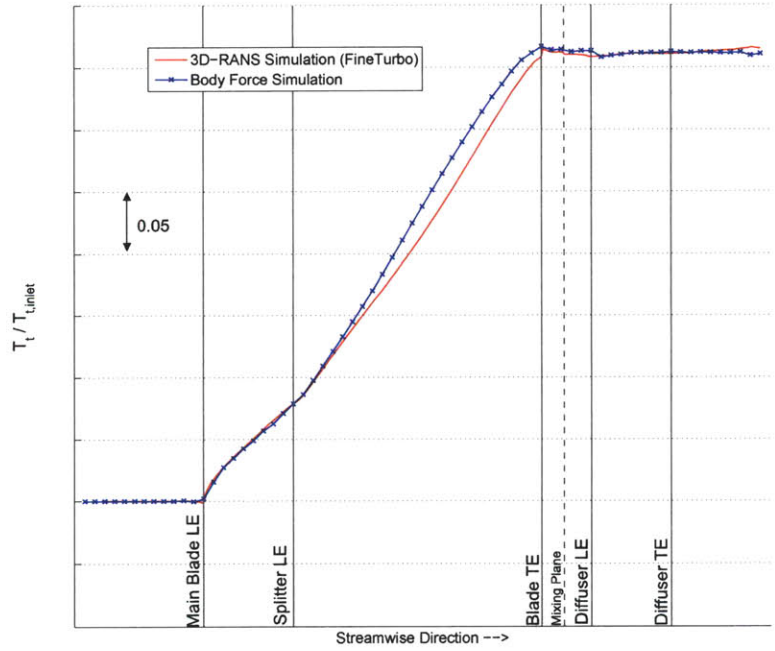


Figure 5-5: Stagnation Temperature. Comparison of the results from the body force simulation to those from the RANS simulation.

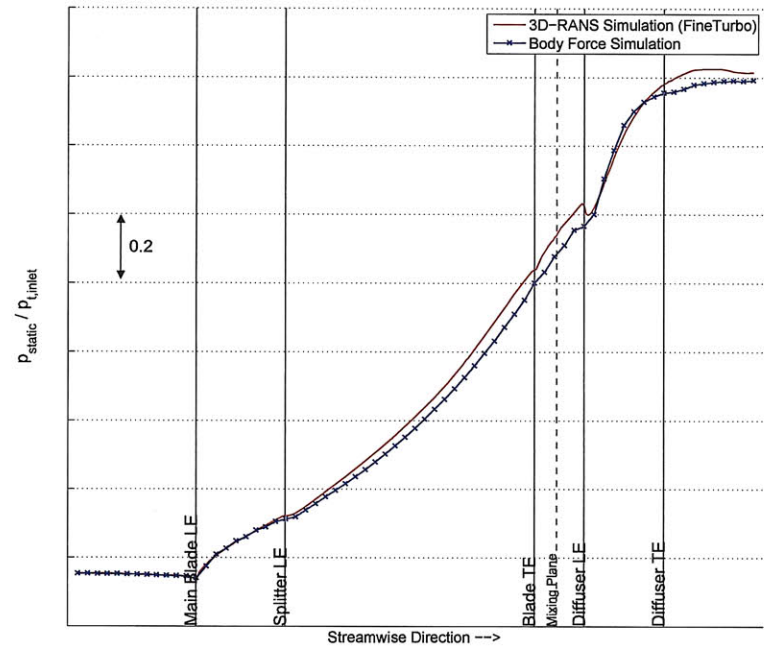


Figure 5-6: Static Pressure. Comparison of the results from the body force simulation to those from the RANS simulation.

Figure 5-7: Static Temperature. Comparison of the results from the body force simulation to those from the RANS simulation.

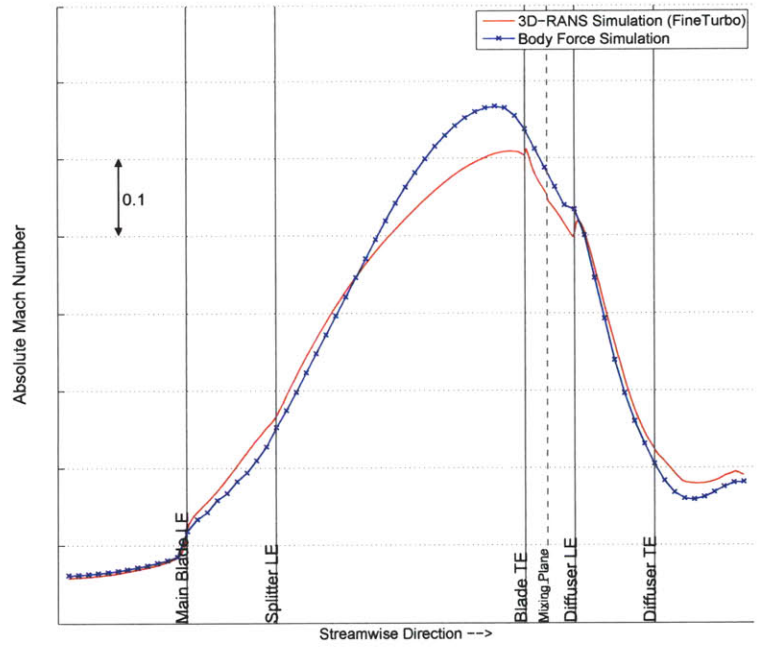


Figure 5-8: Absolute Mach Number. Comparison of the results from the body force simulation to those from the RANS simulation.

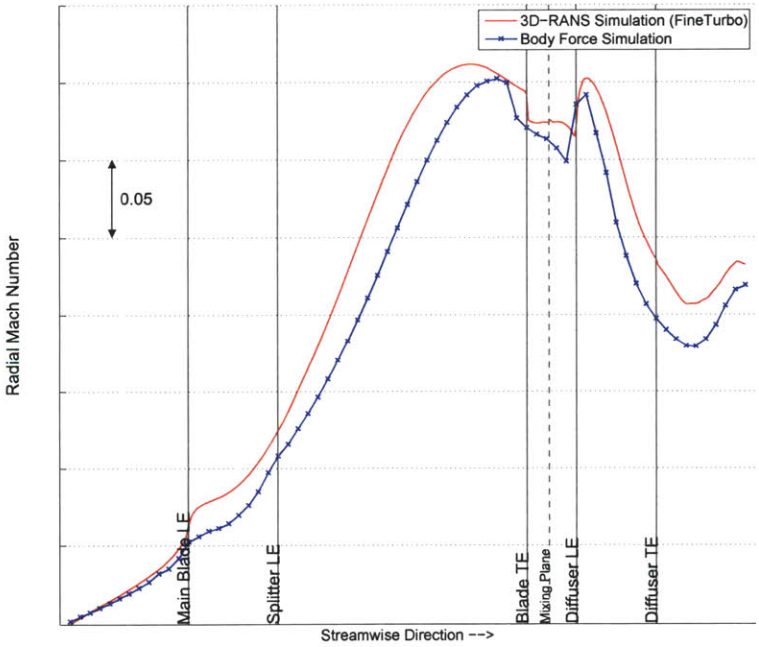


Figure 5-9: Radial Mach Number. Comparison of the results from the body force simulation to those from the RANS simulation.

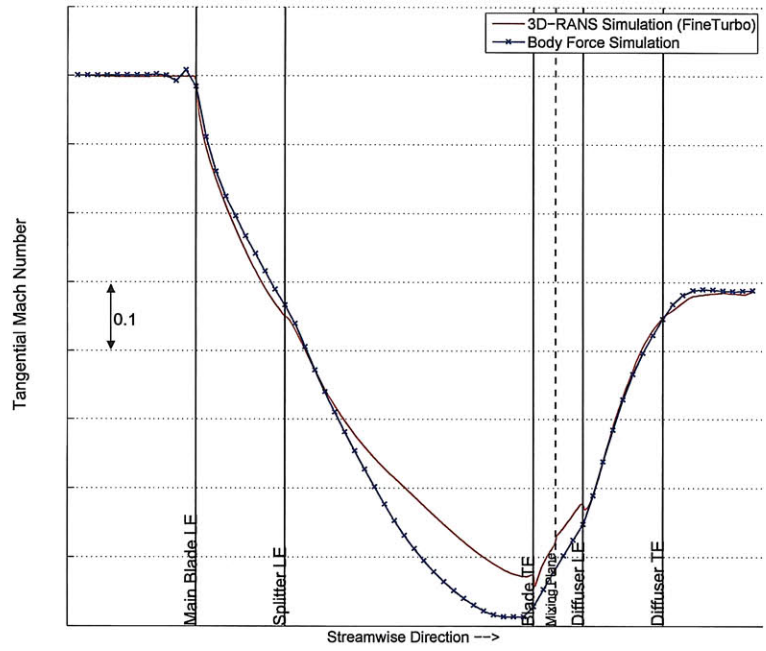


Figure 5-10: Tangential Mach Number. Comparison of the results from the body force simulation to those from the RANS simulation.

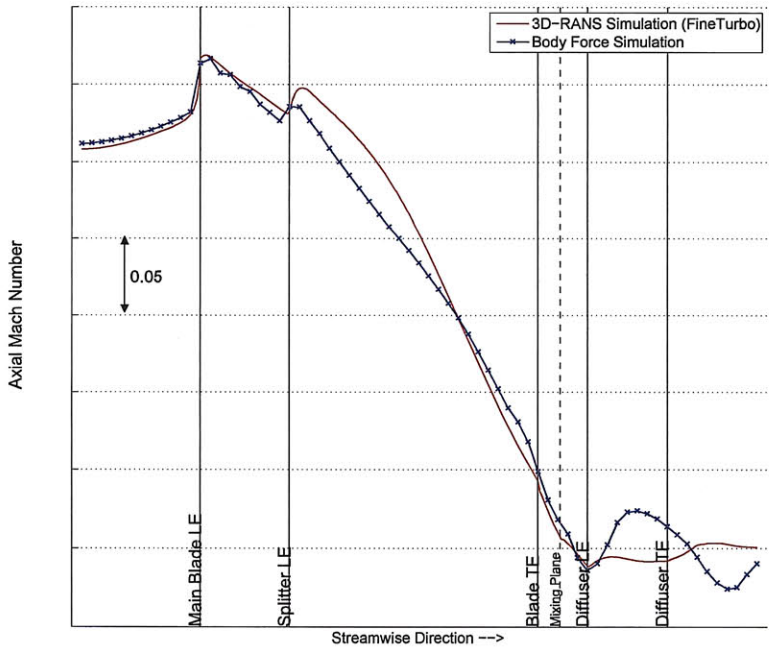


Figure 5-11: Axial Mach Number. Comparison of the results from the body force simulation to those from the RANS simulation.

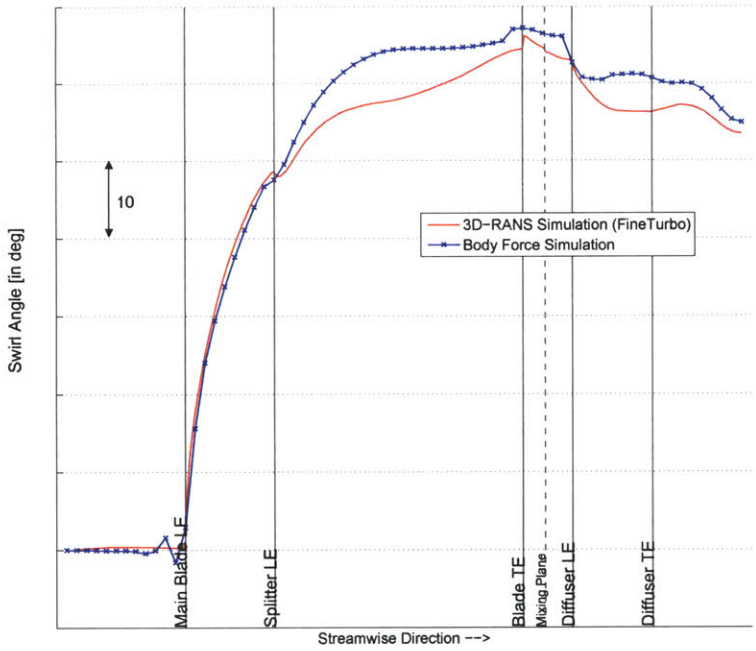


Figure 5-12: Swirl Angle. Comparison of the results from the body force simulation to those from the RANS simulation.

### 5.4.2 Spanwise Flow Distribution

An assessment of the spanwise flow distribution is carried out using contour plots in the meridional plane. Figure 5-13 illustrates the stagnation pressure in the meridional plane of the axisymmetric flow field from the body force based simulation and compares it to the pitchwise-averaged stagnation pressure from the 3-D RANS flow solution.

Overall, the two plots illustrate similar trends in stagnation pressure along the channel. However, there are also qualitative differences. While the spanwise variation of the stagnation pressure is in agreement near the inducer, the pressure rise is increasingly underestimated near the shroud towards the impeller exit. As a result, the spanwise distributions of the stagnation pressure at the impeller exit and in the diffuser are altered.

Figure 5-14 shows spanwise profiles of the stagnation pressure at four locations in the compressor in more detail. The two plots at the top show the spanwise variation in the inducer (left) and at a distance of approximately half of the blade chord into

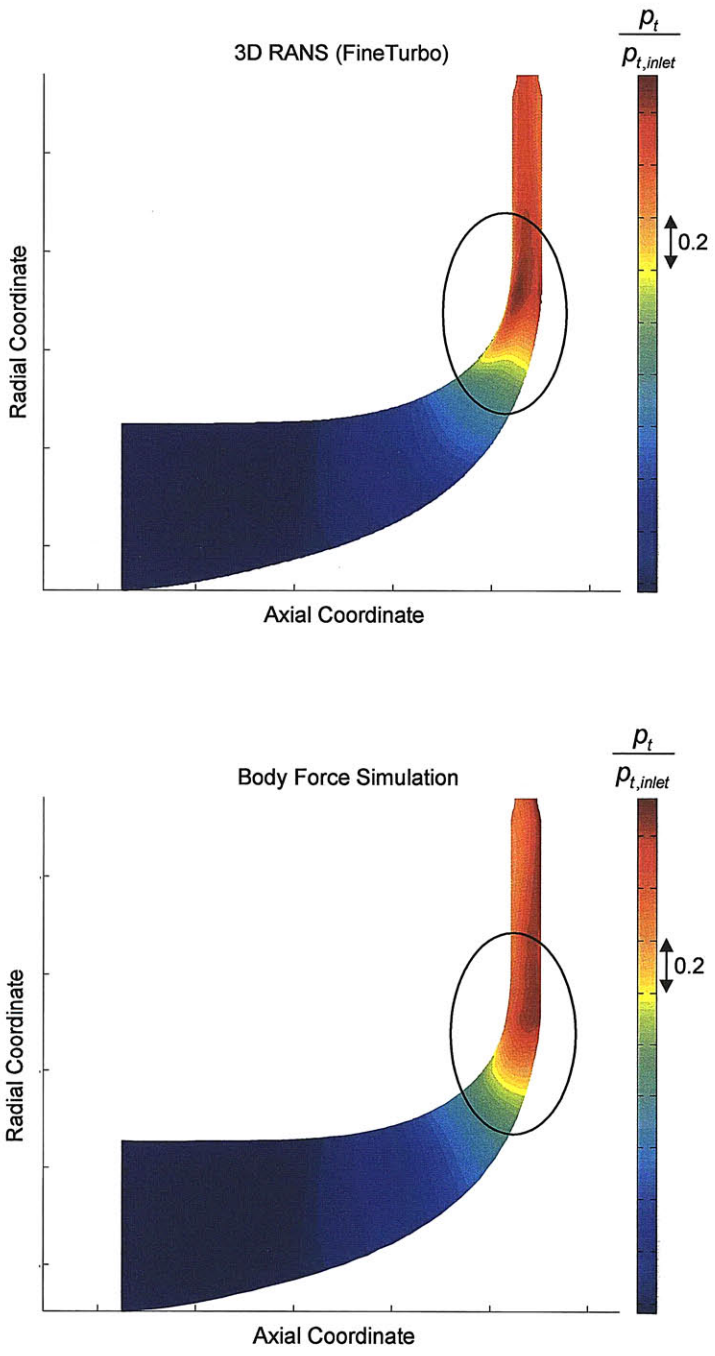


Figure 5-13: Stagnation pressure distribution in the meridional plane. Top: pitchwise-averaged stagnation pressure from 3-D RANS simulation. Bottom: stagnation pressure in the axisymmetric flow field simulated by the body force model.

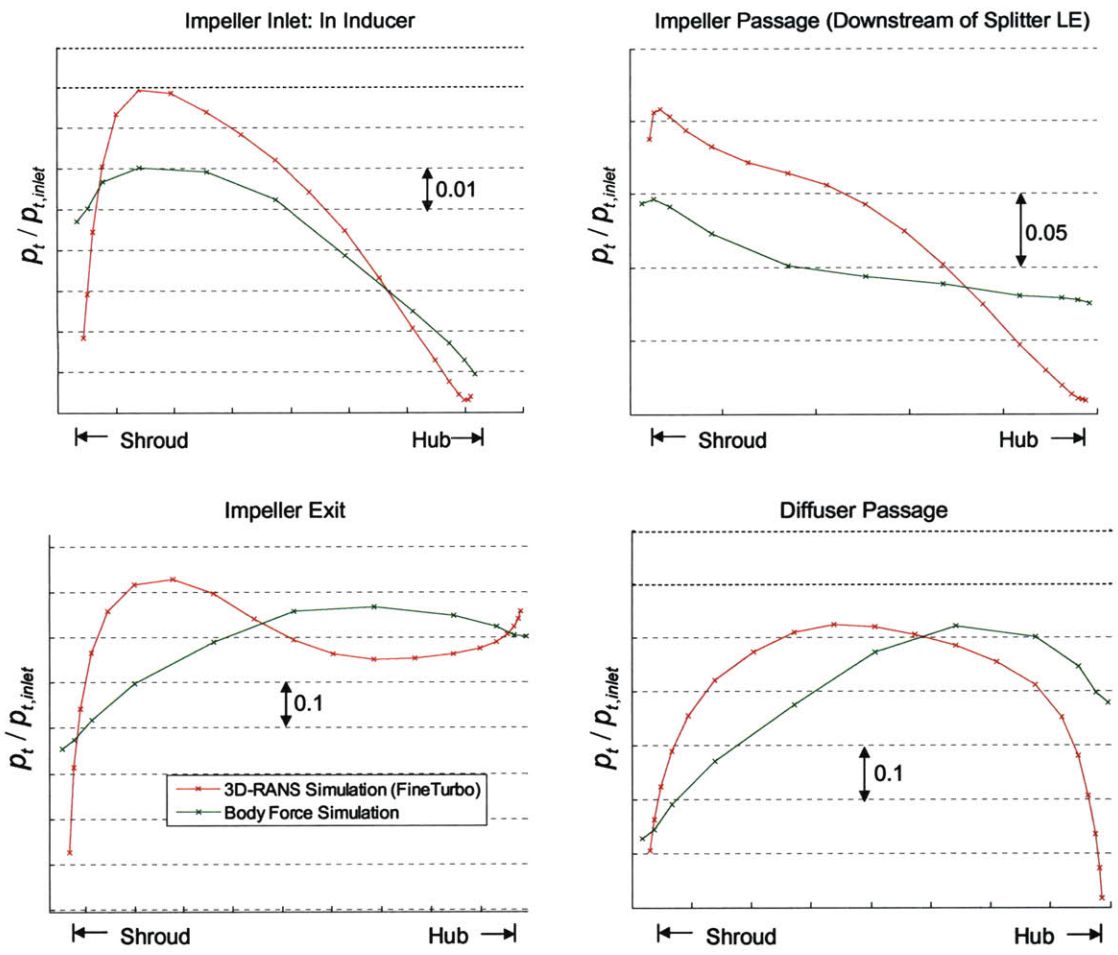


Figure 5-14: Spanwise profiles of the stagnation pressure in the impeller and diffuser. Comparison of the steady 3-D RANS calculation with the body force simulation.

the impeller passage (right). At both locations, the body force simulation underestimated the magnitude of the spanwise variation; however, the sign of the slopes in the spanwise profiles are captured.

The subplots at the bottom illustrate the spanwise profiles at the impeller exit (left) and half of the blade chord into the diffuser passage. At the impeller exit, the body force simulation underestimates the stagnation pressure at the shroud side and does not capture the local maximum near the shroud. The difference in the spanwise profile in the diffuser passage can be attributed to the altered diffuser inflow. While the 3-D RANS simulation calculates a nearly symmetric stagnation pressure profile in the diffuser passage, the body force results show the maximum in the stagnation pressure shifted to the hub side.

Figure 5-15 shows the distributions of the absolute Mach numbers in the meridional plane estimated by the 3-D RANS calculation and the body force model. Similar to the stagnation pressure analysis, the region of high Mach number at the impeller exit is shifted towards the hub. The non-uniform impeller exit flow then experiences an adverse pressure gradient in the diffuser. The low-stagnation pressure fluid near the shroud in the body force simulation is unable to overcome this static pressure rise and separates near the shroud endwall. The separation is manifested by a large region of low Mach number flow.

In summary, there are differences in the spanwise profiles between the steady RANS simulations and the quasi-steady body force based simulations. To determine whether the differences affect the dynamic behavior of the compressor, unsteady simulations are carried out and discussed in Chapter 6.

## 5.5 Body Force Dependence on Local Flow Field

During stall inception at low flow conditions, the local meridional Mach number might be beyond the range available in the body force look-up table. Thus, the body forces have to be extrapolated to flows lower than captured in the steady RANS calculation based on which the look-up table was established. To assess these assumptions, quasi-steady simulations close to stall are assessed for which the body force look-up table is extrapolated.

Figure 5-16 shows the meridional plane of the compressor duct and illustrates the locations in the domain where the body forces are extrapolated. In the left figure, operating point #1 in Figure 5-1) is assessed. The figure on the right corresponds to the last operating point #3 for which the steady solver converges. Green cells indicate force values at local meridional Mach numbers within the look-up table, while red cells indicate cells for which the local forces are extrapolated. As discussed in Section 3.4.2, for local meridional Mach numbers outside the available range, the force was equal to the last available force value in the table. This ensures that the body forces are bound, which helps avoid numerical divergence issues.

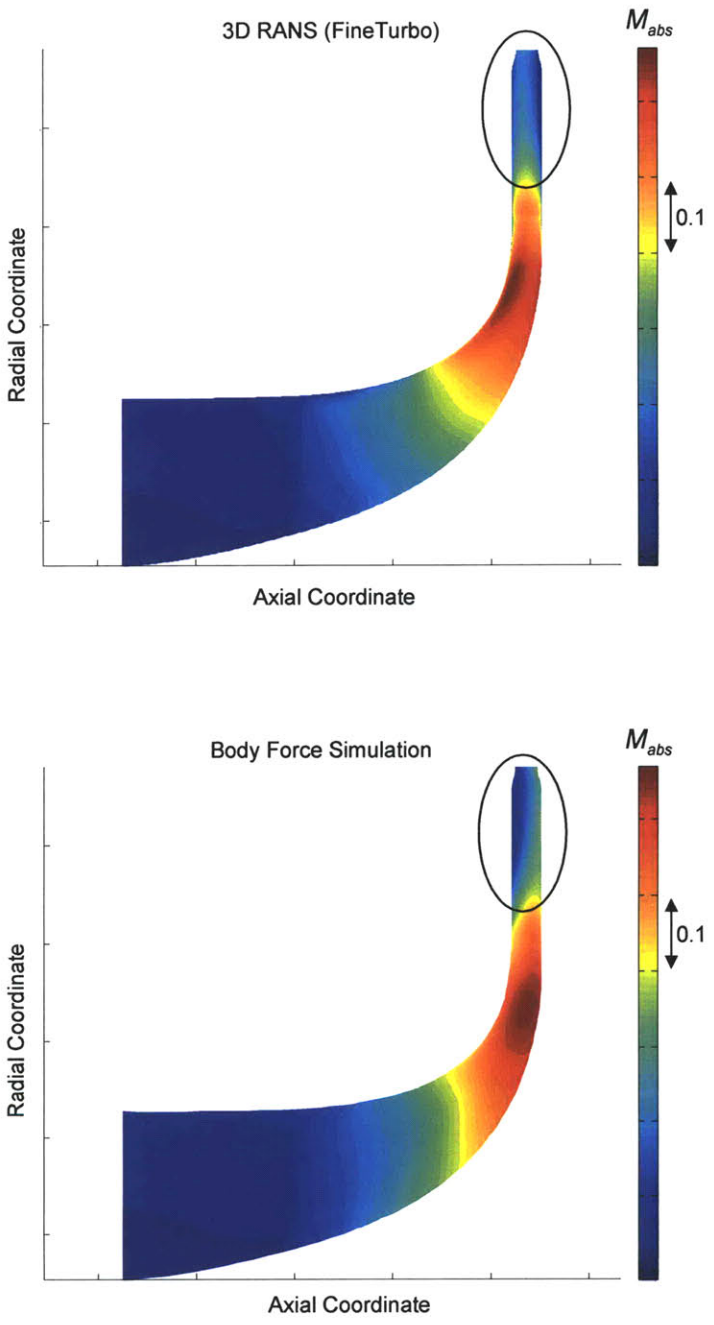


Figure 5-15: Absolute Mach number contours in the meridional plane. Top: pitchwise-averaged Mach number from 3-D RANS simulation. Bottom: Mach number in the axisymmetric flow field simulated by the body force model.

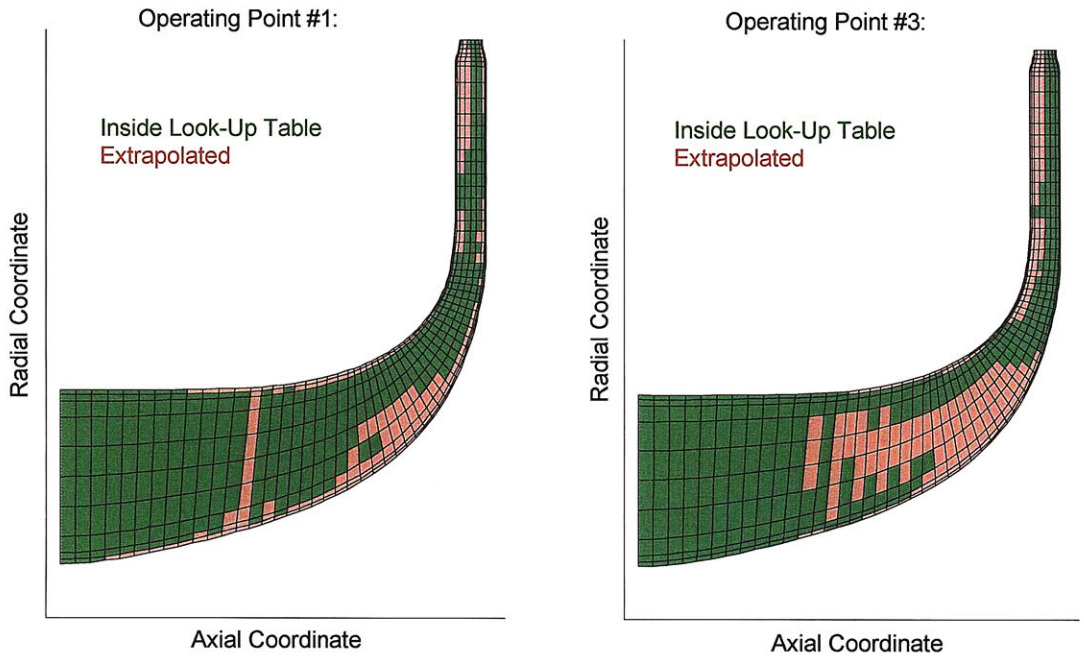


Figure 5-16: Body force look-up table entries for operating point #1 (left) and operating point #3 (right): greens cells indicate local meridional Mach numbers within the look-up table range. Red cells indicate extrapolated body forces.

For the last stable operating point (#1), it was observed that approximately 80% of the flow domain accesses body force values within the look-up table. Particularly at midspan, the body force values correspond to meridional Mach numbers in the range of the look-up table.

An appreciably-sized patch in which local body forces are outside the look-up table range is observed in the diffuser near the shroud endwall. The occurrence of this patch can be attributed to the flow separation near the shroud endwall. At operating points close to stall, the cells in the flow domain access the body force at the look-up table on the low $M_m$ side since the overall mass flow and the meridional Mach numbers are low. The flow separation due to the underestimated stagnation pressure at the shroud then further decreased the meridional Mach number. As a result, the local body forces are required for meridional Mach numbers outside of the available look-up table range.

A similar effect occurs near the hub side in the impeller passage. The spanwise variation in Mach number is altered in the body force based simulation compared to

the 3-D RANS simulation. The body forces are thus extrapolated for cells near the impeller hub.

The analysis suggests that the numerical errors discussed in Section 5.4 are sufficient to alter the meridional Mach number to values beyond the limits of the available look-up table range. However, the analysis discussed here demonstrates that the body force model can capture the steady flow field with reasonable agreement even though the body forces are extrapolated for about 20% of the cells in the flow domain.

Equivalently, the right-hand figure illustrates the access of the look-up table for the dynamically unstable operating point (#3). For this operating point, the meridional Mach numbers were further decreased due to the lowered mass flow. As a consequence, the number of cells outside the look-up table range is increased. A considerable fraction of cells at midspan in the impeller passage accesses extrapolated values in the look-up table. It is suggested that this contributes to the altered slope of the total pressure ratio characteristic at low flow, as seen Figure 5-1).

## 5.6 Body Force Based Simulation at High Speed

As discussed earlier, the absolute Mach number in the transonic flow field at the impeller exit is overestimated for the operating points at 75% corrected design speed (see figure 5-8). The relative difference in absolute Mach numbers between the body force model and the 3-D RANS results is estimated to approximately 7%, considerably higher than the numerical inaccuracies in the stagnation states $p_t$ and $T_t$. The relatively large error in Mach number can be attributed to the high sensitivity of corrected flow to small errors in the stagnation quantities at transonic conditions.

To illustrate this sensitivity, the problem can be reduced to quasi-one-dimensional, compressible channel flow. The corrected flow per unit area $D(M)$ is a function of Mach number only:

$$\frac{\dot{m}\sqrt{RT_t}}{Ap_t\sqrt{\gamma}} = \frac{M}{\left(1+\frac{\gamma-1}{2}M^2\right)^{\frac{1}{2}\left(\frac{\gamma+1}{\gamma-1}\right)}} = D(M)$$

.

As seen in Figure 5-17, the corrected flow per unit area, $D(M)$, flattens in the vicinity of $M = 1$. Hence, a flow with Mach number near unity can exhibit substantial changes in Mach number for small changes in corrected flow.

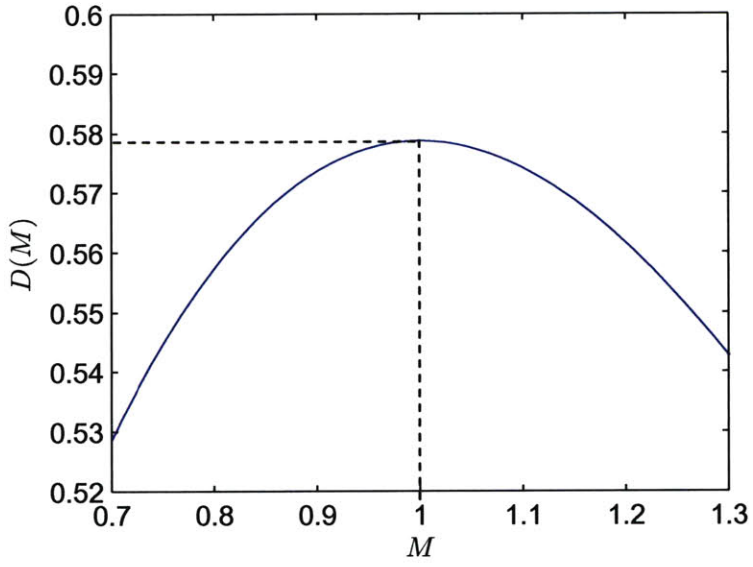


Figure 5-17: Corrected flow versus Mach number. $\gamma = 1.4$

In the simulation, numerical inaccuracies of 3.0% in the stagnation pressure alters the correct flow per unit area $D(M)$ by approximately 2.99%. For transonic flow at $M = 0.8$, this numerical inaccuracy in stagnation pressure can causes an error of 13% in the absolute Mach number. For the given numerical error in $p_t$, this error in the Mach number is further increased as the Mach number approaches unity.

At 75% design speed, the sensitivity of the subsonic flow near the impeller exit lead to a 7% error in absolute Mach number. However, at 100% design speed, the absolute Mach number is further increased and exceeds unity at the impeller exit. Figure 5-18 depicts the absolute Mach number in the meridional plane. The top figure corresponds to the pitchwise-averaged flow field calculated by FineTurbo, while the bottom figure illustrates the results from the body force simulation.

The 3-D RANS results show a region of high subsonic flow near the shroud. However, the body force simulation overestimates the increase in Mach number near the shroud. As a consequence, a supersonic patch is formed and is terminated by a shock.

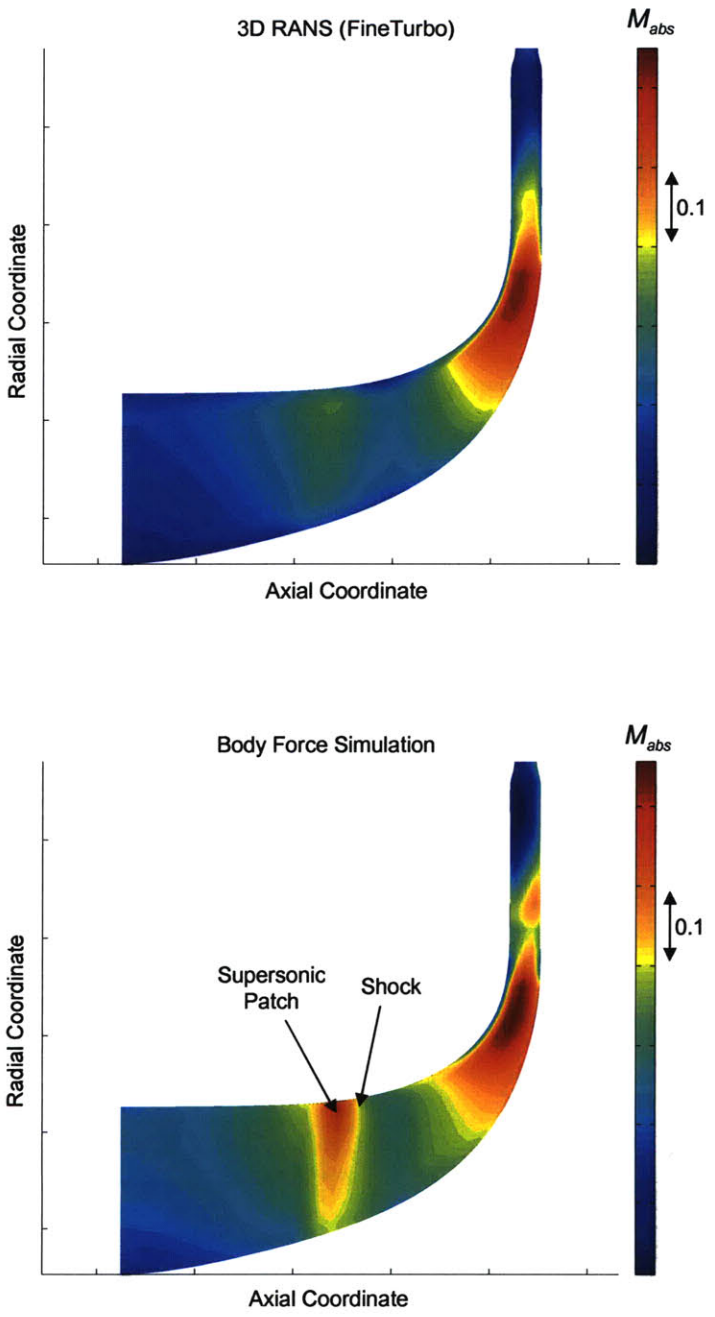


Figure 5-18: Absolute Mach number contours in the meridional plane at 100% speed near the design point. Top: pitchwise-averaged Mach number from 3-D RANS simulation. Bottom: Mach number in the axisymmetric flow field simulated by the body force model.

The supersonic patch is observed at several operating points at design speed and is usually accompanied by convergence problems in the body force based simulation.

In summary, the analysis suggests that the numerical errors in the stagnation quantities are responsible for the discrepancy in the flow field and numerical convergence problems. To capture the high speed case correctly, the sensitivity of the results to grid resolution needs to be investigated. The grid resolution needs to be increased, resulting in a trade-off between numerical accuracy and computational cost. In the work described here, it was decided to demonstrate the stall prediction at reduced speed where numerical convergence issues are not encountered.

# Chapter 6

# Unsteady Stall Inception Simulations

This chapter discusses the unsteady simulations using the body force model and investigates the stability limit and the stall inception pattern in the centrifugal compressor with vaned diffuser. To conduct the stability investigation at a selected operating point, the unsteady response of the compressor flow field to a localized forcing near the impeller exit is computed. At 75% corrected design speed, the body force model predicts the formation of a backward-traveling modal wave at operating conditions where the diffuser static pressure rise characteristic changes slope from slightly negative to positive.

Figure 6-1 depicts the different characteristic and its slope obtained from the quasi-steady, body force based simulation at 75% correct speed. The following sections discuss the unsteady simulations for the operating points at 75% speed marked by #1, #2, and #3. At operating point #1, the slope of the static diffuser pressure rise characteristic is slightly negative. The non-linear response to the forcing has a maximum amplitude of approximately 4% of the inlet pressure at the vaneless space inlet and dies out after a few rotor revolution. This operating point is thus deemed stable.

At operating point #3, the slope of the characteristic is positive and a backward-traveling modal stall precursor is formed that grows exponentially in amplitude. The

backward-traveling character of the long-wavelength disturbance was found to be in agreement with predictions by the analytical compression system stability model developed by Spakovszky [28] and experimental measurements by Spakovszky and Roduner [29].

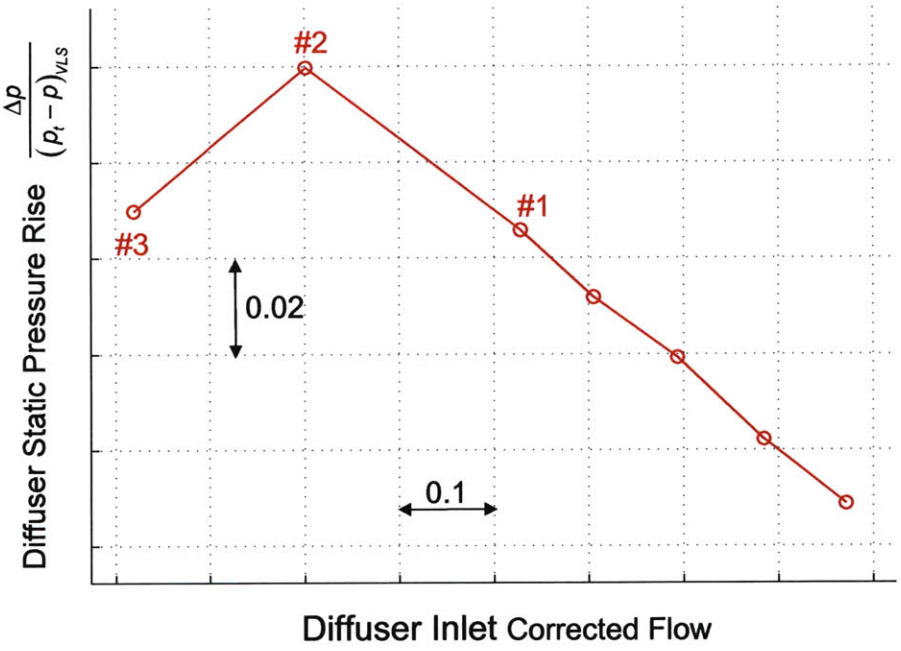


Figure 6-1: Diffuser static pressure rise characteristic at 75% corrected design speed.

To explore the generation of short-wavelength spike-like stall precursors, unsteady simulations were also performed for an altered compressor, which was obtained by scaling the body force look-up table at 100% corrected design speed down to a corrected design speed of 75%. This alters the matching between the impeller and diffuser and yields a different dynamics behavior, changing the path into instability from modal waves to short-wavelength stall precursors.

Finally, the body force look-up table entries are assessed for the unsteady simulation at operating point #3. With growing amplitude of the modal wave, more and more cells in the computation accessed the body force look-up table at meridional Mach numbers outside the available range from the 3-D RANS simulations. The assessment shows that the formation of the modal waves is simulated based on body forces within the look-up table for the cells in the impeller and diffuser, while the

transition to the full-scale instability cannot be captured with the currently available data in the body force look-up table.

## 6.1 Dynamic Compressor Stability Investigation

The quasi-steady flow fields discussed in Section 5.1 were obtained by running unsteady, axisymmetric compressor simulations with the body force model until a time-invariant flow solution was achieved. To investigate the stall inception at the selected operating point, this quasi-steady flow field was locally forced for a short period of time. The dynamic pressure near the shroud at the impeller exit was increased by 25% and the forcing was spatially confined to 10% of the circumference and approximately 30% in the spanwise direction. The forcing was put in place for 1/10th of a rotor revolution. After 1/10th of a rotor revolution, the forcing was deactivated and the unsteady response of the compressor flow in the vaneless space was assessed. The magnitude, spatial extension, and duration of the forcing was identical for all unsteady simulations discussed in this chapter.

To analyze the results and compare them to experimental data, the unsteady pressure signal near the shroud endwall in the vaneless space was recorded at several locations around the circumference. These locations are marked by the green and the red dots in Figure 6-2 and are identical to the locations of the unsteady pressure sensors in the experiments by Spakovszky and Roduner [29].

## 6.2 Stable Operating Point Simulation

The compressor stability investigation is first at conducted at operating point #1 (see Figure 5-1). The slope of the diffuser static pressure rise characteristic is negative at this operating point, as seen in the steady simulations described in Section 5.1.

The unsteady response of the flow field at this operating point to the forcing in the vaneless space is illustrated in Figure 6-3. The curves correspond to the unsteady pressure signal from the eleven pressure sensors shown in Figure 6-2. The

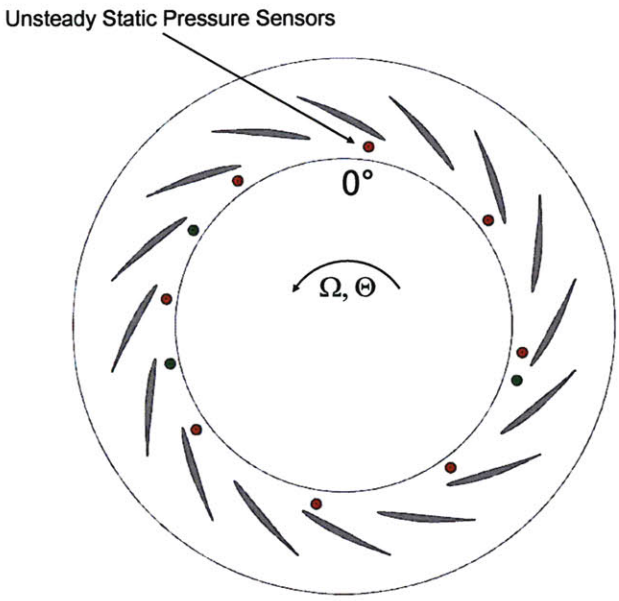


Figure 6-2: Locations of unsteady static pressure sensors in vaneless space. Eight sensors are equally spaced with two blade pitches separation (red) and three sensors are located in between (green). Figure adopted from [29]

pressure signals are non-dimensionalized by the vaneless space inlet dynamic pressure, $(p_t - p)_{VLS}$. The pressure signals are plotted according to their circumferential location relative to the first sensor at $\theta = 0°$.

Before the forcing is imposed at a time of zero rotor revolutions, the flow field is time-invariant and axisymmetric. The pressure in this time-invariant flow field serves as the reference pressure. Starting at time zero, the forcing is introduced for 1/10 of a rotor revolution. After a 1/10 rotor revolution, the forcing is deactivated and the dynamic response of the flow field is computed for 18 rotor revolutions, as shown in Figure 6-3.

The amplitude of the response decays over time, and after approximately 6-8 rotor revolutions, the time-invariant, axisymmetric flow field before the forcing is recovered. The operating point is therefore deemed dynamically stable.

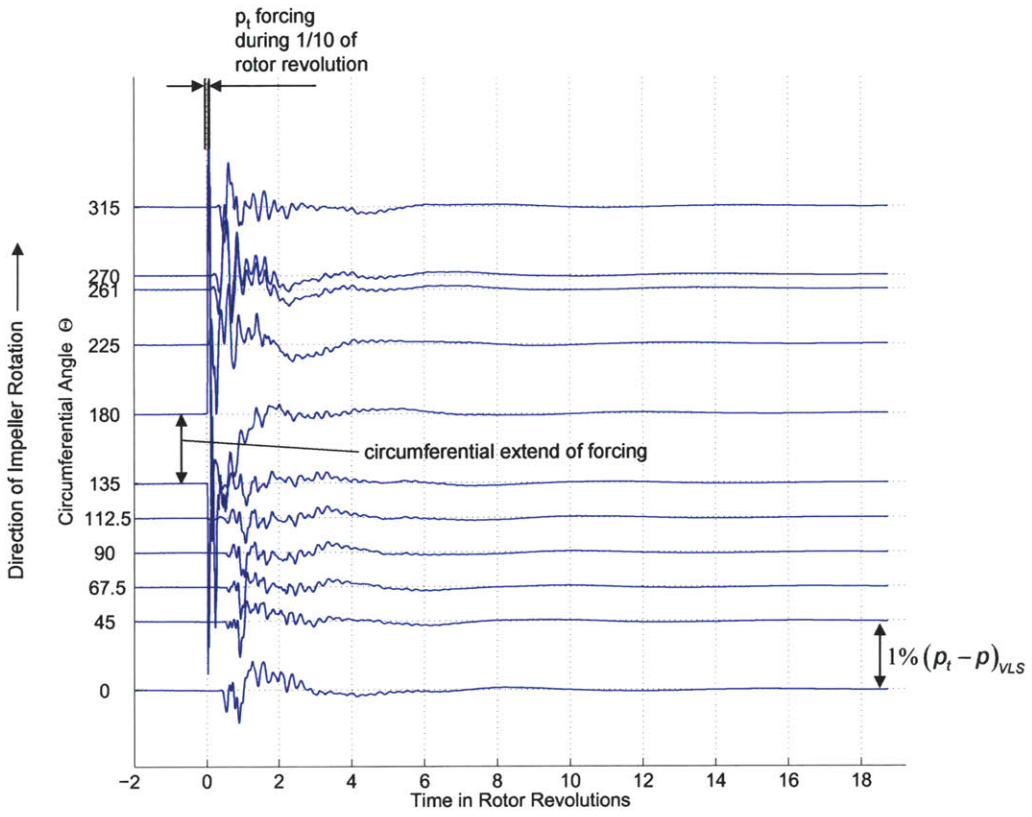


Figure 6-3: Unsteady pressure traces in the vaneless space at 75% corrected design speed: flow perturbations decay in time - dynamically stable operating point.

## 6.3 Backward-Traveling Modal Stall Waves

Next, the stability at an operating point with a positively sloped diffuser static pressure rise characteristic is investigated. Figure 6-4 illustrates the unsteady response of the flow field to forcing at operating point #3. To capture the amplitude, the scale of the plot is increased by a factor of 4 compared to Figure 6-3.

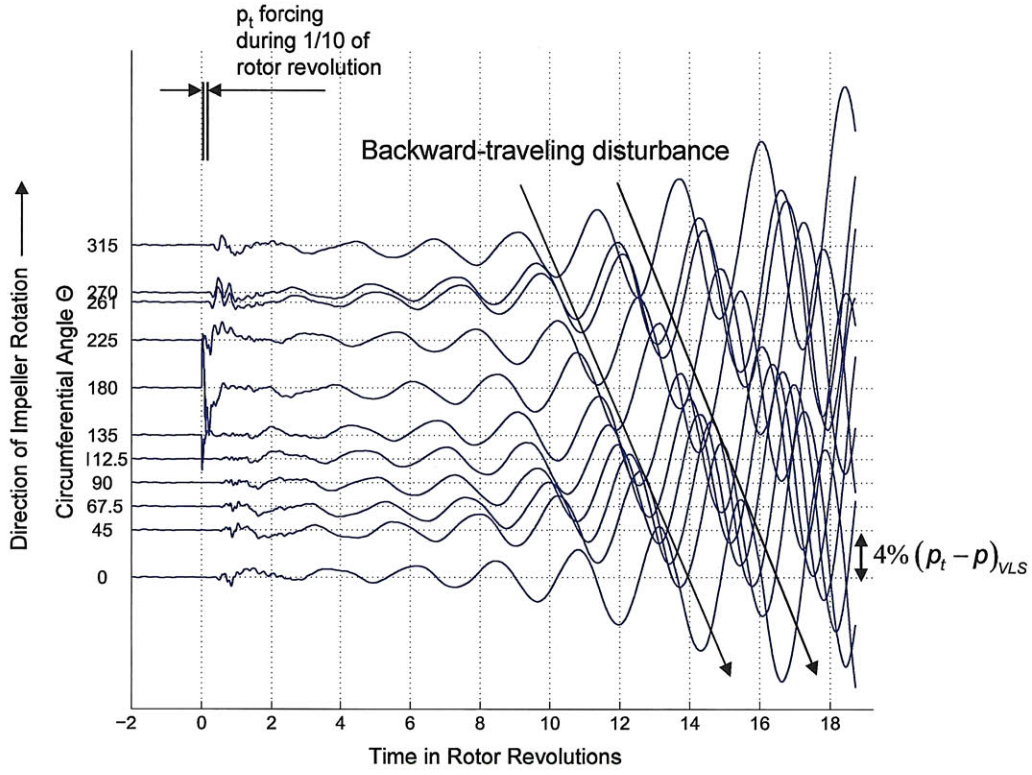


Figure 6-4: Unsteady pressure traces in the vaneless space at 75% corrected design speed: two-lobed backward-traveling modal waves rotating at 20%-25% rotor speed grow in amplitude.

As before, the quasi-steady compressor flow field is forced at time zero. The forcing is identical to the one used in the computation at operating point #1. Similar to operating point #1, the flow field at operating point #3 initially responds to the non-linear forcing. However, shortly after the forcing, a backward-traveling modal wave is formed that grows exponentially in amplitude. Operating point #3 is thus deemed dynamically unstable.

Further analysis of the pressure traces reveals that the wave fronts of a second

spatial harmonic prestall wave travel against the impeller direction at about 20-25% of the rotor speed. The propagation of the wave fronts is indicated by the black arrows in figure 6-4. The negative slope of the arrows with respect to time indicates the backward-traveling character of the wave.

An additional unsteady simulation was performed near the peak of the diffuser pressure rise characteristic where the slope is approximately zero. Figure 6-5 shows the forcing at operating point #2. Again, the forcing is imposed at time zero. Similar to the unstable operating point #3, a backward-traveling modal wave is formed. The analysis shows that the spatial structure and the speed of propagation are in agreement with the modal wave in Figure 6-4. However, the amplitude of the disturbance is maintained over time, indicating that the disturbance energy added by the compressor blade rows is in balance with the dissipation in the dynamic system. The operating point is therefore deemed neutrally stable.

To summarize, the unsteady simulations for operating points #1, #2, and #3 suggest that the dynamic compressor behavior and the formation of modal stall precursors in the vaneless space can be related to the slope of the diffuser static pressure rise characteristic. The operating points where the slope in the diffuser characteristic is slightly negative are stable. However, the diffuser flow is dynamically unstable to the formation of modal waves for operating points that have a diffuser static pressure rise characteristic with a positive slope. Near, the peak of the characteristic, the slope is approximately zero and the compressor is neutrally stable.

## 6.4 Comparison to Experimental Measurements

High-speed experiments were previously conducted by Spakovszky and Roduner [29] and showed the existence of long-wavelength disturbances prior to full-scale instability in the centrifugal compressor. Experimental measurements are not available at 75% corrected design speed, but it is instructive to compare unsteady simulations to compressor dynamic behavior at 100% and 105% corrected design speed.

Figure 6-6 depicts two pressure rise characteristics of the vaned diffuser at 105%

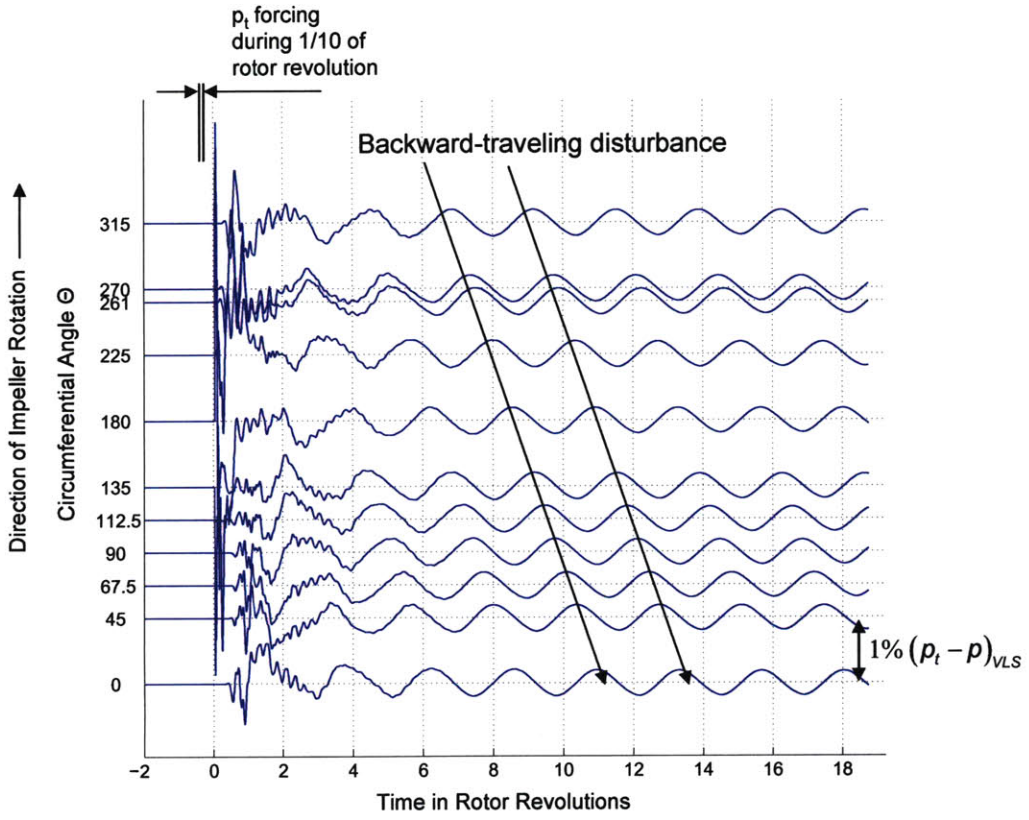


Figure 6-5: Unsteady pressure traces in the vaneless space at 75% corrected design speed: two-lobed, backward-rotating modal waves rotate at 20%-25% of rotor speed and maintain their amplitude.

design speed. Without endwall leakage flow (bleed valve closed), the characteristic plateaus before surge occurs and the stall inception is characterized by a short-wavelength "spike-like" disturbance. With endwall leakage flow (bleed open), the diffuser static pressure rise characteristic peaks, and the slope changes from negative to positive. In this case, long-wavelength modal prestall waves were observed before the onset of the full-scale instability (see Figure 6-7).

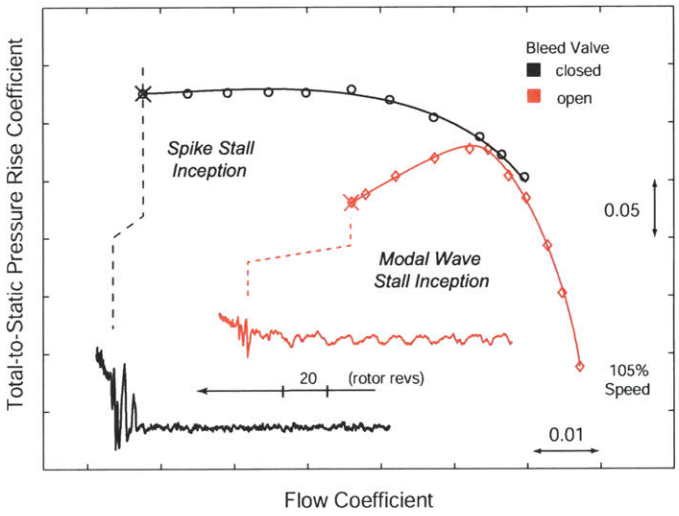


Figure 6-6: Two paths into instability: spike and modal stall patterns in centrifugal compressor with vaned diffusers. Figure adopted from Spakovszky and Roduner [29].

The body force simulation at 75% corrected design speed shows a similar behavior to the experimental measurements at 105% (see Figure 6-7) in that modal waves are formed in the vaned diffuser at operating points with a positive slope in the diffuser static pressure rise characteristic. The backward-traveling character of the modal wave in the simulation is in agreement with the experimental observations. Additionally, the exponential growth of the modal stall precursor predicted by the unsteady simulation is in agreement to the experimental measurements. The experimentally measured pressure signal at 100% corrected design speed is depicted in Figure 6-8.

However, it was also observed that the waves in the simulation at 75% and in the experiments at 105% differ in their spatial structure and their propagation speed. While the experiments (see Figure 6-7) indicate a four-lobed spatial wave that travels at about 8% of rotor frequency against impeller rotation, the simulations show a

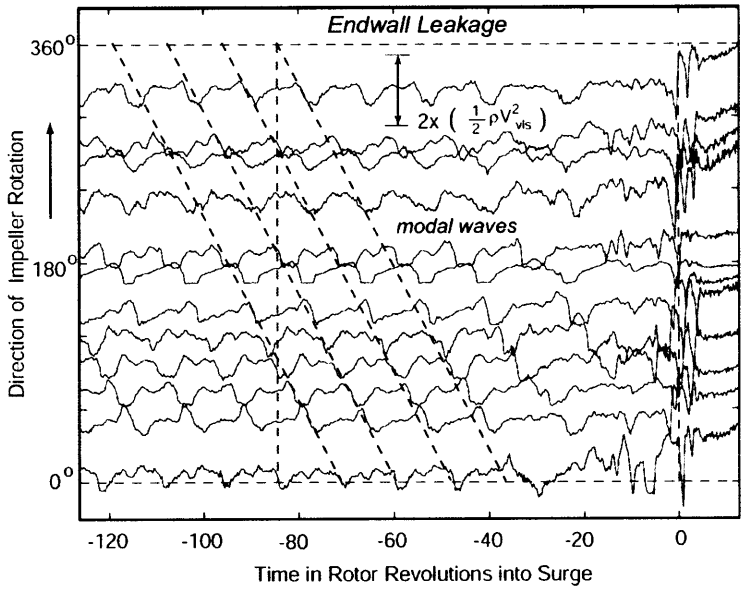


Figure 6-7: Experimentally determined unsteady pressure traces for test compressor at 105% corrected design speed with endwall leakage in vaneless space. Figure adopted from Spakovszky and Roduner [29].

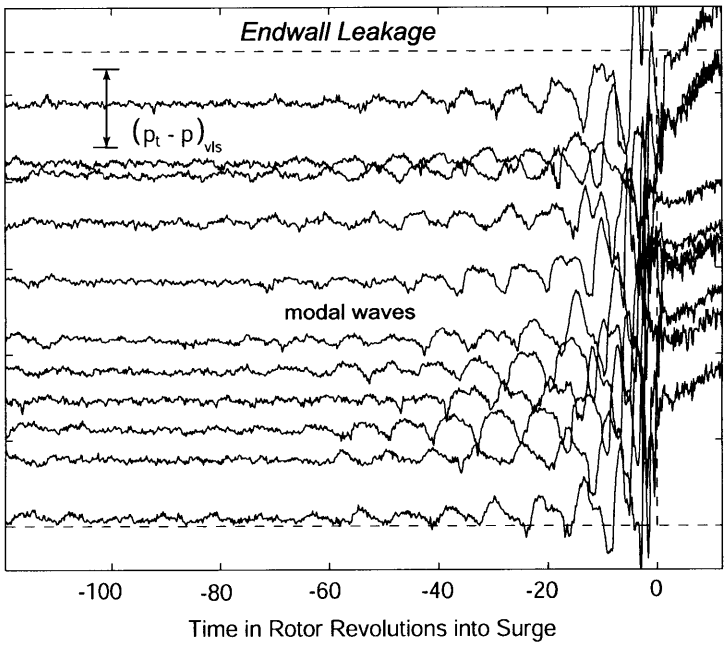


Figure 6-8: Experimentally determined unsteady pressure traces for test compressor at 100% corrected design speed with endwall leakage in vaneless space. Figure adopted from Spakovszky and Roduner [29].

two-lobed spatial periodicity that travels at about 20% to 25% of rotor frequency. Besides the different impeller speeds, a potential reason for the discrepancy between the experimental and computational results is the difference in the amplitudes of the modal waves between the simulation and the experiment. In the experiment, the modal waves detected in the vaneless space have already grown to a considerable fraction of the vaneless space inlet dynamic pressure. The backward-traveling waves in Figure 6-7 have an amplitude of approximately one vaneless space inlet dynamic head. This amplitude is large enough for the nonlinearities in the compressor map to be perceived, which is indicated by the almost rectangular wave shape [29].

In the computation, the modal waves that grow over 18 rotor revolutions (see Figure 6-4) reach an amplitude of 11% of the vaneless space inlet dynamic pressure. In the almost noise-free numerical environment, these modal waves are still sinusoidal, indicating linear behavior. It is therefore suggested that the dynamics in this linear regime are different and a different mode (resonance in the flow field) governs the instability at lower rotor speed.

Due to the limited range of the body force look-up table from the available steady RANS simulation, the transition to larger amplitudes or even full-scale instability cannot be simulated in the body force model, Note however that the objective of the model developed in this work is to investigate the onset of stability and the formation of the stall precursors, rather than the full-scale instability.

## 6.5 Simulation of Short-wavelength "Spike-Like" Disturbances

Spakovszky and Roduner [29] demonstrated that, depending on the matching between impeller and vaned diffuser in highly-loaded centrifugal compressors, either long-wavelength modal waves or short-wavelength spike-like stall precursors can occur before full-scale instability is initiated. For the test compressor operating at 75% corrected design speed, the simulation showed the formation of modal stall precursors

at operating points with a positively sloped diffuser static pressure rise characteristic, in agreement with experimental results.

To demonstrate the simulation of short-wavelength stall precursors, the matching between impeller and diffuser was altered, yielding different compressor performance and dynamic behavior. As discussed in Section 3.4.2, the magnitude of the body forces scales with square of the impeller tip speed. The altered compressor stall was obtained by scaling the body forces based on 3-D RANS calculations at 100% corrected design speed to 70% corrected design speed. Hence, the magnitudes of the body forces in the look-up table were scaled by a factor of $(0.7)^2 = 0.49$.

First, the body force model was used to perform quasi-steady simulations at different back-pressures for the altered test compressor at 70% corrected design speed. Figure 6-9 depicts the resulting total pressure ratio characteristic. For comparison, the results from the RANS simulations and body force based simulations of the test compressor used in Chapter 5 are also plotted. Note that the modification of the body force look-up table to obtain an altered compressor significantly changed the mass flow through the machine.

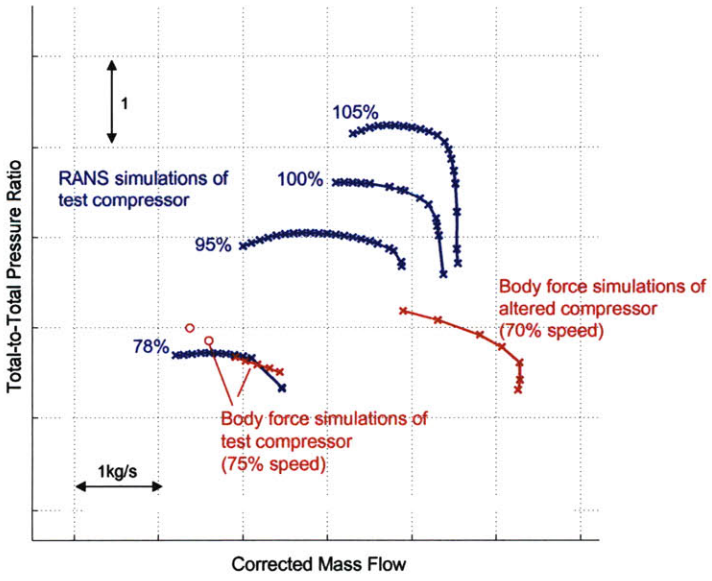


Figure 6-9: Total pressure ratio characteristic of the test compressor at 70% corrected design speed, in comparison to the results for the test compressor from Chapter 5.

The compressor stability and the stall inception are investigated using unsteady simulation with the body force model, as discussed before. The quasi-steady flow field from a selected operating point close to stall is perturbed by forcing the flow field during 1/10 of a rotor revolution. The forcing magnitude and extension are identical to those used previously.

Figure 6-10 shows the dynamic response to the forcing for the operating point at the left end of the characteristic. Shortly after forcing, a forward-traveling, short-wavelength disturbance is born in the vaneless space. The detailed analysis of the pressure signal reveals that the spike-like perturbation travels in the direction of the rotor direction at approximately 60% rotor frequency. The amplitude of the disturbance is about 0.6% of the vaneless space inlet dynamic pressure head. The amplitude remains constant over time.

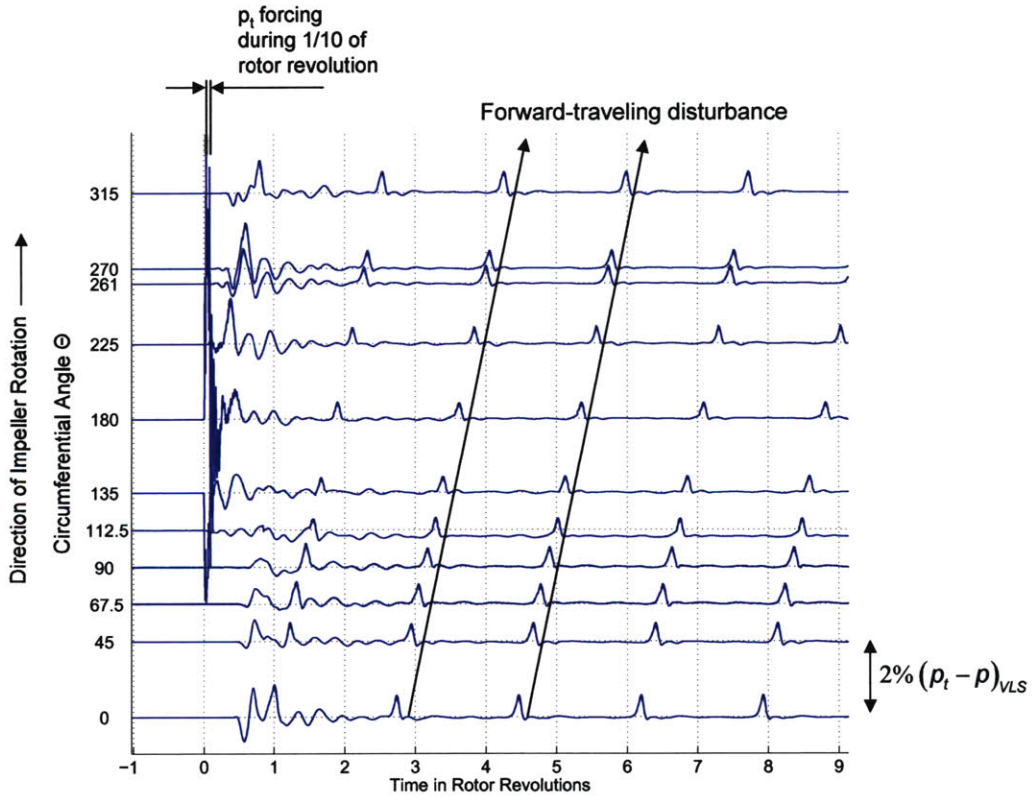


Figure 6-10: Unsteady pressure traces in the vaneless space for the altered test compressor at 70% corrected design speed. A forward-traveling, short-wavelength, spike-like disturbance is formed shortly after forcing.

The computed short-wavelength disturbances agree with the experimentally observed stall precursors (see Figure 1-2b) in that the disturbance travels in the direction of the impeller rotation. A key difference between the simulation and the experiments is that the short-wavelength disturbances in the experiments grow quickly in amplitude and trigger full-scale instability after only a few rotor revolutions.

The pre-stall disturbance does not grow in amplitude in the simulation. A possible reason for the difference is that the last simulated operating point is neutrally stable, such the disturbance cannot extract energy from the flow field. Furthermore, it is possible that the limited range of the body force look-up table does not allow the disturbance to grow to larger amplitude.

In summary, the body force model is capable of capturing the formation of short-wavelength, spike-like stall precursors. Further work is required to investigate the flow mechanisms responsible for the formation of the short-wavelength disturbances and to establish a criterion for their occurrence.

## 6.6 Body Force Look-Up Table Usage in Unsteady Simulations

As discussed earlier, the flow field information obtained from the steady RANS simulations is limited to operating points near the peak of the total pressure rise characteristic. The body force look-up table established in Section 3.4.2 uses this information to describe the body force components as functions of the local meridional Mach number. However, in non-axisymmetric flow during stall inception, the local flow conditions can differ considerably from the flow conditions in the steady flow fields. Depending on the amplitude of the stall precursor, body force information is requested for meridional Mach numbers reduced below the values available in the look-up table.

In this first approach, the body force extrapolation is performed by keeping the last available data point in the look-up table constant for meridional Mach numbers below the tabulated value. This conservative approach prevents numerical difficulties due

to excessive body forces. At the same time, the body force model can still capture the dynamic behavior of the disturbances during stall inception, since the body forces are computed from 3-D RANS calculations where the slope of the diffuser total pressure rise characteristic is positive. Nonetheless, this approach sets an upper limit on the amplitude of the disturbances that can be simulated reliably with the data available from the steady RANS simulations.

As shown in Section 5.1, the steady compressor flow field is in good agreement with the 3-D RANS results, although the body forces are locally extrapolated near the shroud and hub endwalls. This section analyzes the use of the body force look-up table during the unsteady simulation at operating point #3 (see Figure 6-4). Cells at midspan, at which the amplitude of the disturbance is large enough to exceed the look-up table range, are investigated.

Figures 6-11 and 6-12 illustrate the time history of the look-up table usage for a cell just upstream of the impeller leading edge and a cell in the diffuser passage. The largest force components in these cells are the tangential force at the impeller exit and the radial force in the diffuser.

For each cell, the white rectangular region on the left indicates the range of the local meridional Mach number available in the look-up table. Initially, the flow field corresponds to the quasi-steady flow solution at operating point #3, as discussed in Section 5.1. For both cells, the local meridional Mach number is within the look-up table range. Note that, since this operating point is on the stall side of the characteristic, the meridional Mach number in the cell is near the lower value of the available look-up table range.

Before the forcing is imposed at time zero, the flow field is time-invariant and the body forces remain unaltered. Shortly after forcing, a stall precursor is formed and the body forces react to the changing local flow conditions. While the wave fronts of the two-lobed pre-stall wave pass by, the meridional Mach number undergoes oscillations and grows exponentially for this unstable operating point.

After 7 to 10 rotor revolutions, the amplitude of the fluctuation is large enough such that the meridional Mach number in the trough of the wave falls below the

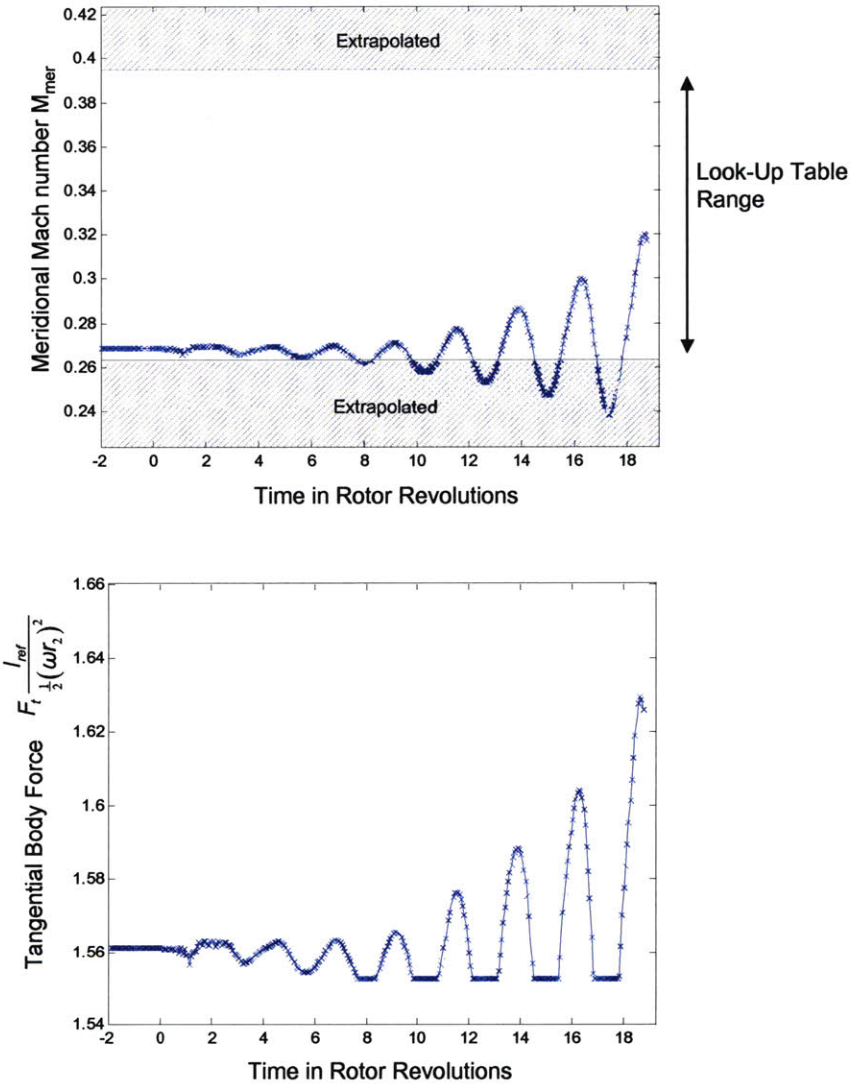


Figure 6-11: Usage of body force look-up table upstream of the impeller leading edge. Top: time trace of meridional Mach number. Bottom: time trace of implemented tangential body force.

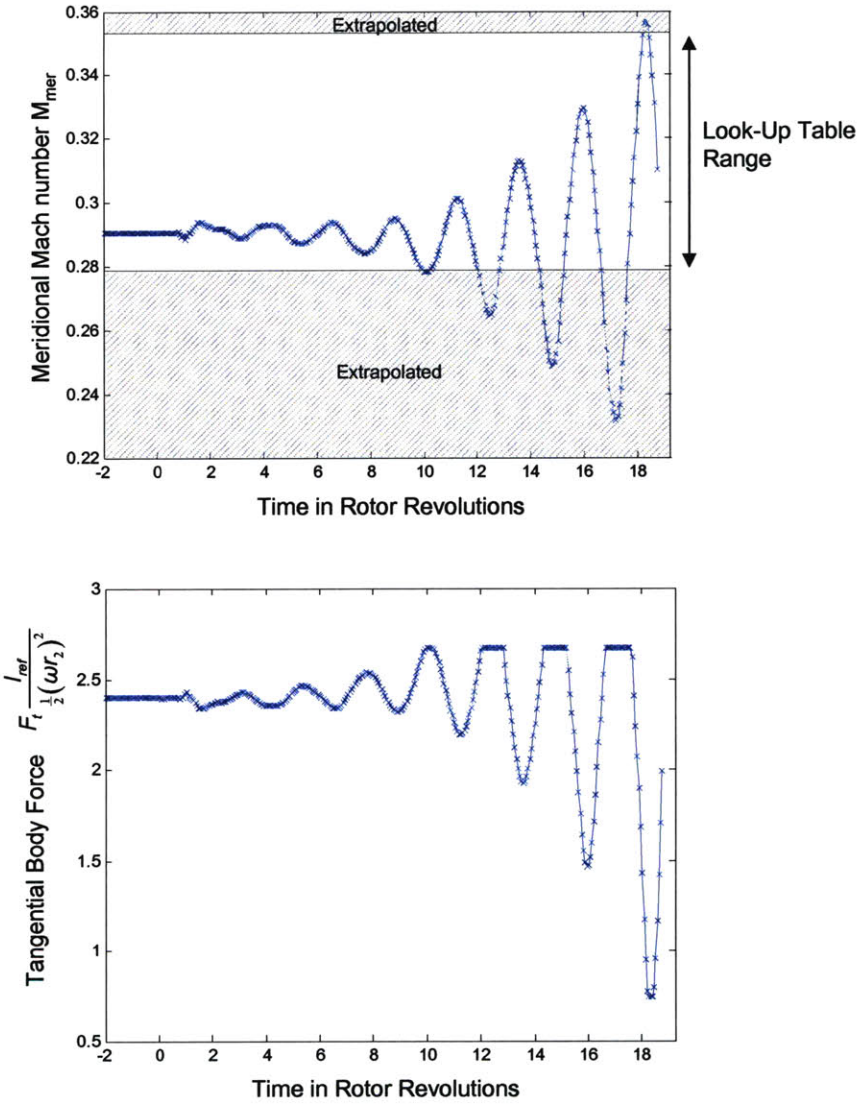


Figure 6-12: Usage of body force look-up table in diffuser passage. Top: time trace of meridional Mach number. Bottom: time trace of implemented tangential body force.

lower limit of the look-up table range. At that point, the body forces imposed in these cells are set to the last available data point in the table, which is indicated by the saturated body force value in the bottom plots in Figures 6-11 and 6-12. The analysis illustrates that despite the limitations in the body force look-up table, the formation of stall precursors can be captured based on the available data points from the 3-D RANS calculations.

## 6.7 Summary

The stability limit and the stall inception pattern in a highly-loaded centrifugal compressor with vaned diffusers were investigated by conducting unsteady body force based simulations.

At an operating point with negatively sloped diffuser pressure rise characteristic, the response to the forcing died out and the time-invariant, axisymmetric flow field was recovered. This operating point was thus deemed stable. However, at the operating point with positively sloped diffuser pressure rise characteristic, the formation of a modal stall precursor was predicted which grows exponentially in amplitude, indicating an unstable operating point. Compared to the experimental measurements at 105% corrected design speed, the simulation at 75% corrected design speed showed a similar behavior to in that the modal waves are formed in the vaneless space at the operating point where the slope of the diffuser pressure rise characteristic changed from negative to positive. Additional investigations in the test compressor with altered dynamic behavior demonstrated the capability of the body force-based compressor model to capture the formation of short-wavelength spike-like stall precursor.

Finally, the analysis of the body force look-up table usage showed that the RANS based body force description is sufficient to capture the stall inception process. However, full-scale instability cannot be simulated due to the current limitations of body force look-up table.

# Chapter 7

# Summary and Conclusions

A novel and integrated methodology was established to predict the stability limit and the stall inception pattern in highly-loaded centrifugal compressors with vaned diffusers. The body force based approach is different from previous research in that the prediction is independent of compressor stability correlations and a-priori knowledge of the compressor characteristics. The methodology was applied to investigate the stall inception for a pre-production, 5.0 pressure ratio, high-speed centrifugal compressor stage of advanced design. Both long-wavelength modal stall precursors and short-wavelength spike-like stall precursors were simulated for the first time in a centrifugal compressor with vaned diffuser, in agreement with experimental measurements.

## 7.1 Concluding Remarks

The key pieces in the development of the methodology were to establish methods to derive the body force description, express the body forces as functions of local flow conditions, and to establish an unsteady, body forced based compressor model.

To obtain the body force description, steady, single-passage 3-D RANS simulations were carried out and validated against experimental data. A body force extraction method was developed capable of extracting the body force description from the 3-D RANS flow fields. These data were used by a body force interpolation scheme to

describe the body forces as functions of the local flow conditions. Combined, the methods allow determining the functional dependence between the body forces and the local flow parameters with only the 3-D compressor geometry as an input.

A computational model for the unsteady simulation of centrifugal compressor with vaned diffusers was established and implemented in an existing Euler solver. The body force based compressor model was validated against high-fidelity 3-D steady RANS calculations of the test compressor. At 75% corrected design speed, the body force based compressor simulations demonstrated good agreement with the 3-D RANS simulations yielding errors in global parameter performance and local flow quantities within a few percent. At design speed, the sensitivity of the highly-transonic flow to numerical inaccuracies in stagnation quantities, suggested to be due to the reduced grid resolution of the Euler calculations with the body force model, were found to be responsible for qualitative differences in the flow field and convergence problems.

Based on these findings, the decision was made to first demonstrate the full methodology by investigating the stall inception in unsteady simulations at reduced speed. The body force simulation at 75% speed agrees with the experimental measurements by Spakovszky and Rodunder [29] at design speed in that the diffuser becomes unstable at operating points with a positively sloped diffuser static pressure rise characteristic. Modal stall precursors were observed and the backward-traveling character of the long-wavelength disturbance was found to be in agreement with predictions by the analytical compression system stability model developed by Spakovszky [28] and the experimental measurements [29] in the same compressor.

Additional investigations in the test compressor with altered dynamic behavior demonstrated the capability of the body force-based compressor model to capture the formation of short-wavelength spike-like stall precursor. It is the first time that the formation of backward-traveling modal waves and short-wavelength spike-like stall precursors are simulated in a centrifugal compressor with vaned diffuser using a body force based methodology combined with 3-D steady RANS computations. Further work is required to investigate the flow mechanisms responsible for the formation of the short-wavelength disturbances and to establish a criterion for their occurrence.

The current approach is limited to simulating the formation of the stall precursors. In the current implementation, the body forces were set to the last available value in the look-up table, when the local meridional Mach number exceeded the range of the RANS based look-up table. As a result, the transition to full-scale cannot be captured. Further, the low resolution of the currently used grid for the body force based simulation limited the simulations to 75% corrected design speed.

## 7.2 Future Work

The following recommendations for future work can be made based on the findings in this thesis:

- The unsteady diffuser flow field simulations should be investigated to interrogate the flow mechanisms responsible for stall inception via modes/spikes and to establish a generalized criterion for the onset of instability in centrifugal compressors.

- The analysis of the compressor simulation at high speed suggested that numerical inaccuracies due to the low resolution of the Euler grid are responsible for the discrepancy in the flow field and the convergence issues. To enable the high-speed correctly, the sensitivity of the results to grid resolution in the body force simulations needs to be investigated and the grid needs to be refined accordingly. Using a refined grid, the stability limit and the stall inception pattern at design speed should be further investigated and compared against the measured data.

- Compressor rig experiments reported by Spakovszky and Roduner suggest that the path into compression system instability can be altered by leakage flow effects at the impeller exit. Additional simulations with bleed flow to change the matching between impeller and diffuser should be conducted to investigate the underlying mechanism.

- A major challenge is to estimate the body forces beyond the range of the look-up table at conditions for which RANS simulations are not available. In the current approach, the body forces were set to the last available values in the look-up table if the local meridional Mach number exceeds the range of the RANS based table. Further studies are necessary to develop a more elaborate method to estimate the body forces for flow conditions on the positively sloped side of the compressor characteristic.

- In the present study, the volute downstream of the diffuser was not included in the compressor simulations. Reflected pressure waves due to the sudden change in impedance at the volute inlet may impact the dynamic behavior of the diffuser flow. To investigate the volute in the stall process, simulations with a volute downstream of the diffuser should be carried out.

# Appendix A

# Two-dimensional Look-Up Table

In Section 3.4.1, the local Mach number, $M$, and the local swirl angle, $\alpha$, were identified to be the main parameters governing the body force at a given location in the flow field. The two-dimensional look-up table approach describes the three force components directly as functions of these two flow parameters.

In the diffuser, the Mach number and swirl angle are determined in the stationary frame, while the body forces in the impeller domain are expressed as functions of the local relative swirl angle $\alpha_{ref}$ and the local relative Mach number $M_{rel}$.

A total of 53 operating points on three speedlines were analyzed. For each operating point and each cell in the meridional Euler grid, the force components, the local Mach number and the swirl angles were extracted. The functional dependency of each of the force components was found by spatially interpolating between the data points available for the selected impeller speed.

Figure A-1 illustrates the look-up table for a cell near the impeller exit at midspan. The plot shows the non-dimensional tangential body force component as a function of the relative Mach number and the relative swirl angle. Each cross marks a combination of reference parameters, $\alpha_{ref}$ and $M_{rel}$, for which the body force is known from a steady RANS operating point. The magnitude of the force component at a specific data point is indicated by the color code near the cross. For this cell, the simulation of the three speedlines enables an independent variation of the two input parameters, yielding a large range of values in the two-dimensional space.

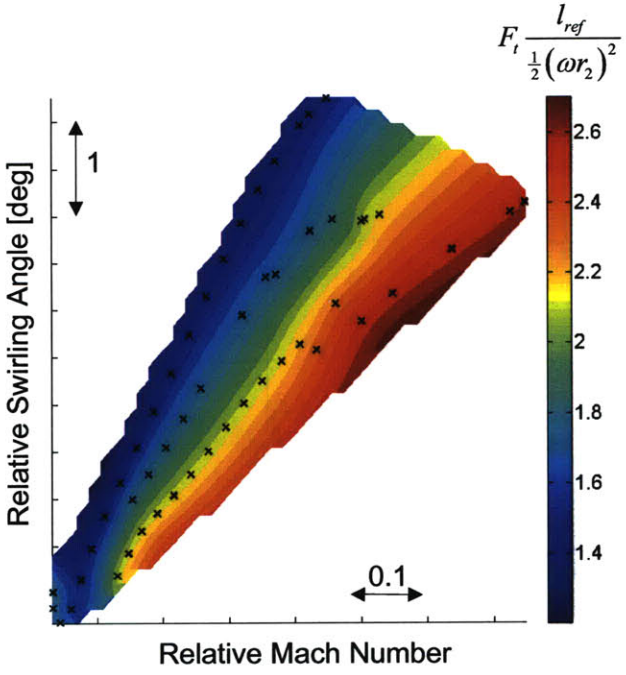


Figure A-1: Tangential body force component at the impeller exit - data from three speedlines provide an independent variation of $M_{rel}$ and $\alpha_{ref}$.

In an unsteady simulation with the body force model, the look-up table provides the body force components as a functions of Mach number and swirl angle. Therefore, an interpolation scheme is required that estimates the value between the available data points. The sparse, unstructured distribution of the data points for a generic cell yields an interpolation and extrapolation challenge. Since the standard interpolation schemes for unstructured data (inverse-distance, triangulation, nearest-neighbor, etc.) fail to provide a reasonable, smooth solution for most of the cells, a statistical estimation scheme, called the spatial Kriging estimation (see [3] for details), was implemented. The Kriging scheme belongs to the family of least-square estimation algorithms. For this application, one major advantage is that Kriging compensates for the effects of data point clustering. Additionally, the interpolation surface is exact on the data points in M-$\alpha$-Force-space and provides a smooth interpolation solution within the data point cloud and its vicinity. For the cell near the impeller exit, the interpolated solution is depicted in Figure A-1.

For the majority of the cells, this method delivers a smooth look-up table with

a sufficient Mach numbers and swirl angle range. However, there is a considerable portion of the cells that have an unfavorable data point distribution in the $M - \alpha$-space.

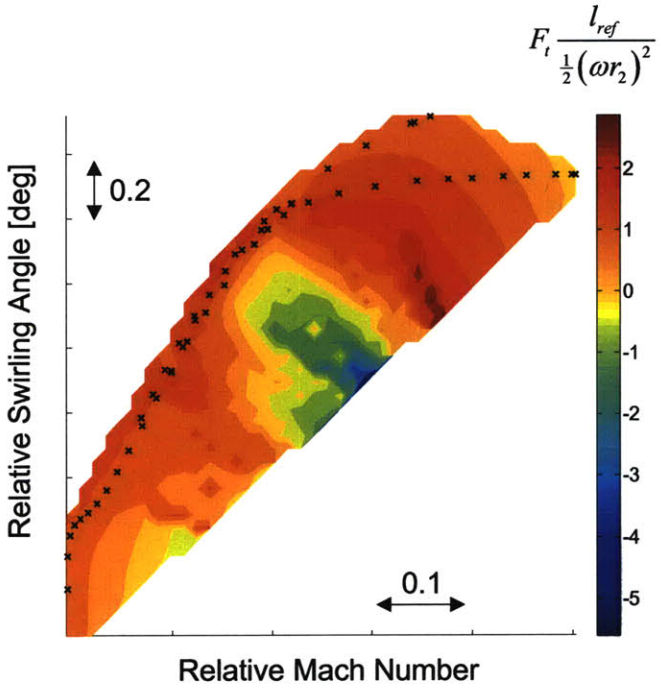


Figure A-2: Tangential body force component at the impeller exit - data from the three speedlines collapse into a single curve making it impossible to estimate the force away from the curve.

The look-up table for a cell in the impeller passage near the splitter blade leading edge is depicted in Figure A-2. The total variation of the flow angle for the data points is less than two degrees. Additionally, the data points from all three speedlines collapse into a single curve. The required estimation of the forces away from the curve of the data points is impossible, since the trend in the direction perpendicular to the curve is unknown. As a result, the body force model is likely to request body forces for flow parameters where a reasonable estimation cannot be performed. It was concluded that the data available from the steady RANS calculations is not sufficient to use the 2D-look-up table approach. A simplified approach based on the meridional Mach number was therefore established (see section 3.4.2).

# Bibliography


[1] W. L. Briggs, V. E. Henson, and S. F. McCormick. *A Multigrid Tutorial.* SIAM, 2000.

[2] T. R. Camp and I. J. Day. A study of spike and modal stall phenomena in a low-speed axial compressor. *ASME Journal of Turbomachinery*, 120:393–401, 1998.

[3] N. Cressie. *Statistics for spatial data.* Wiley, New York, 1993.

[4] I. J. Day. Stall inception in axial flow compressors. *ASME Journal for Turbomachinery*, 115:1–9, 1993.

[5] R.C. Dean. The fluid dynamic design of advanced centrifugal compressors. *Lecture Notes, Von Karman Institute.* Brussels.

[6] A. Demeulenaere. Numeca International, Personal Communications, 2008.

[7] J.D. Denton and U.K. Singh. Time marching methods for turbomachinery flow calculations. *VKI-LEC-SER*, 7, 1979.

[8] H. Emmons, C. Pearson, and H. Grant. Compressor surge and stall propagation. *ASME Journal of Turbomachinery*, 77:455–469, 1955.

[9] A.H. Esptein, J.E. Fowcs-Williams, and E.M. Greitzer. Active suppresion of aerodynamic instabilities in turbomachines. *AiAA Journal of Propulsion and Power*, 5(2):204–211, 1986.

[10] J. Everitt. Master's thesis in progress, Massachusetts Institute of Technology, expected 2009.

[11] Y. Gong. *A Computational Model for Rotating Stall and Inlet Distortions in Multistage Compressors.* PhD thesis, Massachusetts Institute of Technology, February 1999.

[12] Y. Gong, C.S. Tan, K.A. Gordon, and E.M. Greitzer. A computational model for short wavelength stall inception and development in multistage compressors. *ASME Journal for Turbomachinery*, 121:724–736, 1999.

[13] E.M. Greitzer. Stability of pumping systems. *Journal of Fluid Engineering*, 103:193–242, 1981.

[14] E.M. Greitzer, C.S. Tan, and M.B. Graf. *Internal Flow: Concepts and Applications.* Cambridge University Press, Cambridge, England, 2005.

[15] J.M. Haynes and G.J. Hendricks nad A.H. Epstein. Active stabilization of rotating stall in a three-stage axial compressor. *ASME Journal of Turbomachinery*, 116:226–239, 1994.

[16] R. A. Hill. Simulation of spike stall inception in a radial vaned diffuser. Master's thesis, Massachusetts Institute of Technology, September 2007.

[17] R. Hunziker and G. Gyarmathy. The operational stability of a centrifugal compressor and its dependence on the characteristics of the subcomponents. *ASME J. of Turbomachinery*, 116, 1994.

[18] Numeca International. *FINE/Turbo User Manual Version 8.2.* Brussels, Belgium, 2008.

[19] A. Jameson, W. Schmidt, and E. Turkel. Numerical solutions of the euler equations by finite volume methods with runge-kutta time stepping schemes. *AIAA*, (1259), 1981.

[20] G. Kiwada. Development of a body force description for compressor stability assessment. Master's thesis, Massachusetts Institute of Technology, February 2008.

[21] P. Lawless and S. Fleeter. Rotating stall acoustic signature in a low-speed centrifugal compressor, part ii: Vaned diffuser. *ASME Paper*, (GT-254), 1993.

[22] J.P. Longley. A review of nonsteady flow models for compressor stability. *ASME Journal of Turbomachinery*, pages 202–215, April 1994.

[23] F. Marble. Three-dimensional flow in turbomachines. *Aerodynamics of Turbines and Compressors*, X of High Speed Aerodynamics and Jet Propulsion:83–166, 1964. Hawthorne, W.R., editor Princeton University Press.

[24] N.M. McDougall, N.A. Cumpsty, and T.P. Hynes. Stall inception in axial compressors. *ASME Journal of Turbomachinery*, 112:116–125, 1990.

[25] F.K Moore and E.M. Greitzer. A theory of post-stall transients in axial compressors, part i - development of equations. *ASME Journal of Engineering for Gas Turbines and Power*, 108:68–76, 1986.

[26] W. Oakes, P. Lawless, and S. Fleeter. Instability pathology of a high speed centrifugal compressor. *ASME Paper*, 1999. 99-GT-415.

[27] J. Paduano, A.H. Epstein, L. Valavani, J.P. Longley, E.M. Greitzer, and G.R. Guenette. Active control of rotating stall in a low speed axial compressor. *ASME Journal of Turbomachinery*, 115:48–56, 1993.

[28] Z.S. Spakovszky. Backward traveling rotating stall waves in centrifugal compressors. *ASME Journal for Turbomachinery*, 126:1–12, 2004.

[29] Z.S. Spakovszky and C.H. Roduner. Spike and modal stall inception in an advanced turbocharger centrifugal compressor. *ASME Journal of Turbomachinery*, 131, July 2009.

[30] ABB Turbo Systems. Abb turbocharging - product information. www.abb.com/product/us/9AAC132908.aspx, 2008.

[31] K. Toyama, P.W. Runstadler, and R.C. Dean Jr. An experimental study of surge in centrifugal compressors. *ASME Journal of Fluid Engineering*, 99:115–131, 1977.